UTTAC-69, 2001

ANNUAL REPORT

April 1,2000 – March 31, 2001

TANDEM ACCELERATOR CENTER
UNIVERSITY OF TSUKUBA

http://www.tac.tsukuba.ac.jp/

PREFACE

This volume describes research activities in UTTAC during the period from April 2000 to March 2001. The operation of the 12 UD Pelletron tandem accelerator was interrupted in August 2000 because of the trouble of corona points mounted on the first tube section on the low energy end. After the repair of the corona points, the tandem accelerator was continuously operated until the end of February 2001. A total beam time used for experiments was 2783 hours. The tandetron accelerator was used for experiments on solid state physics and PIXE analysis of some biological materials.

The developments of experimental instruments initiated in the last year were continued on a proton polarimeter, a TOF detector for atomic clusters at low velocities, a long focal-plane position-sensitive detector and an ECR ion source equipped with a liquid-helium-free superconducting solenoid.

Nuclear reactions with polarized deuterons, an analysis of the p+^{28}Si total-reaction cross section at energies around the ^{28}Si(p,n) threshold energy, a precise measurement of proton-proton elastic scattering cross section at energies around 20 MeV are included in this volume as progress reports. An experiment on the transient magnetic field using polarized protons was also performed. Nuclear structure physics by means of in-beam gamma ray spectroscopy and some activities in high-energy nuclear physics aiming at the search for quark-gluon plasma are also described in this annual report.

Ion-induced secondary electron spectroscopy, atomic cluster physics, the electronic states of 3*d* transition-metal oxides by NMR and Moessbauer experiments made a steady advance. Some new results are reported on the investigation of an active center produced by the heavy ion bombardment of silica glass and on the diffusion of deuterons implanted in Ta and Cu.

The quantitative trace element analysis of fluid inclusions in natural quartz was carried out by means of PIXE. It turned out that inclusions in the quartz collected from Kwahage quartz veins in Nagano prefecture in Japan contained transition metal elements at several 100-1000 μg / g. A new project of hydrogen analysis was approved in the last year. To construct a new beam line for this project, the heavy-ion post accelerator and the Ge detector array for gamma-ray spectroscopy were shut down. A method of the preparation and calibration of a standard hydrogen-bearing target was developed. The measurements of ^{36}Cl with AMS techniques were performed for samples that were taken at several places near the nuclear fuel processing facility JCO after the critical nuclear accident in two years ago.

A symposium was held on 12 and 13 in December 2000 as the 25th anniversary of the commencement of experiments with 12 UD Pelletron. Many fruitful discussions were made on nuclear physics, solid state physics, PIXE, AMS, and some other topics related to tandem accelerators.

Kohei Furuno

CONTENTS

1. ACCELERATOR AND EXPERIMENTAL FACILITIES

2. NUCLEAR PHYSICS ----- Experiment

3. ATOMIC AND SOLID STATE PHYSICS, AND CLUSTER SCIENCE

1.1 Accelerator operation

K. Sasa, S. Ishii, H. Kimura, H. Oshima, Y. Tajima, T. Takahashi, Y. Yamato,
T. Katabuchi, T. Komatsubara, K. Shima and K. Furuno

The periodic maintenance per year was finished on March 29 in 2000. After the voltage conditioning for two weeks, we provided beams for experiments from April 17. The total operating time and the experimental beam time were 3480.5 and 2782.9 hours respectively, for the period from April in 2000 to March in 2001. Each time recorded an increase of about 20 % as compared with that in the last year. Fig.1 shows the distribution of operation hours every month. The beam time at various terminal voltages is shown in Fig.2. Fig.3 presents the summary of accelerated ions and fractions of their beam time for three ion sources. Fig.4 shows the percentage of experimental beam times for research fields.

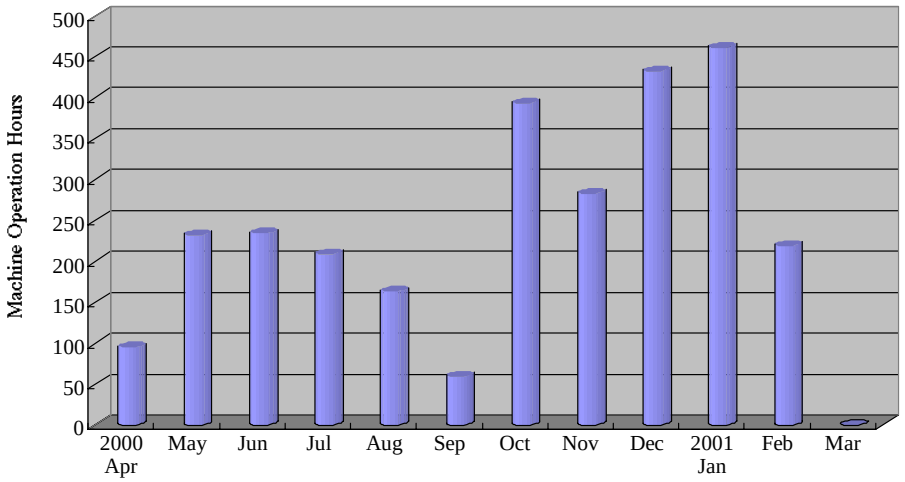

Fig.1 Accelerator operation hours per month from April in 2000 to March in 2001.

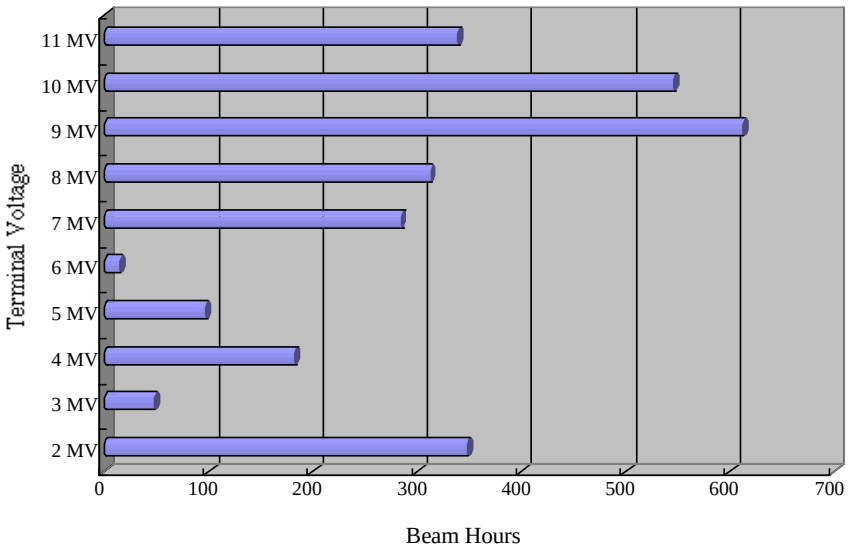

Fig.2 Beam time summed up every 1 MV of terminal voltages.

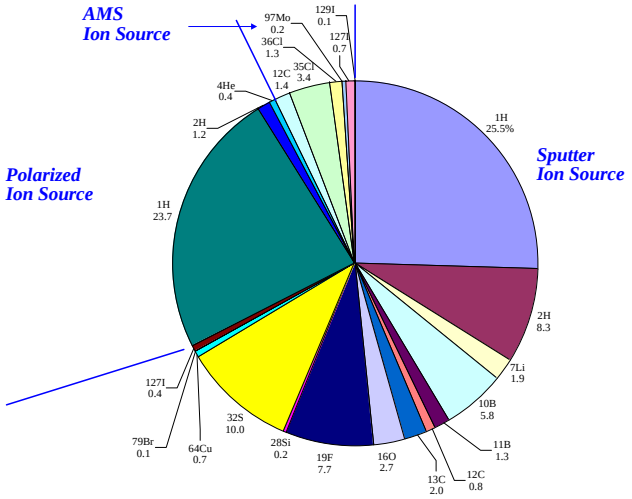

Fig.3 Accelerated ions and fractions of their beam time for three ion sources.

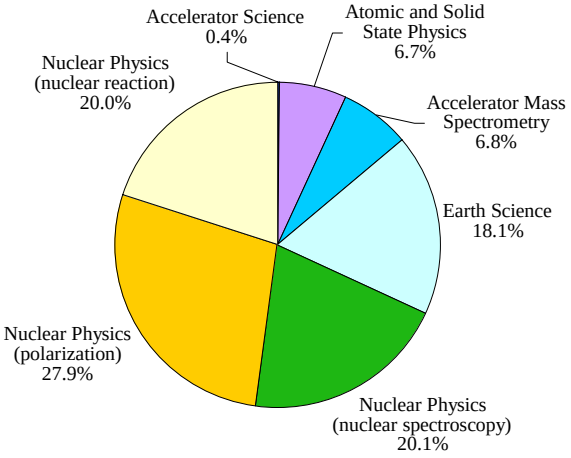

Fig.4 Percentage of experimental beam times for research fields.

The beam time at the terminal voltage of 11 MV was about twice as large as that in the last year. There are two groups in distribution of the beam time. Almost all the high voltages in the range from 7 to 11 MV were used for nuclear physics. Low terminal voltages in the range from 2 to 5 MV were used for the ion beam analysis in earth science.

The operation of the 12UD tandem accelerator was very stable until July in 2000. In August, however, the terminal voltage became gradually unstable. We observed extremely large fluctuation of corona currents and X-ray bursts in the case of the first and second units alive. It suggested that the problem occurred in the first or the second unit on the low energy side. We opened the accelerator tank on August 21. The corona points on the first accelerating tube section hung down as shown in Fig.5 (a). This problem was just the same as that in its position and phenomenon occurred in July of 1999 [1]. The accelerating electrodes were electrically shorted outside the tube two by two in order to reduce the voltage gradient at the entrance of the accelerating tube for small magnification as a converging lens. For this

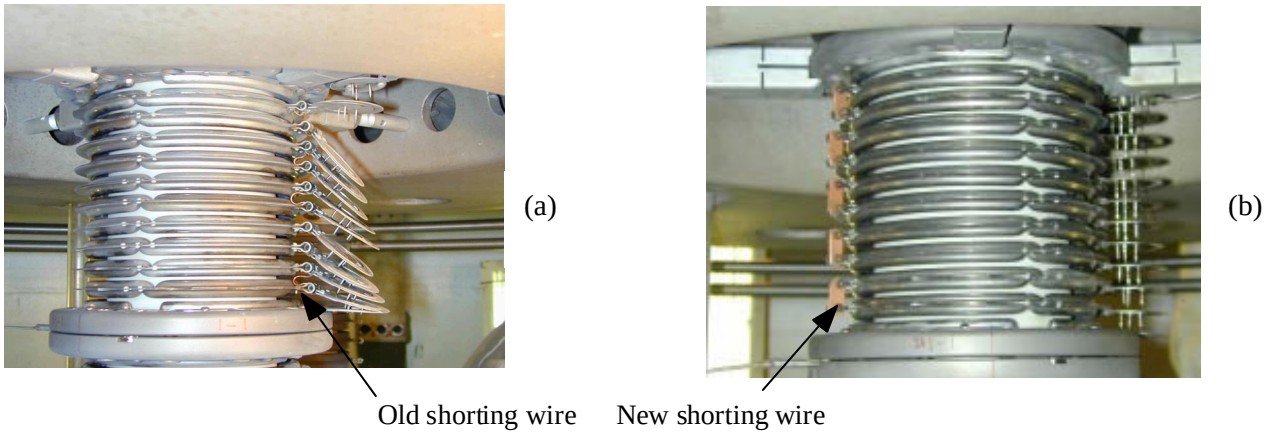

Fig.5 Shorting wires on the first accelerating tube. (a): Hanging corona points before the repair. Shorting wires directly were connected to corona needle plates. (b): Shorting wires were modified to copper plates and mounted on the opposite side of the corona points in the position.

Fig.6 A plumb was hung down from the upper chain sheave to the bottom of the tank. The position of the lower sheave was adjusted with respect to the position of the plumb.

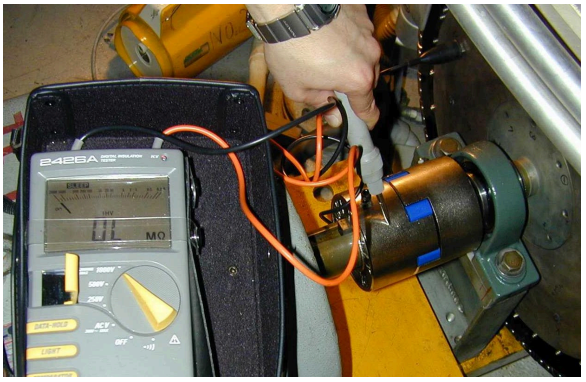

Fig.7 A photograph of the chain-motor coupling. It is made of Hytrel developed by DU PONT-TORAY Co., Ltd. We selected it in order to insulate between the motor and the sheave.

purpose, a copper wire was put between the socket for the corona points on the spark-gap ring of the electrode. In addition to the difficulty for obtaining stable fit in this geometry, the thread became worn so that the connecting force was not strong enough. We separated the mount of shorting wires from that of corona points. Copper plates instead of wires were used to short electrodes with new setscrews. The copper plates have a stable fit on the socket and the screw holder. Fig.5 (b) shows the new shorting method for the first accelerating tube section.

As regards other troubles, the power supply for switching magnet in the second target room was broken on August 1. We used the power supply of the first target room temporarily until March of 2001, and then a new power supply produced by DANFYSIK Co., Ltd. was installed.

There is a serious problem in our SF_6 gas system. The compressor is very old and an appreciable leak

occurs at the connecting rod. We lost SF_6 gas by 656 kg in the operation of the gas handling system twelve times year of 2000. Four times of them were carried out for the maintenance. The others were performed for AMS experiments. In our experience, stable corona currents along the accelerating tube in particular are necessary to obtain reasonable reproduction of the data.

The scheduled maintenance in the spring of 2001 was started from the March 1. The major works of this maintenance were as follows. All corona points were replaced along the column and the accelerating tube. Stripper foils in A and B foil changers were also replaced by new foils. Before the start of this scheduled maintenance, there was a tendency to increase the fluctuation of the charging current when the acceleration of beams was unstable in the slit control mode. It was supposed that the fluttering of the chain sheave during the rotation and the snaking of the chain towards the terminal might cause the fluctuation of the charging current. We carefully adjusted the position and alignment of sheaves by hanging down a plumb from the sheave in the terminal (Fig.6). The old ball bearings of the sheaves were replaced. The insulating coupler made of Hytrel, which was supplied by DU PONT-TORAY Co., Ltd. was inserted between the chain motor and the sheave (Fig.7). The resistance between the sheave and the ground was increased to a value larger than 2000 MΩ. An overhaul was made of the thin plate attached to the sheave (contact band) to obtain good contact with pellets. Finally, we adjusted gaps between the chain and stabilizing wheels (idler wheels) in such a way that the snaking of the chain became as small as possible. After these works, the fluctuation of the charging current disappeared as long as we observed the current on the analog current meter by the eyes.

In the period of this maintenance, some modifications on beam lines were carried out. This was motivated by the start of a new project of micro-beam hydrogen analysis with ^{19}F and ^{15}N ions in one hand. Another motivation was that the walk of the focus in the first target room produced by the quadrupole doublet in front of the switching magnet was large. It was because of the misalignment of the beam emerging from the image slit of the beam analyzer from the axis of the quadrupole doublet. To carry out the new project, the heavy-ion post accelerator was shut down. The post buncher installed about 1 m upstream of the quadrupole doublet was removed. This part of the beam line was modified to a simple beam line equipped with an ion pump. The work of the focus produced by the quadrupole doublet was minimized by the displacement of the opening in the object slit of the beam-analyzing magnet by 1 mm from the vertical line of the accelerator. The opening position was adjusted by observing the movement of focus on a ZnS plate as the excitation current of the magnet was increased. This displacement would be due to the fact that the bending plane of the beam-analyzing magnet is not vertical exactly.

The total operating time of the tandetron accelerator was 524 hours for the period of last year. We have used this accelerator for PIXE, RBS, secondary electron spectroscopy, detector tests and preliminary experiments for investigations using the 12UD tandem accelerator. At present, we have been constructing a new micro-beam line for PIXE and/or RBS analyses.

[References]

[1] K. Sasa et al. UTTAC-68 (1999) 1.

1.2 Construction of a system for hydrogen analysis

K. Sasa, K. Furuno, H. Oshima, Y. Yamato, T. Takahashi and K. Shima

The hydrogen analysis of minerals and rocks by means of the resonant nuclear reaction $^{1}H(^{19}F, \alpha\gamma)^{16}O$ or $^{1}H(^{15}N, \alpha\gamma)^{12}C$ was started as a new project in 2000. One of the objectives is the measurement of the concentration of water in fluid inclusions in minerals. Since the size of the fluid inclusions in the range from 100 to 30 μm or less, the incident ^{19}F or ^{15}N beam must be focused on mineral samples in an area as large as those of fluid inclusions. In addition to the transverse confinement of the area of beam irradiation, the measurement of depth profile is necessary for three-dimensional mapping of water in fluid inclusions. We have developed a new beam line dedicated to the hydrogen analysis in the 0° beam course in the first target room. This report describes the design and a preliminary test experiment to estimate beam currents through a narrow slit.

[1] Design of the beam line.

Fig.1 shows a schematic layout of the new beam line. It consists of a beam defining aperture (first slit), a collimating aperture (second slit), a diaphragm (third slit) and a quadrupole lens. The length of the beam line is limited within 14.7 m by walls of the target room. Taking a passage and working space behind the target chamber, we determined the distance from the beam exit wall to the target to be 11 m. The first slit is placed at a position of 0.3 m upstream from the wall of the switching magnet room. The resultant distance between the 1st slit and the target is 12.8 m. The distance from the exit of the quadrupole lens to the target is chosen to be 0.35 m from a tentative design of the target chamber. Other distances are presented in Fig.1.

The beam emerging from the image slit of the beam analyzing magnet is once focused onto the first slit through 0° port of the switching magnet with the aid of the quadrupole doublet (QS) and a steering magnet

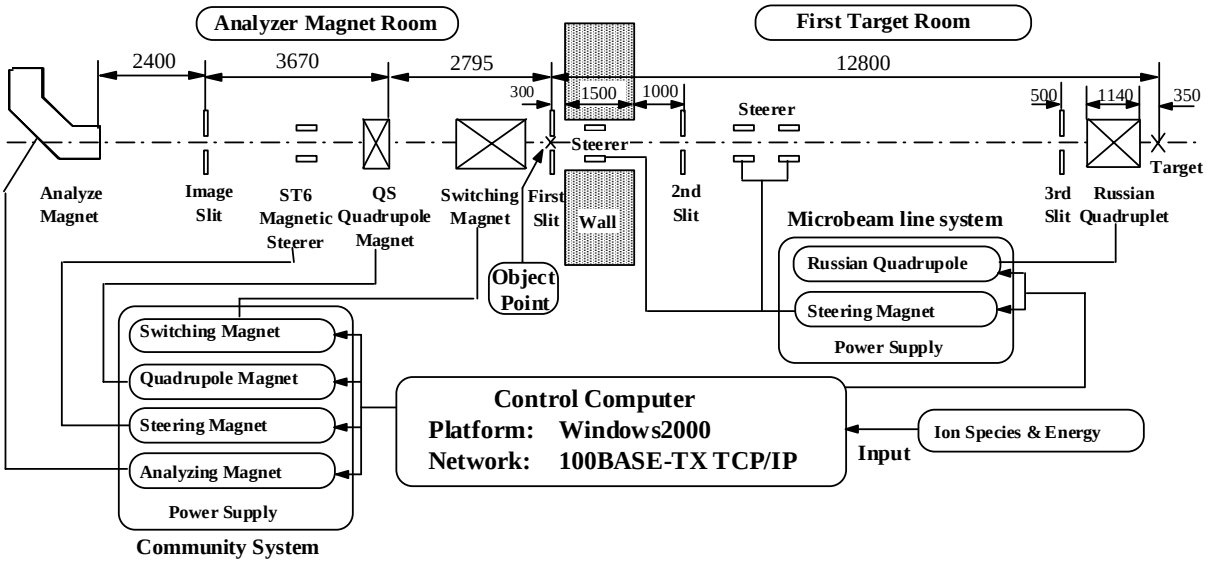

Fig.1 A schematic layout of the beam line and the control system.

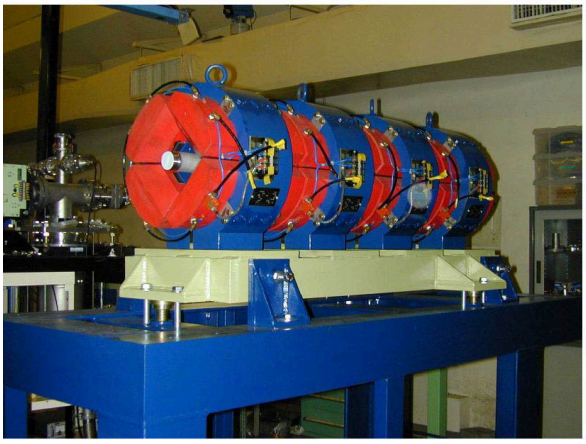

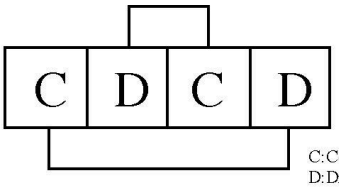

Magnetic pole length	**150 mm**
Magnetic pole effective length	**166 mm**
Space between the poles	**180 mm**
Bore radius	**25 mm**
Maximum field gradient	**2.2 kG/cm (20A)**
Setting error of the pole	**< 50μm**

Fig.2 A photograph of the Russian quadruplet and the specifications.

(ST6). The beam is further collimated by the second slit placed 2.8 m apart from the first slit. An adjustable diaphragm is prepared to limit the divergence of the beam. The beam is finally focused on the target by means of a Russian Quadruplet[1]. This quadrupole lens was constructed by remodeling two quadrupole doublets available in our laboratory. The space between two poles was 200 mm in the old doublets, but it turned out from a calculation that a narrower space was advantageous to obtain smaller beam spot sizes on the target. On the basis of this calculation, the space was modified to be 180 mm, which was narrowest space limited by the mechanical structure of the old quadrupole magnet. The principal specifications are described in Fig. 2.

Beam optics calculations were carried out with the computer program TRACE-3D [2]. A typical example of the envelope of $^{19}F^{4+}$ ions at an energy of 30 MeV is displayed in Fig.3. The calculation is made the assumptions that the diameter of the first slit is 0.71 mm; the maximum angles of the beam are 0.71 mrad in both vertical and horizontal planes; the energy spread of the beam is 12.5 keV. On these conditions, the diameter of the beam spot on target is 59.2 μm, while the angles are 8.45 mrad in both planes. This result implies that a reduction factor of 0.084 could be expected for the beam diameter. The maximum transverse excursion of the beam occurs in the vertical plane. The value is about 11 mm. It is sufficiently smaller than the inner radius of 17.5 mm in the vacuum pipe of the Russian quadruplet.

The depth profile of hydrogen atoms can be obtained from the measurement of the yield of γ rays as a function of the incident beam energy. The principal composition in most of the minerals and rocks is SiO_2. The width of the 16.44 MeV resonance is reported to be 83.8 keV in the laboratory frame [3]. The

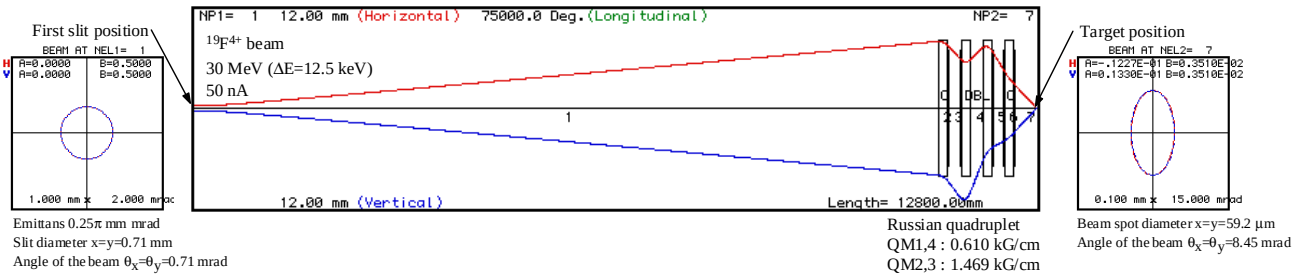

Fig.3 A calculated beam envelope in horizontal and vertical planes of the proposed $^{19}F^{4+}$ ions at 30 MeV. Emittance diagrams at the first slit and the target are also displayed.

thickness corresponding to the width of 83.8 keV is calculated to be 0.03 μm with the stopping power of ^{19}F ions in SiO_2. This value is much smaller than a typical size of fluid inclusions. Although it depends on research subjects how many data points are required for depth profiling of a certain fluid inclusion, the incident energy should be changed, in general, over several tens of steps. The design and construction of an automatic focusing system, therefore, are in progress. The concept is presented in Fig.1. Power supplies for the beam analyzing magnet, quadrupole magnets and steering magnets are controlled by a personal computer equipped with Windows 2000 as its operating system.

[2] Test experiments.

As described in the preceding section, the diameter of the first slit must be smaller than 0.6 mm to obtain beam spot sizes on target smaller than 50 μm. It is obvious that the beam current seriously decreases after the first slit. We performed a test of beam transmission for $^{19}F^{4+}$ and $^{19}F^{5+}$ beams to estimate practically obtainable beam currents. Experimental setup is shown in Fig.4. The Faraday cups FC1 and FC2 are mounted on the object and image position of the injection magnet. FC2 measures negative beam currents injected into the tandem accelerator. FC3 is located at the exit of the accelerator, while FC4 is placed in front of the beam analyzing magnet. FC5 is installed just after the image slit of the beam analyzing magnet, and measures the analyzed beam current.

A tentative slit was placed at a distance further than the design position of the first slit by 4.8 m. Three apertures of 0.6, 1 and 2 mm in diameter were prepared for the tentative slit. The surfaces of these apertures were covered with ZnS phosphor to observe the beam spot with video camera. Beam currents after the tentative slit were measured with the same type Faraday cup as FC5. The energies of beams were 20 MeV for $^{19}F^{4+}$ ions, and 24 MeV for $^{19}F^{5+}$ ions, respectively. The experimental results are summarized in Table 1.

The beam currents observed with the aperture of 0.6 mm in diameter were 2.5 enA for 20 MeV $^{19}F^{4+}$ ions, and 6.3 enA for 24 MeV $^{19}F^{5+}$ ions. The beam spot was 4 mm wide and 8 mm high. This size of the beam

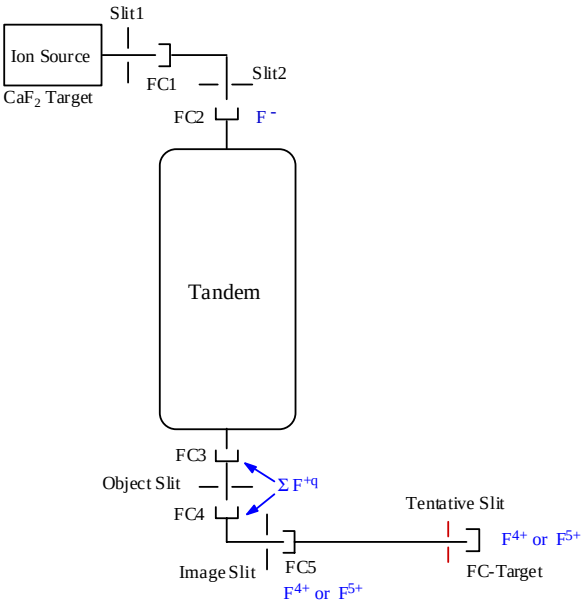

Fig.4 A schematic diagram for the measurement of transmission of ^{19}F beams.

spot is roughly in agreement with the opening of the image slit of the beam analyzing magnet (2 mm times 3 mm) multiplied by the magnification of the quadrupole doublet (QS) in front of the switching magnet. If we move the first slit to the design position, the magnification of QS became almost unity. The ratio of areas of the aperture of 0.4 mm in diameter to the beam spot of 2 mm times 3 mm is approximately 0.02. Thus an expected beam current through the aperture of 0.4 mm in diameter is calculated to be 2 enA for an analyzed current of 100 nA at FC5, if we make a very crude assumption that the beam intensity has uniform distribution over the area of 2 mm times 3 mm.

The experimental results given in Table 1 indicates that about 1 μA of negative beam currents are necessary to obtain 100 enA of analyzed beam current at FC5. The operation of the tandem accelerator was stable without problems like electron loading for injection of negative beam of 1 μA or more. Short lifetimes of stripper foils remains as a practical problem in such an acceleration of low-energy heavy-ion beams with high intensity as the present application.

Table 1. Experimental results of the beam transmission for 20 MeV $^{19}F^{4+}$ and 24 MeV $^{19}F^{5+}$ ions.

	FC1	FC2	FC3	FC4	FC5	FC-target φ2	FC-target φ1	FC-target φ0.6
$^{19}F^{4+}$ (nA)	2700	1300	1950	350	115	16	5	2.5
$^{19}F^{5+}$ (nA)	2500	1150	1950	450	225	-	11	6.3

Acknowledgement

This work is supported in part by the Grand-in-Aid for Scientific Research (A) of the Ministry of Education, Science, Sports and Culture.

References

[1] A. D. Dymnikov, T. Ya. Fishkova and S. Ya Yavor, Sov. Phys. Tech. Phys. 10 (1965) 340.

[2] K. Crandall and D. Rusthoi, “TRACE-3D Documentation”, third edition, Los Alamos National Laboratory Report LA-UR-97-886(1997).

[3] F. Ajzenberg-Selove, Nucl. Phys. A475(1987)163.

1.3 Development of a proton polarimeter using a liquid helium target and a measurement of the polarizations of the ^{52}Cr($d,\vec{p}$)^{53}Cr reaction

K.Sawada, M.Yamaguchi, T.Katabuchi, Y.Tagishi

We have developed a proton polarimeter using a liquid helium target for double scattering experiments [1]. Fig. 1 shows the vertical section of the polarimeter. The polarimeter target was liquid helium held in a conical cell. It was connected to a helium tank. The helium tank was supported by the stainless steel pipes and fixed to an upper flange of the polarimeter. The helium tank was surrounded by a liquid nitrogen tank.

The polarimeter was improved by keeping tightly the thermal insulation. First, to cut heat radiation, the liquid helium tank was covered with the copper foil. Thickness of the foil was 0.5 mm. The foil was connected to the liquid nitrogen tank by using cryogenic high vacuum grease for the purpose of thermal conduction.

Secondly, the top of the each pipe of the helium tank was connected to the liquid nitrogen tank with a bundle of copper wires. By the bundles of wires, the tops of the pipes were refrigerated and heat flow from the upper flange to the the helium tank was reduced. The length of each bundle was about 25 cm. The combined cross section of the bundle wires was about 0.45 cm^2.

The evaporation rate of the liquid helium was measured and thermal inflow was estimated. It was about 240 mW. The value was consistent with the value calculated from thermodynamics.

By using this proton polarimeter, we measured polarization of the reactions ^{52}Cr($d,\vec{p}$)^{53}Cr to $\frac{3}{2}^-$ state at g.s. and $\frac{1}{2}^-$ state at 564 keV at three laboratory angles $15^\circ, 20^\circ, 30^\circ$. The polarimeter was set at the focal position of QDQ spectrometer[2]. The ^{52}Cr target was self supporting foil with a thickness of approximately 0.5 mg/cm^2. We used effective analyzing powers of the polarimeter that had been measured before [1]. Figure 2 show the measured polarizations.

References

[1] M. Yamaguchi et al., UTTAC Annual Report, **66**, 7(1998).

[2] Y. Aoki et al., UTTAC Annual Report, **52**, 19(1987).

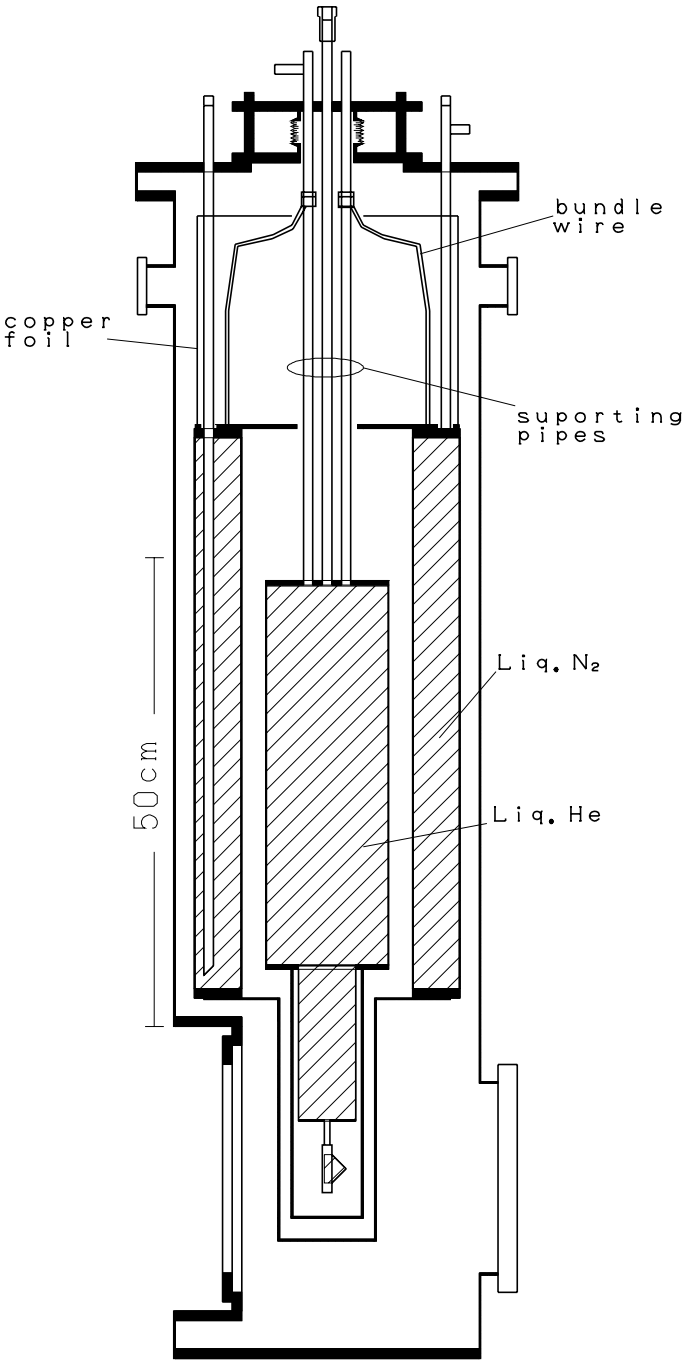

Fig. 1. The vertical section of the polarimeter.

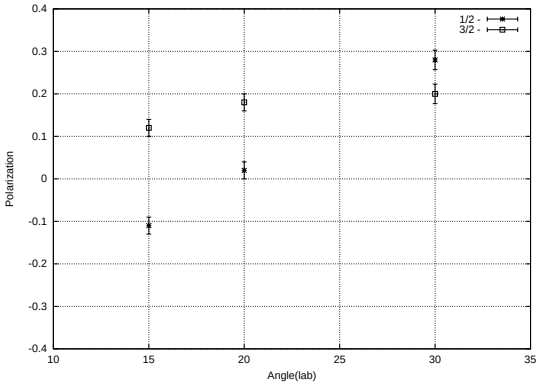

Fig. 2. Polarizations for The ^{52}Cr$(d,p)^{53}$Cr reaction to $\frac{3}{2}^-$ state at g.s. and $\frac{1}{2}^-$ state at 564 keV.

1.4 Development of oven type cluster ion source

T.Miyazaki, I.Arai and S.M.Lee

Recently research of nanostructures of using clusters has become one of the leading topics in the fields of both fundamental physics and applications. Especially, the behavior of size-selected clusters deposited on the substrate takes more attention. [1] For such research, we need an intense cluster ion source which can provide a beam of size-selected cluster ions with proper intensity.

A cluster ion source is decomposed into three parts from its functional view point as follows.
(1) a region for making vapor of material
(2) a region for growing clusters by cooling the vapor of material with noble gas
(3) a region for ionizing clusters

The intensity of cluster beam mainly depends on the operating conditions in the regions (1) and (3). The evaporation rate from the surface of material and the ionization efficiency are the parameters to determine the maximum available intensity of cluster beam. The distribution of cluster size mainly depends on the operating conditions in the region (2). The vapor of material is cooled down by multiple collisions with noble gas atoms while the large-sized clusters grow through the aggregation of vapor atoms. The pressure and temperature of the noble gas and the length of the tube, i.e., the aggregation length, are the parameters to control the distribution of cluster size.

The main difference among the ion sources so far developed is found in their methods of vaporization, e.g., the laser ablation, the sputtering with high energy particles and the thermal heating. An oven type cluster ion source uses a method of Joule heating to vaporize material. Although this methods is applicable only for materials with low melting point and high vapor pressure such as Na, K and Pb, it's quite simple and convenient to achieve a considerable increase of the amount of vapor with the least expense.[2] Under these conditions, we've developed of a homemade oven type cluster ion source for the research of nanostructures.

Fig.1 and Fig.2 show a schematic drawing and pictures of our cluster ion source, respectively. The metal vapor coming from the first nozzle joined to the crucible is cooled down by the helium gas in the aggregation tube contacted with liquid nitrogen . The first nozzle controls the flow of metal vapor and suppresses the dispersion of flow, i.e., a main cause of the beam intensity loss. In the aggregation tube, the metal vapor atoms condense to form clusters. The

mixture of helium atoms and metal clusters is guided via the second nozzle into the ionization region maintained at a pressure of 10^{-4}torr by using a diffusion pump (Varian VHS-6) with a pumping speed 3000 l/s for helium. A certain part of the clusters are ionized by an electron impact method applied in the ionization region and accelerated horizontally toward the beam transport joined to the TOF mass analyzer. The advantage of the developed system is that neutral particles flow out vertically and only charged particles are extracted horizontally by the electrical field. With this configuration, we can completely get rid of the contamination of useless particles. To achieve a good connection and sealing between the first nozzle and the crucible, we designed the crucible as follows. An aluminum crucible (8mm×100mm) is screwed and attached to the first nozzle (2mm×6mm). The joined structure is put into an aluminum oxide crucible wound with a MnNi ribbon heater ~(2×6mm^2×1300mm,≈6Ω). For example the ejection rate of sodium from the first nozzle is evaluated as 6.2×10^{-8} [mole/sec] when the crucible's temperature T_s is 620K,which means a saturated vapor pressure 0.1torr for sodium. We can keep this flux for several weeks in the case when the half volume of the aluminum crucible is filled with around 5cc of sodium.

The crucible is mounted on a movable supporting rod to adjust the distance L between the first nozzle and the second one over the range from 0 to 20 cm. L affects the size distribution of metal clusters. We can control the pressure of helium gas in the aggregation tube by adjusting its flow or by changing the conductance of the second nozzle. When we set 50scc/m in as a helium gas flow and use the second nozzle of the size 3mm×10mm, the pressures of inside and outside of the aggregation tube are 0.75torr and 0.75×10^{-4} torr, respectively. This condition is similar to the ones used in other cluster ion sources.[3][4] Under this pressure condition, the heat conduction from the crucible to the aggregation tube is mainly due to the helium viscous flow, which is independent of the pressure of helium gas but inversely proportional to the distance X between the crucible and the wall of aggregation tube. The heat loss from the crucible is calculated as 24W when T_s=620K, P_s=1 torr and X=15mm. It is not large compare to the latent heat of vaporization of liquid nitrogen. We can cool down the helium gas below 100K with any effort.

To ionize neutral particles, we use a heat cathode plasma method.[5] W wire(0.20mm) is heated up around 2300 K by Joule heating and eventually ejects thermal electrons. The wire is biased to –100V against the second nozzle kept at the ground voltage. As a result, the thermal electrons are accelerated to have energies to ionize neutral particles. It is reported that an ionization efficiency of 20% has been achieved by combining the accelerated thermal electrons with permanent magnets.[4] We got 10^{-4} as an ionization efficiency without permanent magnets. This value is a typical one for a weakly ionized plasma.

In present, we have achieved a beam intensity of 100nA for sodium. The beam contains all the

sizes of clusters. We've not known the mass distribution clusters. The next step is to combine a TOF mass analyzer with our cluster ion source and examine adequate operating conditions for the production of size-selected cluster ions.

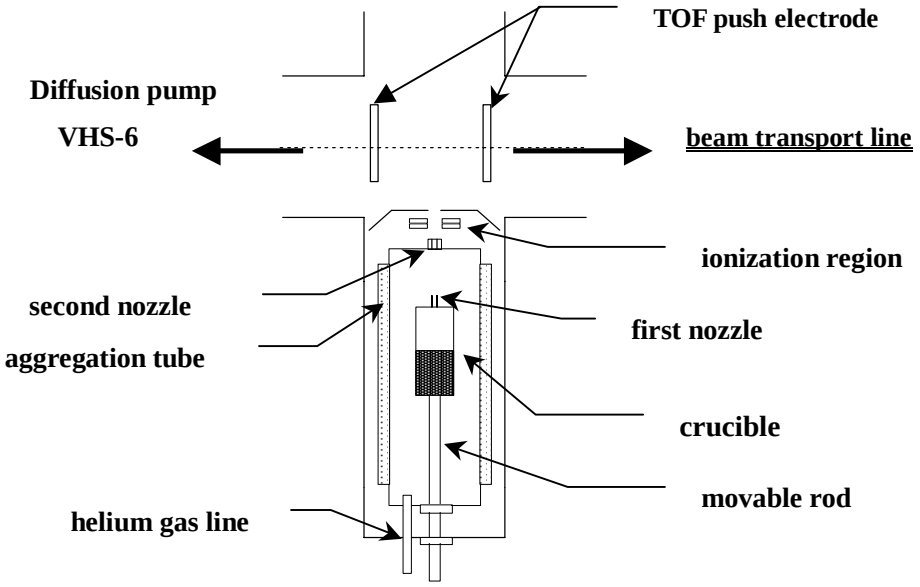

Fig. 1 Schematic drawing of cluster ion source.

(a) Crucible

(b) Aggregation tube

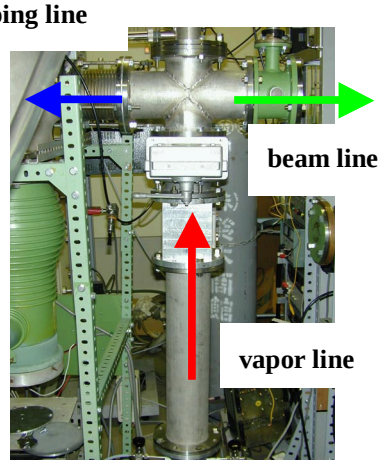

(c) Whole setup

fig.2. Pictures of cluster ion source.

References.

[1] P.Jensen, Rev. Mod. Phys., 71(1999)1695.

[2]Clusters of Atoms and Molecules I and II, edited byH.Haberland, (Springer,Berlin,1994).

[3] U.Zimmermann, et.al. , Z.Phys. D31, (1994)85.

[4] I.M.Goldby, et.al., Rev.Sci.Instrum. 68(1997)3327.

[5] L. Valyi, “Atom and ion sources” (John Wiley &Sons, London,1977).

2.1 Polarization transfer in the ^{2}H(d,p)^{3}H reaction at $\theta = 0^\circ$ at very low energies

Tatsuya Katabuchi, Kohei Kudo, Kazuyuki Masuno, Tomoyuki Iizuka, Yasuo Aoki, and Yoshihiro Tagishi

The fusion reactions ^{2}H(d,p)^{3}H and ^{2}H(d,n)^{3}He in the sub-Coulomb energy region have been studied with great interest because of a suggestion that the reactions initiated by two parallel-polarized deuterons would be suppressed, thus leading to "neutron-lean" fusion reactors [1]. This suggestion has aroused controversy because no direct spin-correlation measurement has been performed due to the difficulty in developing a polarized deuteron target and theoretical predictions from several models conflict. For more understanding of the mechanisms of this reactions, we have measured the polarization transfer coefficient $K_y^{y'}$ for the ^{2}H(d,p)^{3}H reaction at a scattering angle of 0° at very low energies ($\leq$ 90 keV). The preliminary results have been previously reported[2, 3]. In this report, we describe the latest experimental results and comparison with a theoretical prediction.

The experimental detail was described in the previous reports[2, 3]. Thus we here explain the experimental condition briefly. The experiments were performed with a 90-keV polarized deuteron beam from a Lamb-shift polarized ion source at UTTAC. We used a proton polarimeter using p - ^{28}Si elastic scattering to measure the polarization of protons from the ^{2}H(d,p)^{3}H reaction. A silicon solid-state detector was used as the analyzing ^{28}Si-target of the proton polarimeter, so that the background events could be reduced by requiring coincidence between the analyzing detector and the scattered-proton detector of the polarimeter. Deuterated-polyethylene $(CD_2)_n$ with a thickness of 10 μm deposited on a 15-μm thick Al foil was used as a deuteron target. The incident deuteron beam was stopped by the $(CD_2)_n$ target. An incident deuteron, losing its energy in the target, can react with a target deuteron at lower energies than the incident energy of 90 keV. The mean value of the reaction energy estimated from the reaction cross sections [5] and the stopping powers of $(CD_2)_n$ for deuterons is 68 keV [6]. The polarization transfer coefficient $K_y^{y'}$ was obtained by measuring separately the double-scattering yields of the incident deuterons in the $m_I = +1$ and $m_I = -1$ magnetic substates from the polarized ion source for the spin-quantization axis oriented at an angle of 54.7° from the beam direction. The spin-quantization axis was controlled by the Wien-filter system of the polarized ion source. As a result, the polarization transfer coefficient $K_y^{y'}$ was determined to be 0.09 ± 0.10. The error includes statistical errors for the proton polarization measurement ($\pm$0.08) and uncertainties associated with the ion source and the proton polarimeter ($\pm$0.04).

We compared our experimental estimate of $K_y^{y'}$ with a value calculated using the transition amplitudes determined by Lemaître and Schieck in Ref.[4] for the ^{2}H(d,p)^{3}H reaction. In the analysis, using a simple barrier penetrability model, they determined all low-energy transition amplitudes for the ^{2}H(d,p)^{3}H and ^{2}H(d,n)^{3}He reactions from a fit to the Legendre expansion coefficients of the experimental data for the cross section, analyzing powers and proton polarization induced by unpolarized deuterons for $E_d < 500$keV. The calculated results for incident energies of 10 and 90 keV and the experimental estimate are shown in Fig. 1. The measured value is a mean of $K_y^{y'}$ over deuteron reaction energies lower than an incident energy of 90 keV. The corresponding theoretical mean, evaluated from an energy-integration over the calculated $K_y^{y'}$ weighted with the reaction cross section, is 0.25 (shown in Fig. 1 as a triangle). The experimental result differs from the calculation from the transition amplitudes by 1.5 standard deviations. For further discussion about the suppression of the d + d reactions, the values of $K_y^{y'}$ calculated from other models for the d + d reactions should be compared with the present experimental value.

References

[1] R. M. Kulsrud, H. P. Furth and E. J. Valeo, Phys. Rev. Lett. **49**, 1248 (1982)

[2] T. Katabuchi, K. Kudo, K. Masuno, T. Iizuka, Y. Aoki and Y. Tagishi, in Proceedings of the 14th International Spin Physics Symposium (SPIN2000), Osaka, October 2000

[3] K. Kudo, T. Katabuchi, K. Masuno, T. Iizuka, Y. Aoki and Y. Tagishi, UTTAC Annual Report 1999, 28 (2000)

[4] S. Lemaître and H. Paetz. gen. Schieck, Ann. Phys. **2**, 503 (1993)

[5] R.E.Brown and N.Jarmie, Phys. Rev. **C41**, 1391 (1990)

[6] J. Biersack and J. F. Ziegler, TRIM89, version-5.1 (1989)

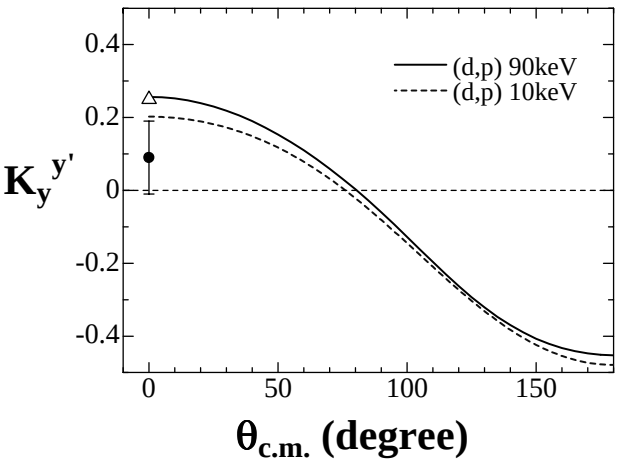

Fig. 1. The measured polarization transfer coefficient $K_y^{y'}$ (solid circle), the values calculated from the transition amplitudes determined by Lemaître and Schieck in Ref. 4 (solid and dashed curves), and the mean value of the calculated value over the incident energies (triangle).

2.2 Analyzing powers for the $(\vec{d}, \alpha)$ and $(\vec{p}, \alpha)$ reactions in the continuum at an incident energy of 20 MeV

K.Masuno, T.Katabuchi, M.Yamaguchi, N.Kawachi, K.Kudo, K.Sawada, T.Iizuka and Y.Tagishi

Continuum energy spectra of emitted particles from nuclear reactions have been studied to obtain information on relaxation process from a simple state well-described by the shell model to an complicated equilibrium state of nuclei. Kozlowski et al. have derived the ratio of energy relaxation time to spin relaxation time of nuclei from the analyzing powers of (p, α) reactions in continuum using a spin relaxation model[1]. In the present work, we have measured analyzing powers of (p, α) and (d, α) reactions on several targets at an incident energy of 20 MeV and evaluated the ratio of the energy to the spin relaxation times for the reaction ^{100}Mo(d, α) based on the Kozlowski model.

For particle identification over a wide dynamic range for α particles, we used a ΔE-E counter system consisting of a proportional gas counter as a ΔE-counter and four silicon solid state detectors (HAMAMATSU S3204-06) as E-counters. The proportional gas counter had a large window with an area of 200 $\times$ 20 mm^2. The silicon detectors had an area of 18 $\times$ 18 mm^2, were placed behind the gas counter and separated from each other in 10° steps. The anodes of the silicon detectors were connected in series through resistances. We could clearly distinguish signals of the counters from each other by the charge division method with a position detector analyzer (ORTEC464). The energy signals of the detectors were obtained from the cathodes. We reduced background events by requiring a coincidence between the gas counter and one of the silicon detectors.

Experiments were performed at UTTAC using polarized protons and polarized deuterons at an incident energy of 20 MeV. Polarized protons and deuterons from a Lamb-shift polarized ion source were accelerated with a Pelletron 12UD tandem accelerator. The accelerated polarized protons or deuterons bombarded a target in a scattering chamber with a diameter of 90 cm. Self-supporting enriched targets of ^{58}Ni, ^{92}Zr, ^{94}Mo, ^{100}Mo, ^{208}Pb and ^{197}Au were used. Continuum spectra from a mylar foil and a natural carbon foil bombarded with 20-MeV protons and deuterons were also obtained to eliminate undesired contribution of carbon and oxygen contamination to continuum spectra of (p, α) and (d, α) for the enriched targets. The beam polarization was obtained by a quench ratio method.

We measured the angular distributions of the analyzing power A_y for the (p, α) reactions from the ^{58}Ni, ^{92}Zr, ^{94}Mo, ^{100}Mo, ^{197}Au and ^{208}Pb targets and the analyzing power iT_{11} for the (d, α) reaction from the ^{100}Mo target. The obtained results for ^{100}Mo(p, α) and ^{100}Mo(d, α) at laboratory angles from 80° to 120° are shown as functions of outgoing α-particle energy in Figs. 1 and 2. The analyzing power iT_{11} for the reaction ^{100}Mo(d, α) is found to increase as α-particle energy increases in contrast to A_y for the ^{100}Mo(p, α). This behavior of iT_{11} for the reaction ^{100}Mo(d, α) agrees with an expectation from the Kozlowski model that a projectile loses gradually its energy and polarization in the target nucleus by successive two-body interactions and, as a result, the vector analyzing power decreases as outgoing particle energy decreases. Thus, we estimated the ratio of energy relaxation time to spin relaxation time from the experimental data for ^{100}Mo(d, α) based on the Kozlowski model. We modified the Kozlowski model for deuteron induced reactions. In the modified Kozlowski model, the vector analyzing power iT_{11} is expressed as follows:

$$iT_{11}(E^*) = iT_{11}(0)[1 - \frac{E^*}{E_M}]^{\beta} \quad (1)$$

where E^* is the excitation energy of the residual nuclei, E_M is the maximum energy of the emitted α-particles ($E_M = E_d + Q$ in c.m.) and β is the ratio of the energy to the spin relaxation times

($\beta = \tau_e/\tau_s$). The value of E_M is 27.7 MeV in ^{100}Mo(d,α) reaction at an incident energy of 20MeV. From a least-squares fitting to Eq. 1, we obtained the values of $\beta = 5.11 \pm 0.55$ and $iT_{11}(0) = 0.30 \pm 0.04$. The fitting result is shown in Fig. 3 as a function of excitation energy of the residual nucleus, E^*.

References

[1] M.Kozlowski et al., Nucl. Phys. A449,251 (1986)

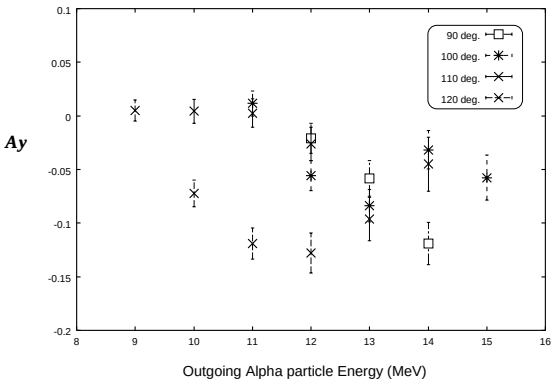

Fig. 1. Experimental data of A_y for the $^{100}Mo(\vec{p},\alpha X)$ reaction

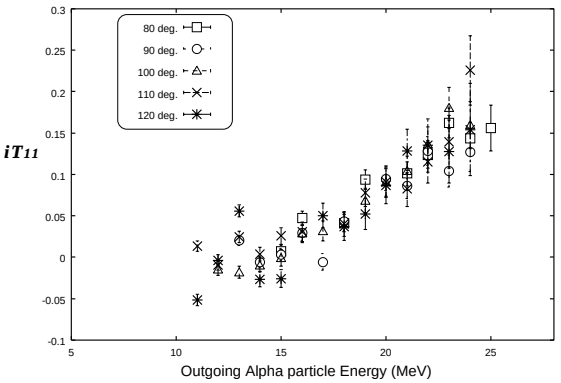

Fig. 2. Experimental data of iT_{11} for the $^{100}Mo(\vec{d},\alpha X)$ reaction

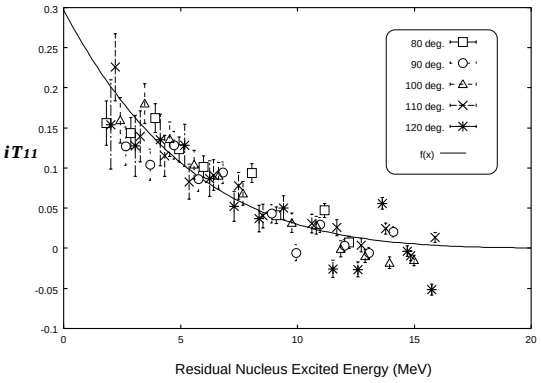

Fig. 3. Experimental data of iT_{11} for the $^{100}Mo(\vec{d},\alpha X)$ reaction as a function of excitation energy of the residual nucleus and a fitting result to Eq. 1 based on the Kozlowski spin relaxation model (solid line).

2.3 Analyzing power T_{20} for the $^6Li(\vec{d},\alpha)^4He$ reaction at an incident energy of 90 keV

T.Iizuka T.Furui T.Katabuchi and Y.Tagishi

The reaction $^6Li(d,\alpha)^4He$ at energies below the Coulomb barrier has been studied to understand nucleosynthesis in the early universe. The cross sections of the reaction $^6Li(d,\alpha)^4He$ at the low energies have been measured. From the experimental data of the cross sections, some researchers have suggested that the reaction $^6Li(d,\alpha)^4He$ may be dominated at low energies by a broad 2^+ subthreshold resonance in the compound nucleus ^8Be[1]. In the present work, we have first measured the tensor analyzing power T_{20} of the $^6Li(d,\alpha)^4He$ reaction at an incident energy of 90 keV for more understanding of the reaction mechanism for this reaction.

The emitted alpha particles were detected simultaneously by five silicon photodiodes (HAMAMATSU S2744) placed in a scattering chamber at every 20° from +40° to -40° in the laboratory system. Each anode of photodiodes was connected with a resistance in series and each cathode was also connected in series without resistance. We could clearly distinguish signals from each counter by applying a position detecting method with charge division (Fig.1) and also energy signal of each counter was obtained from cathode. The solid angle of each counter was 20 msr, which corresponded to a detector angular acceptance of $\Delta\theta$=3°.

Experiments were performed with 90-keV polarized deuteron beam from a Lamb-shift type polarized ion source at UTTAC. The target of ^6Li was prepared by vacuum evaporation of $^6Li_2CO_3$ onto a 15-μm-thick aluminum foil, whose thickness was about 10 μg/cm^2. The energy loss of the incident deuterons in the $^6Li_2CO_3$ target was estimated about at 5 keV. The deuteron beam was stopped by the aluminum backing. Measurements were made on the polarized-beam injection line by setting a small scattering chamber just after a quadrupole magnet followed by a Wien filter. The analyzing power T_{20} was obtained by measuring each cross section of the incident deuteron beams with the m_I=+1 and m_I=0 deuteron magnetic substates from the polarized ion source for the spin-quantization axis parallel to the beam direction. The obtained angular distribution of the analyzing power T_{20} is shown in Fig. 2. As shown in Fig. 2, the center of the detector-arrangement was shifted toward approximately 5 degrees from the incident beam line. A more systematic measurements are now in progress.

References

[1] K. Czerski et al., Phys. Rev. C55, 1517 (1997)

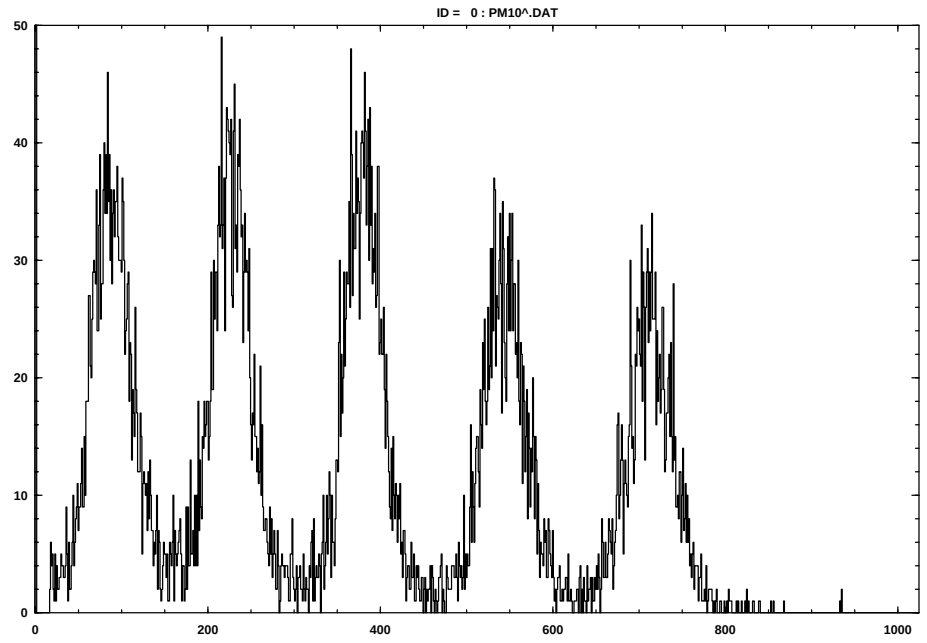

Fig. 1. Position spectrum from the photodiode counter array. Each peak corresponds to the signal from each photodiode counter.

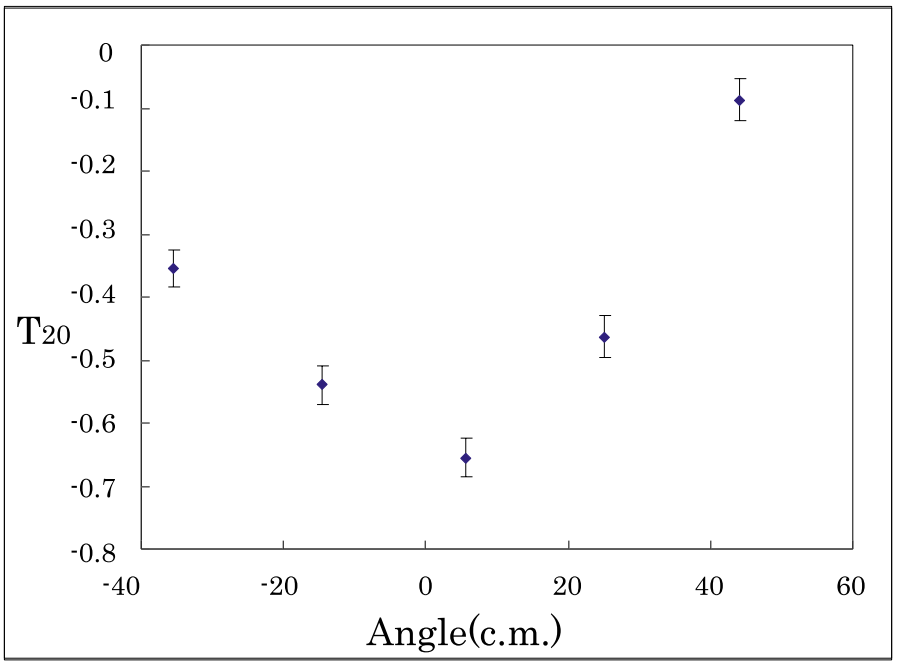

Fig. 2. Angular distribution of the analyzing power T_{20} of the reaction $^6\mathrm{Li}(\vec{d},\alpha)^4\mathrm{He}$ at $E_d = 90keV$.

2.4 Measurement of proton total reaction cross sections for ^{nat}Si near the ^{28}Si(p,n) threshold energy (II)

N. Okumura, T. Joh, Y. Honkyu, K. S. Itoh[1] and Y. Aoki

An energy dependence of proton total reaction cross sections on ^{nat}Si and ^{27}Al nucleus was reported in ref. [1]. A resonance like behavior is observed in the case of ^{nat}Si around ^{28}Si(p, n) threshold energy (15.7 MeV). On the contrary, the total reaction cross sections of ^{27}Al target increase monotonously with the energy in the range from 14 to 17 MeV. In this energy region, numerical data on proton elastic scattering cross sections are available [2]. The optical model calculation, which reproduced these elastic data, fails to predict the resonance behavior.

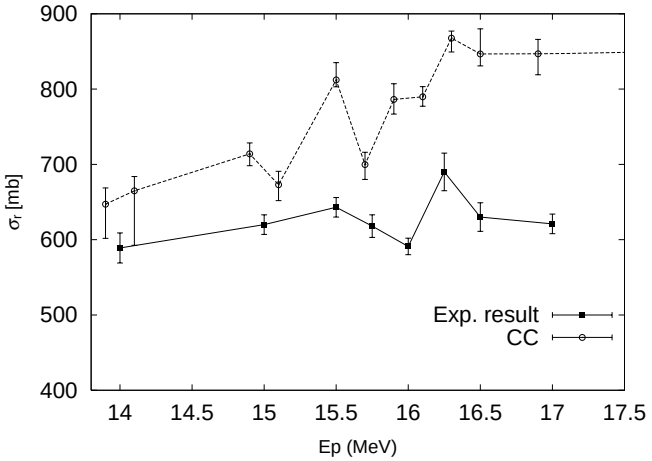

Fig. 1. Comparison of coupled channels analysis (CC) with the experimental data.

Allowing for a possibility of higher order effects, coupled channels calculation was tried. In this calculation, potential parameters which can reproduce the elastic and inelastic scattering cross sections from ref. [2] was searched. The inelastic scattering data was limited to the cross sections leading to the 1st excited state in ^{28}Si. Coupled channels calculation, which we used CHUCK2 code [4], solves the following set of coupled equations,

$$\{\frac{d^2}{dr^2} - \frac{\ell(\ell+1)}{r^2} + (k^2_{\alpha'} - U^I_{\alpha'\alpha'}(r))\}u^{\alpha}_{\alpha'}(r) = \sum_{\alpha''\neq\alpha'} U^I_{\alpha'\alpha''}(r)u^{\alpha}_{\alpha''}(r). \quad (1)$$

Suffices α' and α'' denote sets of channel quantum numbers. The superscript α shows the entrance channel. The ^{28}Si(gnd.), ^{28}Si(2^+_1) and (p,n) states are included in this calculation. Total reaction cross section $\sigma_{\rm r}$ can be expressed as

$$\sigma_{\rm r} = \int_0^{\infty} \sigma_{\rm r}(r)dr \quad (2)$$

$$= \frac{2\pi}{k^3}\sum_{\ell j}(2j+1)\int_0^{\infty} Im\{u^{\alpha\pi I*}_{\alpha}\sum_{\alpha'} U_{\alpha\alpha'}u^{\alpha\pi I}_{\alpha'}\}dr. \quad (3)$$

Following form of coupling potentials are assumed, i.e.,
for the coupling with ground and ^{28}Si(2^+_1) state,

$$U(\text{gnd.} \rightarrow \text{1st}) = \frac{2m_\alpha}{\hbar^2}\sum_{n=1}^{2}\left\{V_n\frac{d^{(n)}f(X_R)}{dX^{(n)}_R} + iW_n\frac{d^{(n)}f(X_I)}{dX^{(n)}_I}\right\}, \quad (4)$$

[1]Cyclotron and Radioisotope Center, Tohoku University, Sendai 980-8578, Japan

where $f(X_R)$ and $f(X_I)$ are Wood-Saxon type function and m_α is the channel reduced mass, and for the (p,n) reaction,

$$U(\mathrm{p} \to \mathrm{n}) = \frac{2m_\alpha}{\hbar^2} V \frac{\exp(-\mu r)}{r} \qquad \text{or} \qquad \frac{2m_\alpha}{\hbar^2} V \delta(|r - r_0|), \tag{5}$$

respectively. The result of this analysis is compared with the experimental data (fig. 1). A resonance like behavior in the calculation can be seen around the (p,n) threshold energy, The error bar of the coupled channels calculation shows the range where the χ^2 is increased by 1/3 from the minimum χ^2. To compute this range, the strength of the imaginary part of the potential is changed.

The integrand $\sigma_{\mathrm{r}}(r)$ in eq. (2) is named absorption distribution in [3]. Upper panel of fig. 2 shows $\sigma_{\mathrm{r}}(r)$. Peaks around 4 fm means that the absorption takes place near the surface region of

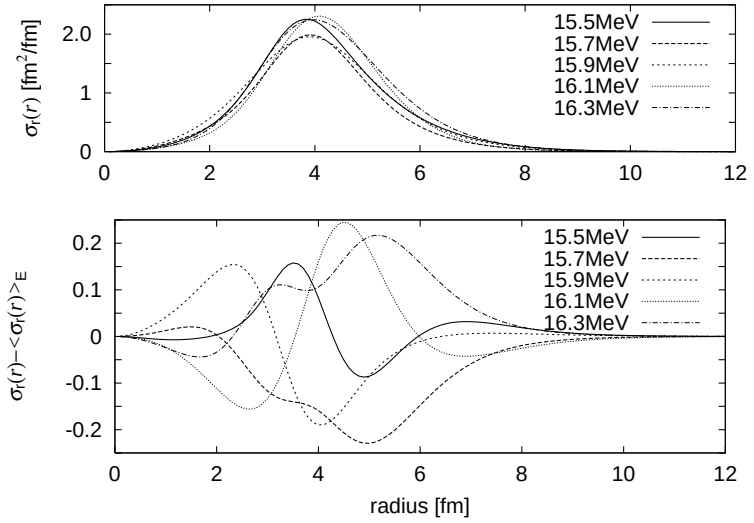

Fig. 2. The upper panel of the figure shows the absorption distribution around the threshold energy. The lower panel shows the absorption distributions, where energy averaged absorption distribution is subtracted.

the target nucleus. The peak value is a little smaller for 15.5 and 15.7 MeV than the rest. The lower panel shows the energy dependence of the deviation of $\sigma_{\mathrm{r}}(r)$ from the energy averaged one ($\langle\sigma_{\mathrm{r}}(r)\rangle_E$). This figure shows that the 15.7 MeV curve has a large negative value near the nuclear surface. At 15.9 MeV the dip near the nuclear surface is drawn into the center by about 1 fm and the dip change sign and pushed out to nuclear surface when the incident energy is increased to 16.1 and 16.3 MeV. This energy dependence of absorption distribution can clearly be seen using absorption radius as the first moment of the absorption distribution [3],

$$r_{abs} = \frac{\langle r\sigma_{\mathrm{r}}(r)\rangle}{\langle\sigma_{\mathrm{r}}(r)\rangle}. \tag{6}$$

Fig. 3 shows the energy dependence of the absorption radius due to the coupled channels analysis. The absorption radius becomes about 0.1 fm smaller around 15.6 MeV. If the geometrical cross section is estimated with the absorption radius, this decrease in the absorption radius corresponds to 30 mb reduction. The experimental data of total reaction cross section in the ref. [1] has a dip whose depth is about 50 mb. So the absorption radius shows the same tendency as the experimental total reaction cross section.

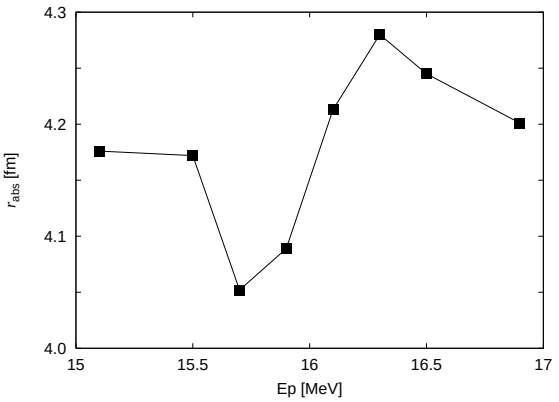

Fig. 3. Energy dependence of the absorption radius $r_{\rm abs}$.

References

[1] N. Okumura, N Takahashi, T. Joh, Y. Honkyu, M. Kitazawa, K. S. Itoh and Y. Aoki, UTTAC annual report (1999) 35

[2] K. Hirota, ^{28}Si(p,p) data, *private communications*

[3] Y. Aoki, K. Hirota, H. Kishita, K. Koyama, M. Masaki, K. Miura, Y. Mukouhara, S. Nakagawa, N. Okumura and Y. Tagishi, Nucl.Phys. A**599**,417(1996)

[4] P. D. Kunz, *computer code* CHUCK2, *private communications*

2.5 Toward proton-proton scattering at forward angles (III)

T. Joh, K. S. Itoh, N. Okumura, Y. Honkyu, M. Aramaki and Y. Aoki

The study of p-p differential cross section at energies around 20MeV has been continued [1]. It was reported in ref [1] that the proton elastic spectrum is degraded by a beam halo and slit edge scattering. An effort was made to improve the quality of the spectrum by installing a slit with four jaws, which can be moved independently. By reading the beam current intensities, which hit these four jaws, are used to establish a good beam transportation. A typical momentum spectrum obtained with the new set up is displayed in Fig. 1.

This spectrum was taken at a laboratory angle of +4 degree with a proton beam energy of 22MeV. The prominent peak in this spectrum is due to the p-p scattering. The continuous tail observed at the low-momentum side decreased to 0.2% level. Protons elastically scattered from contaminant carbon and /or oxygen are negligible. There remains left/right asymmetry in elastic yield at 4 degree. It was noticed that there was a little misalignment of target chamber and a magnetic spectrograph. This misalignment was corrected to less than 0.1 mm.

We are now directing our effort to the operation of monitor counter. It is a plastic scintillator coupled with a 1/2” photo multiplier tube. It is located at 25 degree right from the target center.

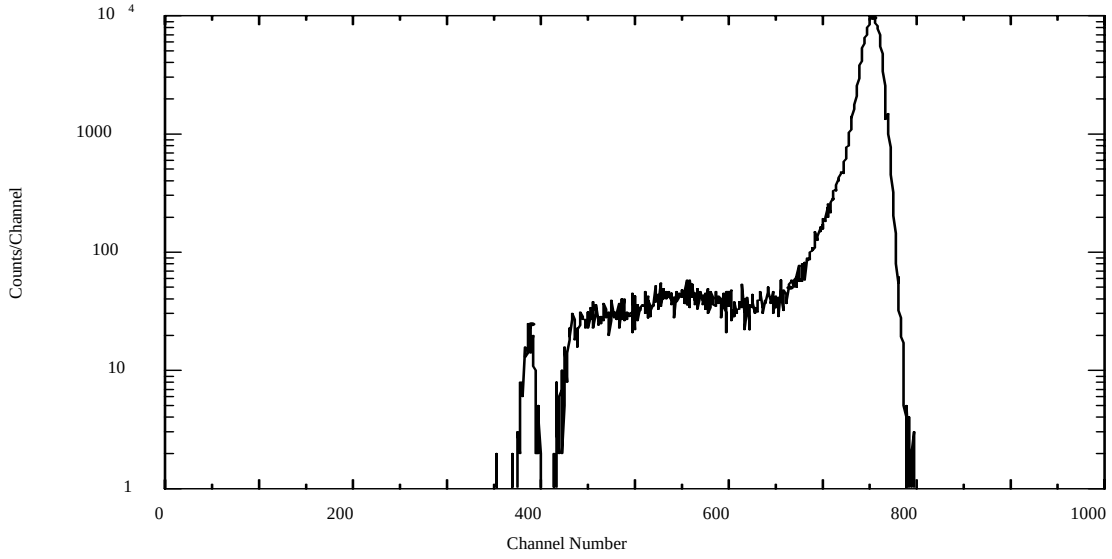

Fig. 1: momentum spectrum of ^{1}H(p,p) at 22 MeV

Reference

[1] T. Joh, K.S. Itoh, N. Okumura, N.Takahasi, Y. Honkyu, M. Kitazawa and Y. Aoki, UTTAC annual report (1999) 38

2.6 Measurement of the proton spectrum in deuteron break-up reaction

Y. Honkyu, N. Okumura, K. S. Itoh[1)], T. Joh, M. Aramaki, and Y. Aoki

We have developed a counter system to measure proton spectra in deuteron break-up reactions[1, 2]. It is a 1300 mm long position sensitive detector and is designed as a focal-plane detecter for an Enge-type Split Pole magnetic spectrograph (ESP90)[3].

Fig.1 shows the current version of the counter assembly. It consists of two position-sensitive detectors and an energy detector. The position-sensitive detectors are single wire proportional counters (SWPC). The anode wire is 12.5 μm in diameter, and is 1200 mm long. The anode-to-cathode gap is 5 mm wide. The cathode is made of 4 μm thick aluminized myler. The counter gas is a mixture of 70% Ar and 30% methane. Position information can be extracted by charge-division method. The energy counter is composed of a plastic scintillator and two photomultiplier tubes. The plastic scintillator is about 900 mm long, and its thickness of 15 mm is enough to stop protons and deuterons. Two photomultiplier tubes are set on both sides of the scintillator.

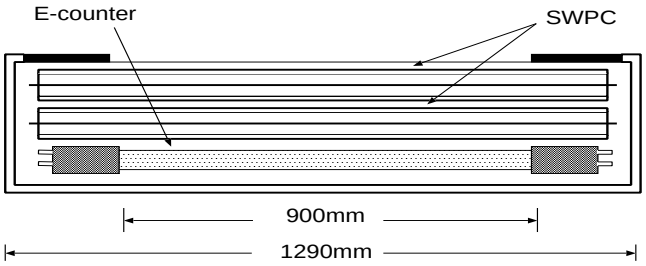

Fig. 1. Counter assembly

Off-line tests were carried out for the SWPC using 5.9keV X-rays from ^{55}Fe source. The position resolution of the SWPC was improved from 2.4 mm to 1.5 mm(FWHM).

A proton spectrum in deuteron break-up reaction was measured by using 18 MeV deuterons and ^{208}Pb target(3.89 mg/cm^2). The data were taken in five-degree steps from θ_{lab}=20° to 55°. Triple coincidence in two SWPC and the energy detector was observed to determine proton events. A typical two dimensional coincidence spectrum is displayed in Fig.2. Fig.3 shows the proton momentum spectrum obtaind by projecting the two-dimensional spectrum onto the position axis. Protons in the figure come partly from the break-up reaction (d,pn) and partly from (d,p) reactions. Fig.4 shows the double differential cross section.

References

[1] Y.Sinbara and S.Kuroki, Thesis, Tsukuba University, (1997)

[2] N. Takahasi, K. S. Itou, N. Okumura, T. Joh, Y. Honkyu, M. Kitazawa, K. Hirota[1] and Y. Aoki , UTTAC annual report (1999) 22

[3] J.E.Spencer and H.A.Enge, Nucl. Instr. and Meth. **49**, (1967), 181

[1]Laboratory of Nuclear Science, Tohoku University

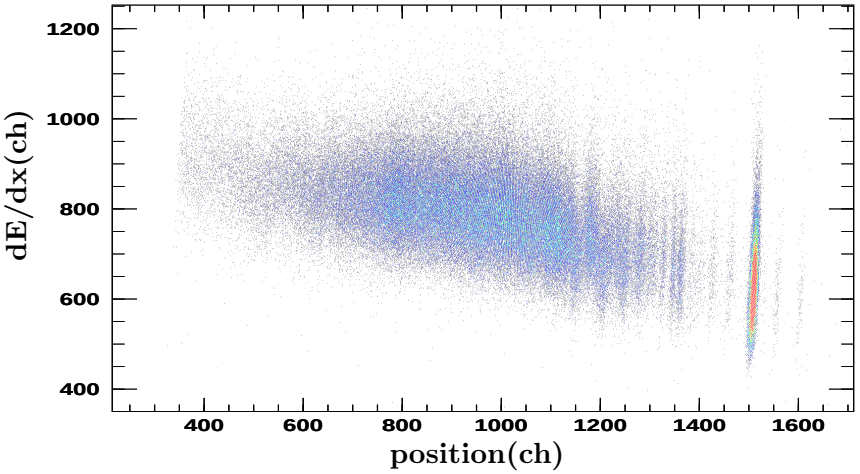

Fig. 2. Two dimensional spectrum
Inelastic scattering for d+^{208}Pb and θ_{lab}=30°at E$_d$=18 MeV

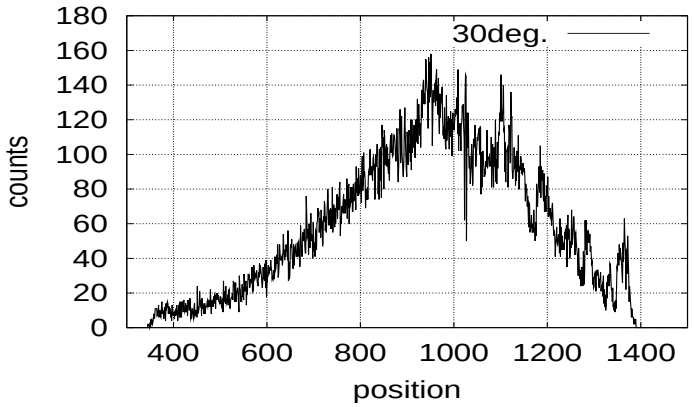

Fig. 3. Momentum spectrum

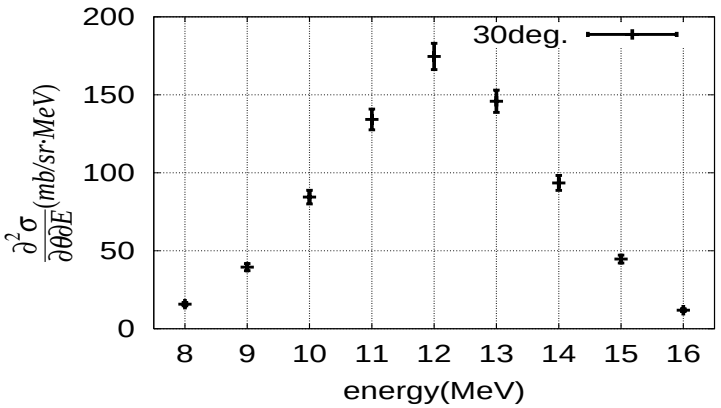

Fig. 4. Double differential cross section
Inelastic scattering for d+^{208}Pb and θ_{lab}=30°at E$_d$=18 MeV.

2.7 Yrare Bands in ^{119}Xe

C.-B. Moon[1], T. Komatsubara , Y. Sasaki, T. Jumatsu, K. Yamada, K. Satou, and K. Furuno

The transitional nuclei, such as Xe and Ba in the A=120-130 mass region have attracted much attention since they provide the useful information helped to understand, in the framework of the cranking model, the polarizing effect of the valence quasiparticles on the nuclear shape. In this mass region the proton Fermi surface lies in the lower part of the $h_{11/2}$ subshell while the neutron Fermi surface lies in the $h_{11/2}$ midshell. Thereby, the nuclei in this mass region are soft with respect to γ, the triaxiality parameter in the polar description of quadrupole shapes. Total Routhian surface (TRS) [1,2] and cranked shell model (CSM) [3, 4] calculations suggest that these high-j valence particles exert a strong and specific driving force on the γ–soft core: particles in the lower part of the $h_{11/2}$ subshell favor a collectively rotating prolate shape ($\gamma \geq 0^0$ in the Lund convention) while those in the middle part of the $h_{11/2}$ subshell favor a collectively rotating triaxial shape ($\gamma \approx -30^0$).

In the even-mass Xe nuclei in this mass region, low-lying γ-vibrational bands have been observed that show a pronounced energy staggering between odd and even spin states. This has been interpreted in terms of a gamma-soft nuclear potential in their low-lying states. In the odd-mass Xe isotopes, the unique-negative parity $h_{11/2}$ neutron orbital forms the yrast rotational band and their signature splitting features can be nicely described by cranking calculations. In the mean time, the second negative-parity rotational bands based on the high-j $h_{11/2}$ neutron orbital, they are called the yrare bands, were observed in ^{121}Xe [5], ^{123}Xe [6], and ^{125}Xe [7]. In contrast to the behaviour of the yrast bands where the favored states should be lying lower in energy, the yrare favoured states are seen to be energetically unfavoured, namely the signature splitting is inversed. Such signature inversion in the yrare bands seems to be quite general in the light odd-mass Xe isotopes. With features in mind, although several studies on high-spin states in ^{119}Xe [8,9,10,11] were done, we tried to investigate excited states for observing the yrare bands in ^{119}Xe. In the present work, we report the yrare bands in ^{119}Xe and discuss signature inversion seen in the light odd-mass Xe isotopes.

The level structure was studied with the ^{107}Ag(^{16}O, p3n)^{119}Xe reaction at a beam energy of 85 MeV. The beam was provided by the 12UD tandem accelerator at the University of Tsukuba. The target was a self-supporting foil of ^{107}Ag, 6.6 mg/cm^2 in thickness. The γ-ray spectra were taken with 11 high-purity (HP) Ge detectors with BGO anti-Compton shields (ACS). One of them was the LEPS (low energy photon spectrometer) detector to ensure sensitivity for important low-energy transitions at the bottom parts of γ-ray cascades.

Figure 1 shows the partial level scheme of ^{119}Xe where only the negative-parity states are represented. The ordering of the γ-ray transitions has been determined from coincidence relationships and relative

[1]Department of Physics, Hoseo University, Chung-Nam 336-795, Korea

intensities.

Band 1, favored yrast states, built on the $11/2^-$ state and its signature partner band 2, unfavoured yrast states, were already known in the previous works [8-11]. In the present work, we confirmed up to the $43/2^-$ state. In a recent work by Scraggs et al. [11], this favoured yrast band was established up to $83/2^-$.

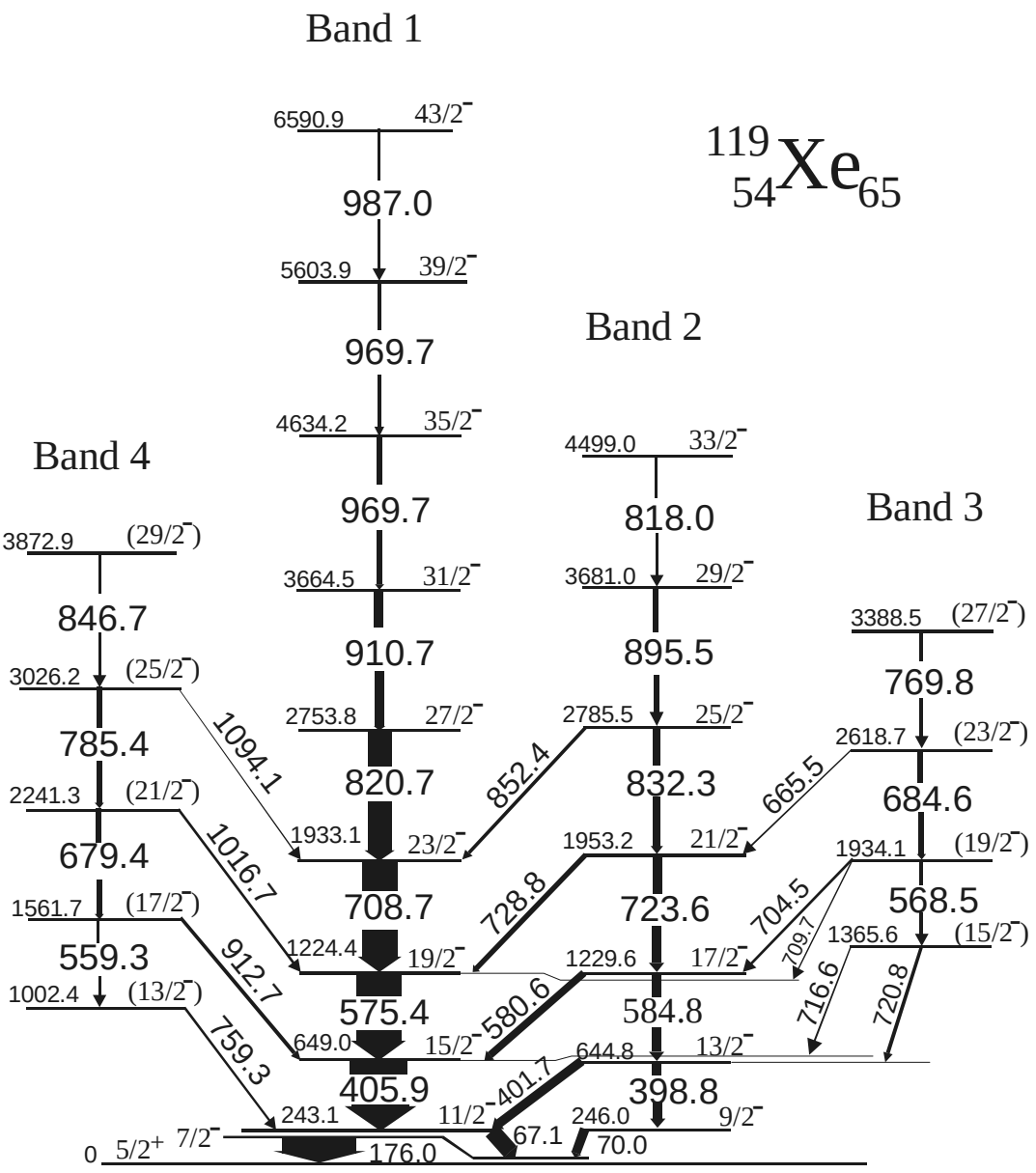

Fig. 1. Partial level scheme of ^{119}Xe showing the negative-parity states populated from the ^{107}Ag (^{16}O,p3n) ^{119}Xe reaction at E_{lab} = 85 MeV. Excited and transitional energies are given in keV.

Bands 3 and 4, to which we assign negative parity, were newly identified in the present work. The population intensity for bands 3 and 4 is estimated to be 11 % and 18 %, respectively relative to that of

the $15/2^-$ - $11/2^-$ 406 keV transition in band 1. Thereby, the favoured yrare states, band 3, are less populated than the unfavoured yrare states, band 4. Band 4 is connected to the yrast favoured states through several interband transitions, namley the 759-913-1017-1094 ones while band 4 is connected to both the yrast favoured and unfavoured states. Meanwhile, the interband transitions from band 3 are rather strongly populated to the unfavoured yrast band than to the favoured yrast band. The proposed spin and parity assignments are essentially based on the multipolarity of the interband transitions connecting to the yrast bands 1 and 2. The DCO ratios indicate that the 913, 1017, and 1094 keV transitions connecting band 4 to the favoured yrast band are $\Delta I = 1$ transitions with mixed M1/E2. The 721, 705, and 666 keV transitions connecting band 3 to band 2 are also of dipole character indicating $\Delta I = 1$ transitions with mixed M1/E2. So we propose that bands 3 and 4 should have negative-parity states. Bands 3 and 4 are called the favored and unfavored yrare states. It is seen that the low spin signatures for the unfavored yrare bands are inverted as compared with those in the yrast bands. Surprisingly, the critical inversion-spin, $I_c = 12\hbar$ at which the normal signature splitting is restored, was observed, which is the first observation in the odd-A Xe.

References

[1] R. Wyss, J. Nyberg, A. Johnson, R. Bengtsson, W. Nazarewicz, Phys. Lett. B 215 (1988) 211.

[2] W. Nazarewicz, R. Wyss, A. Johnson, Nucl. Phys. A 503 (1989) 285.

[3] R. Bengtsson, S. Frauendorf, Nucl. Phys. A 327 (1979) 139.

[4] R. Bengtsson, S. Frauendorf, F.-R. May, At. Data Nucl. Data Tables 35 (1986) 15.

[5] C.-B. Moon, T. Komatsubara, T. Shizuma, K. Uchiyama, T. Sasaki and K. Furuno, Eur. Phys. J A 4 (1999) 107.

[6] A. Schmidt, I. Schneider, H. Meise, I. Wiedenhöver, O. Stuch, K. Jessen, D. Weisshaar, C. Schumacher, P. von Brentano, G. Sletten, B. Herskind, M. Bergstrom, J. Wrzesinski, Eur. Phys. J A2 (1998) 21.

[7] Granderath, D. Lieberz, A. Gelberg, S. Freund, W. Lieberz, R. Wirowski, P. von Brentano and R. Wyss, Nucl. Phys. A 524 (1991) 153.

[8] P. Chowdhury, U. Garg, T.P. Sjoreen and D.B. Fossan, Phys. Rev. C 23 (1981) 733.

[9] V. Barci, J. Gizon, A. Gizon, J. Crawford, J. Genevey, A. Plochocki and M.A. Cunningham, Nucl. Phys. A 383 (1982) 309.

[10] V.P. Janzen, M.P. Carpenter, L.L. Riedinger, W. Schmitz, D.G. Popescu, J.A. Cameron, J.K. Johansson, D.D. Rajnauth, J.C. Waddington, G. Kajrys, S. Monaro and S. Pilotte, Phys. Rev. C 39 (1989) 2050.

[11] H.C. Scraggs, E.S. Paul, A.J. Boston, J.F.C. Cocks, D.M. Cullen, K. Helariutta, P.M. Jones, R. Julin, S. Juutinen, H. Kankaanpää, M. Muikku, P.J. Nolan, C.M. Parry, A. Savelius, R. Wadsworth, A.V. Afanasjev and I. Ragnarsson, Nucl. Phys. A 640 (1998) 337.

[12] K. Loewenich, K.O. Zell, A. Dewald, W. Gast, A. Gelberg, W. Lieberz, P. von Brentano, Nucl. Phys. A 460 (1986) 361.

2.8 Band structures in the doubly odd nucleus ^{130}Cs

Y.-J. Ma, Y.-H. Zhang, Y. Sasaki, K. Yamada, H. Ohshima, S. Yokose, M. Ishizuka, T. Komatsubara and K. Furuno

1. Introduction

There have been extensive investigations on high-spin structures of odd-odd nuclei in the A ~ 130 mass region. Rich experimental data on band structures and transition probabilities obtained with recent Ge-detector arrays have revealed a number of interesting features of the nuclear structure in this mass region like the signature inversion at low spins.

Neutron deficient odd-odd Cs isotopes are well investigated up to high spins by several authors[1-3]. Since even-even nuclei in this region change in their shape from a deformed shape at the neutron-deficient side to spherical shape near the N = 82 closed shell, high-spin band structures in odd-odd nuclie would also exhibit a systematic behavior with the increase of the neutron number according to the softness for gamma deformation of the core and the variety of the couplings in the extra-core neutron and proton.

The nucleus ^{130}Cs has 75 neutron; it located between the well deformed and the spherical region. Since the last extra-core neutron occupies the $h_{11/2}$ orbital having high-Ω as the increase of the neutron number, it is expected that a dipole band might be observed in addition to the usually observed competition of the collective excitations with the single-particle excitations. However, the high-spin sates in ^{130}Cs are less studied in comparison with lighter Cs isotopes. This is partly because of the difficulty in the production *via* a dominant exit channel of fusion-evaporation reactions with A > 11 projectiles.

Previously, Sala et al. reported three rotational bands of ^{130}Cs [4]. The yrast band was observed up to 14^+ state; the configuration was assigned to $\pi h_{11/2}\otimes\nu h_{11/2}$, but no backbending was observed. The configurations of other two bands were assigned to $\pi g_{7/2}\otimes\nu h_{11/2}$ and $\pi d_{5/2}\otimes\nu h_{11/2}$. During the progress of this study, some new results of ^{130}Cs became available from a recent publication by Starosta et al [5].

2. Experimental details and data analysis

In the present work high-spin states in ^{130}Cs have been studied through two separate experiments successively performed at Tandem Accelerator Center, University of Tsukuba (UTTAC). In the first experiment ^{130}Cs was produced via the ^{124}Sn(^{10}B, 4n) reaction at a bombarding energy of 47 MeV, and in the second one via the ^{124}Sn(^{11}B, 5n) reaction at 58 MeV. The same target and same detection system were used in the two different experiments. The target was a self-supporting 4.6 mg/cm^2 metallic foil, enriched in ^{124}Sn to 99%. The detection system was an array consisting of nine Compton-suppressed HPGe detectors and one planar HPGe detectors. Energy and efficiency calibrations of these detectors were made using ^{152}Eu and ^{133}Ba sources. γ-γ coincidences were measured and the events were collected when at least two detectors fired in coincidence within 100 ns. In addition, single spectra were also measured in each experiment. Approximately 140 and 100 million coincidence events were collected in the first and second experiments, respectively.

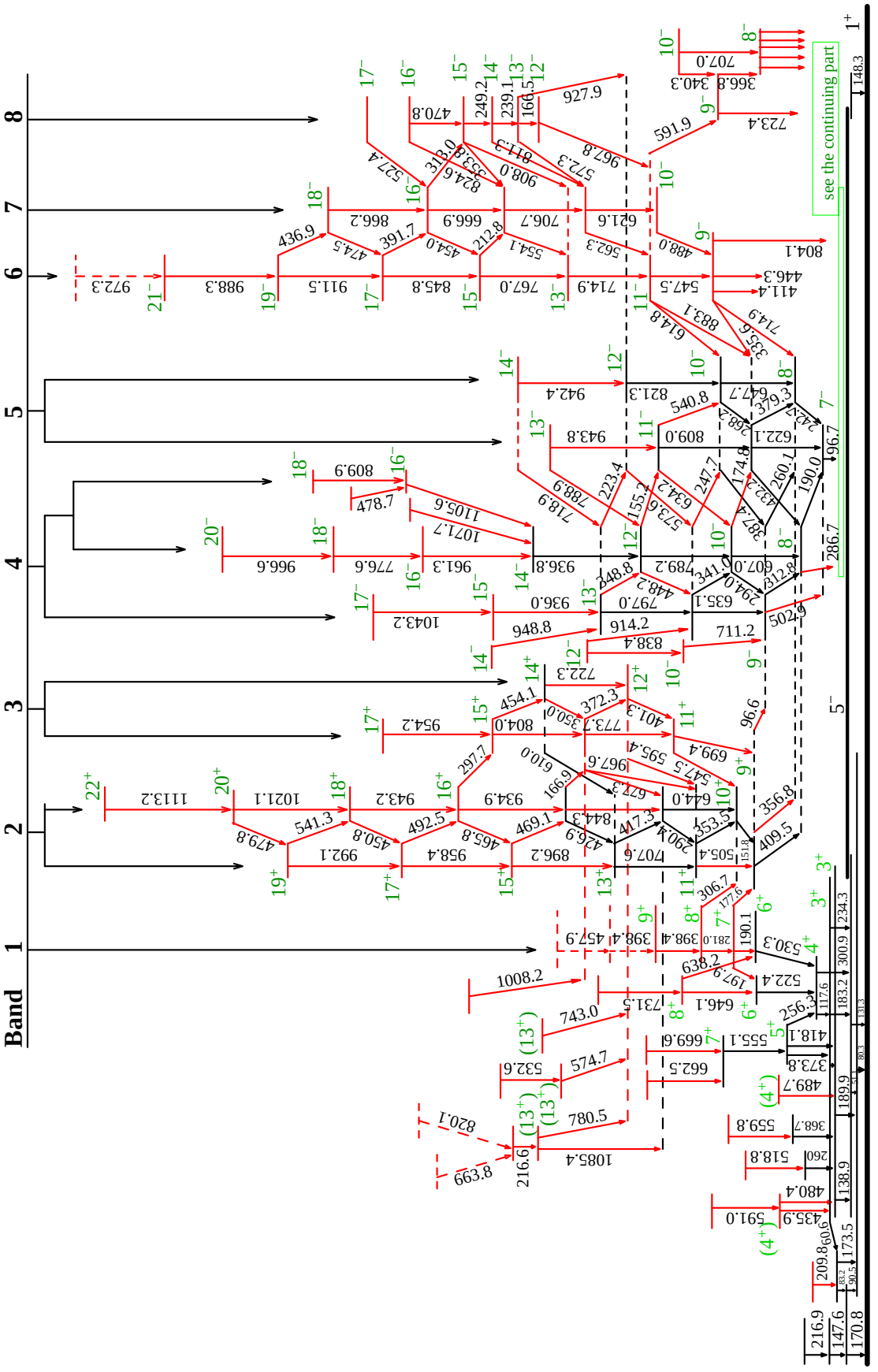

Figure 1. Level scheme of ^{130}Cs deduced from the present work. (to be continued)

(Black lines denote previously known states or trnanstions, while red ones denote newly identified states or transitions.)

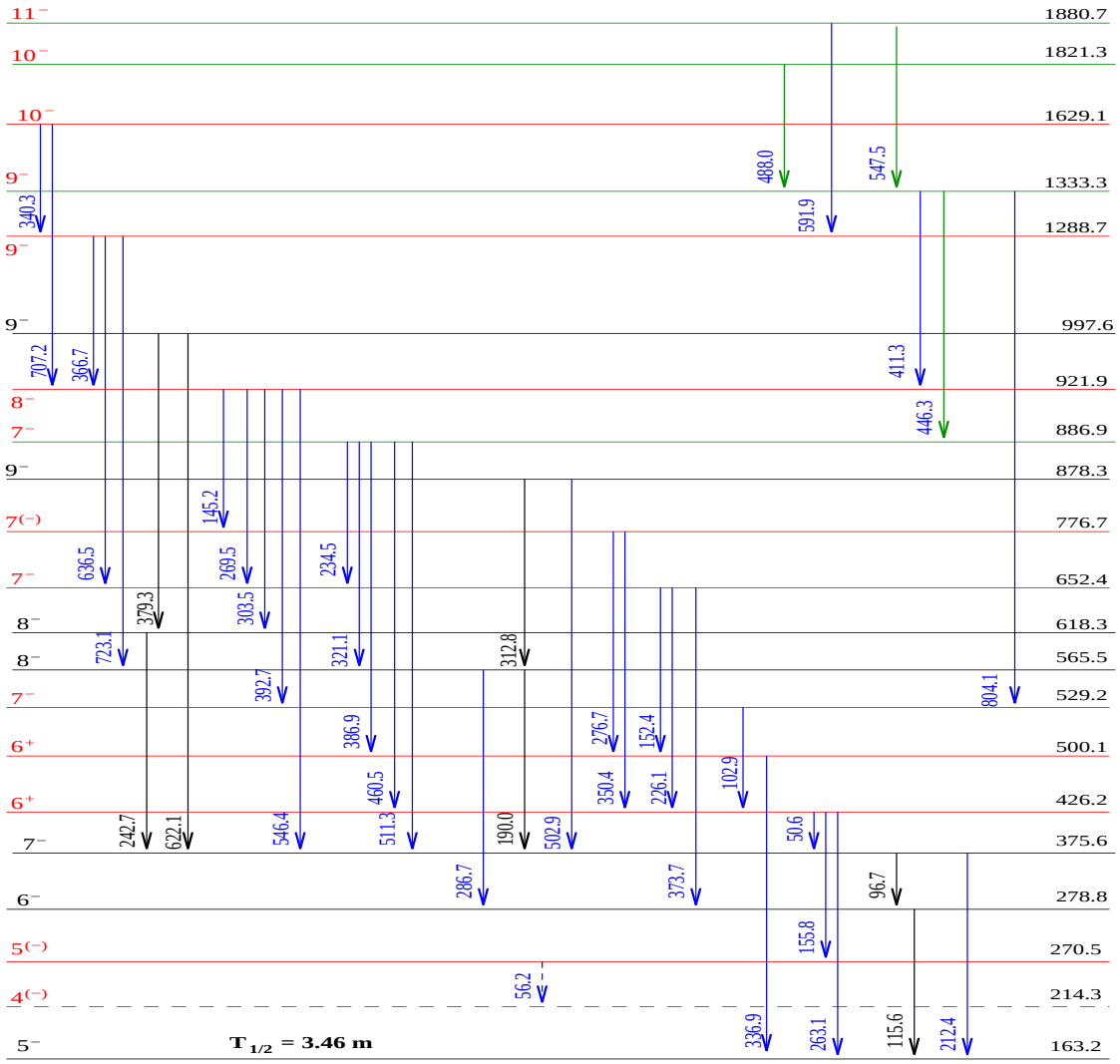

Figure 1 (continued). Level scheme of ^{130}Cs. (This part mainly displays the decays of band 6 to lower states)

In the off-line analysis, the spectra were corrected for the Doppler shift depending on the detector angle. They were then sorted into two separate two-dimensional E_γ-E_γ matrices corresponding to the two different experiments. A summed matrix of the above two matrices was also constructed to enhance ^{130}Cs as it appeared to be the most intensely populated residue both in the ^{10}B and ^{11}B induced reactions. All these matrices were symmetrized and were employed to deduce γ-γ coincidence relationships. Likewise, three asymmetric matrices were constructed for a purpose to extract the DCO ratios of γ transitions.

3. Results and discussions

The level scheme of ^{130}Cs deduced from the present work is shown in figure 1. With all the previously known [4] rotational bands extended to higher spins, several new bands have also been identified on the basis of prompt coincidence data. For the convenience of discussion, bands of interest in figure 1 are labeled with numbers.

3.1. Band 2, 4 and 5

Bands 2, 4 and 5 are the three rotational bands identified previously by Sala et al [4]. In their work, these three bands were observed up to spins I = 14, 14 and 12 respectively. Meanwhile, based on considerations of the parities of the respective bands and on nice agreements between the experimental and IBFFM (interacting boson-fermion-fermion model) level spectra, these bands were assigned to be based on the $\pi h_{11/2} \otimes \nu h_{11/2}$ $\pi g_{7/2} \otimes \nu h_{11/2}$ and $\pi d_{5/2} \otimes \nu h_{11/2}$ configurations, respectively. In the present work, bands 2 and 4 have been extended up to spins where the rotational alignment of a pair of quasiparticles occurs. The configuration assignments proposed by Sala et al are consistent with the observed alignment properties of these bands.

3.2. Band 3

In the previous work of Sala et al [4], a 610 keV transition was shown to feed the 13^+ state of the yrast band (band 2 in figure 1), in addition to the other feedings. In the present work this 610 keV transition has been identified as an out-of-band transition from another band, which is band 3 shown in figure 1. Moreover, we have also observed several other linking transitions, as can be seen from figure 1. Based on the measured DCO ratios of these linking transitions, band 3 is realized to have positive parity. Band 3 was also observed in the recent work by Starosta et al [5] and interpreted to be built on the same $\pi h_{11/2} \otimes \nu h_{11/2}$ configuration as the yrast band. Furthermore, they demonstrated that such sideband partner of the yrast band exists systematically in the N =75 isotones ^{130}Cs, ^{132}La, ^{134}Pr and ^{136}Pm, suggesting a common basis, for which they interpreted in terms of chiral vibration. In comparison with the data reported by them, in our data one additional transition (the 954 keV transition) has been placed on the top of band 3. In addition, two transitions with energy of 298 and 167 keV are observed to decay from the yrast band into the side partner band; see figure 1. Such an observation is interesting since no similar transition has ever been observed in the other three N=75 isotones.

3.3. Band 6 and 7

Bands 6 and 7 are two new bands disclosed from this work. They are connected quite strongly and band 6 de-excites towards the previously known lower states in a quite complicated decay pattern. The state fed by the 446 keV transition seems to be the bandhead of band 6. As its excitation energy is quite low, comparable to those of the other two-quasiparticle bands, it is thought to be also of two-quasiparticle instead of four-quasiparticle in nature at low spins. In addition, based on the experimental DCO data, band 6 as well as band 7 has been identified unambiguously to be of negative-parity. Taking into account these observations and the alignment property of band 6, we have tentatively assigned the $\pi h_{112/} \otimes \nu g_{7/2}$ configuration to band 6.

Band 7 is connected with band 6 quite strongly and this feature seems to suggest that it is the another signature of the $\pi h_{112/} \otimes \nu g_{7/2}$ band. However, an alternative assignment can not be completely excluded, i.e. the assignment of $\pi h_{112/} \otimes \nu d_{5/2}$ configuration.

3.4. Band 1 and 8

Band 8 appears to be a band-like structure consisting of only low-energy transition compared to the other normal rotational bands. Based on the experimental DCO data and the observation of a large number of linking transitions from band 8 to other known bands, we have been able to make firm spin and parity assignments for it, which indicate that it can be classified as a dipole band. Similar bands have also been observed in a number of nuclei in this region (see e.g. refs. [6,7]). The lowest observed state of band 8 has a high excitation energy (E_x = 2849 keV), which happens to be quite close to the excitation energy around which the EF alignment occurs in band 6 and 7, as well as in ^{129}Cs [7]. In view of this feature, we propose that band 8 is a four-quasiparticle band and the E and F quasineutrons are present in its configuration.

Besides band 8, band 1 also appears to be a dipole band, however they have quite different excitation energies. The band-head excitation energy of band 1 is only 962 keV, which is so low that it would be unreasonable to assign band 1 as a four-quasiparticle band. Dipole bands of two-quasiparticle in nature have also been suggested in several other odd-odd nuclei such as in ^{134}La, ^{136}Pr and ^{138}Pm (See ref. [8] and refs therein). It is worth emphasizing that we have in one nucleus found two types of dipole band, which are of two- and four-quasiparticle in nature respectively.

4. Summary

In brief summary, high spin states in ^{130}Cs have been studied through the reactions ^{124}Sn(^{11}B, 5n) at a beam energy of 58 MeV and ^{124}Sn(^{10}B, 4n) at 47 MeV. Previously know rotational bands have been extended to higher spins, and several new bands have also been established. The possible configurations of the newly identified bands are discussed briefly. Further work of this study is in progress.

References

[1] C.-B. Moon, T. Komatsubara, K. Furuno, Nucl. Phys. A674, 343 (2000)

[2] T. Komatsubara et al., Nucl. Phys. A557, 419c (1993)

[3] E. S. Paul et al., Phys. Rev. C 40, 619 (1989)

[4] P. R. Sala et al., Nucl. Phys. A531, 383 (1991)

[5] K. Starosta et al., Phys. Rev. Lett. 86, 971 (2001)

[6] T. Hayakawa et al., Z. Phys. A 357, 349 (1997)

[7] L. Hildingsson et al., Z. Phys. A 340, 29 (1991)

[10] U. Datta Pramanik et al., Nucl. Phys. A637, 327 (1998)

2.9 Level Structure of ^{118}I

C.-B. Moon[1], T. Komatsubara, T. Shizuma, Y. Sasaki, H. Ishiyama, T. Jumatsu, K. Yamada, and K. Furuno

The transitional nuclei with the A = 120 mass region have been extensively studied in the last years and the resulting experimental information helped to understand the polarizing effect of the valence quasiparticles on the nuclear shape. In this mass region the proton Fermi surface lies in the lower part of the $h_{11/2}$ subshell while the neutron Fermi surface lies in the $h_{11/2}$ midshell. These high-j valence particles exert a strong and specific driving force on the γ-soft core: quasiprotons in the lower part of the $h_{11/2}$ orbital favor a collectively rotating prolate shape at $\gamma \geq 0^0$ while quasineutrons in the middle part of the $h_{11/2}$ orbital favor a collectively rotating triaxial shape at $\gamma \approx -30^0$. In view of such driving effect, the doubly odd I nuclei have attracted attention since they provide an opportunity to understand the possible interaction and competing shape driving effects between proton and neutron quasiparticles in the high-j intruder $h_{11/2}$ orbitals.

The collectivity in the light I nuclei has been derived from the well-developed quadrupole deformation built on the neighboring even-even Xe core. In the light odd-A I, the yrast rotational bands were built on the $11/2^-$ state that is associated with the proton $h_{11/2}$ orbital. In the meantime, the yrast rotational bands based on the $\pi h_{11/2} \otimes \nu h_{11/2}$ configuration were observed in the light odd-odd I such as ^{116}I [1] and ^{118}I [2]. Interestingly, such $\pi h_{11/2} \otimes \nu h_{11/2}$ rotational bands in the odd-odd Cs nuclei reveal the signature inversion phenomena, which the excitation energy in unfavored signature states is lower than that in favored signature states [3].

Although several investigations for the level structure of ^{118}I by using in-beam spectroscopy were done [2, 4, 5], reliable spin-parity assignments for the observed rotational bands could not be established since the bands observed in this nucleus were not connected and thus remain isolated from each other. In the present work, we report the new results for the level scheme of ^{118}I.

The level structure has been studied with the ^{103}Rh (^{18}O, 3n) ^{118}I reaction at a beam energy of 85 MeV. The beam was provided by the 12UD tandem accelerator at the University of Tsukuba. The target of ^{103}Rh was a self-supporting foil of 6.8 mg/cm^2 in thickness. The γ-ray spectra were taken with seven high-purity (HP) Ge detectors with BGO anti-Compton shields. The level scheme of ^{118}I deduced from the present work is shown in Fig. 1. The ordering of the γ-ray transitions has been determined from coincidence relationships and relative intensities. Information on γ-ray multipolarities was obtained from DCO ratios, $R = I_\gamma(37^0)/I_\gamma(79^0)$.

Bands 1 and 2 have been known in previous works [2, 4, 5] and interpreted as the strongly coupled rotational bands built on the $\pi g_{9/2} \otimes \nu h_{11/2}$ configuration. The band-head 7^- state with the half-life of 8.5 m, however, has not been known its excitation energy. In the present work, we propose that the excitation energy of the 7^- state should be 188.8 keV. This result comes from the definite determination for the

[1]Department of Physics, Hoseo University, Chung-Nam 336-795, Korea

excitation energy of the 10^- state in band 6 and the observation of a linking transition of 406.6 keV from the 10^- state at 942.6 keV to the 9^+ state at 536.0 keV, which finally decays to the 7^- state through a pathway of the 224.6 keV transition.

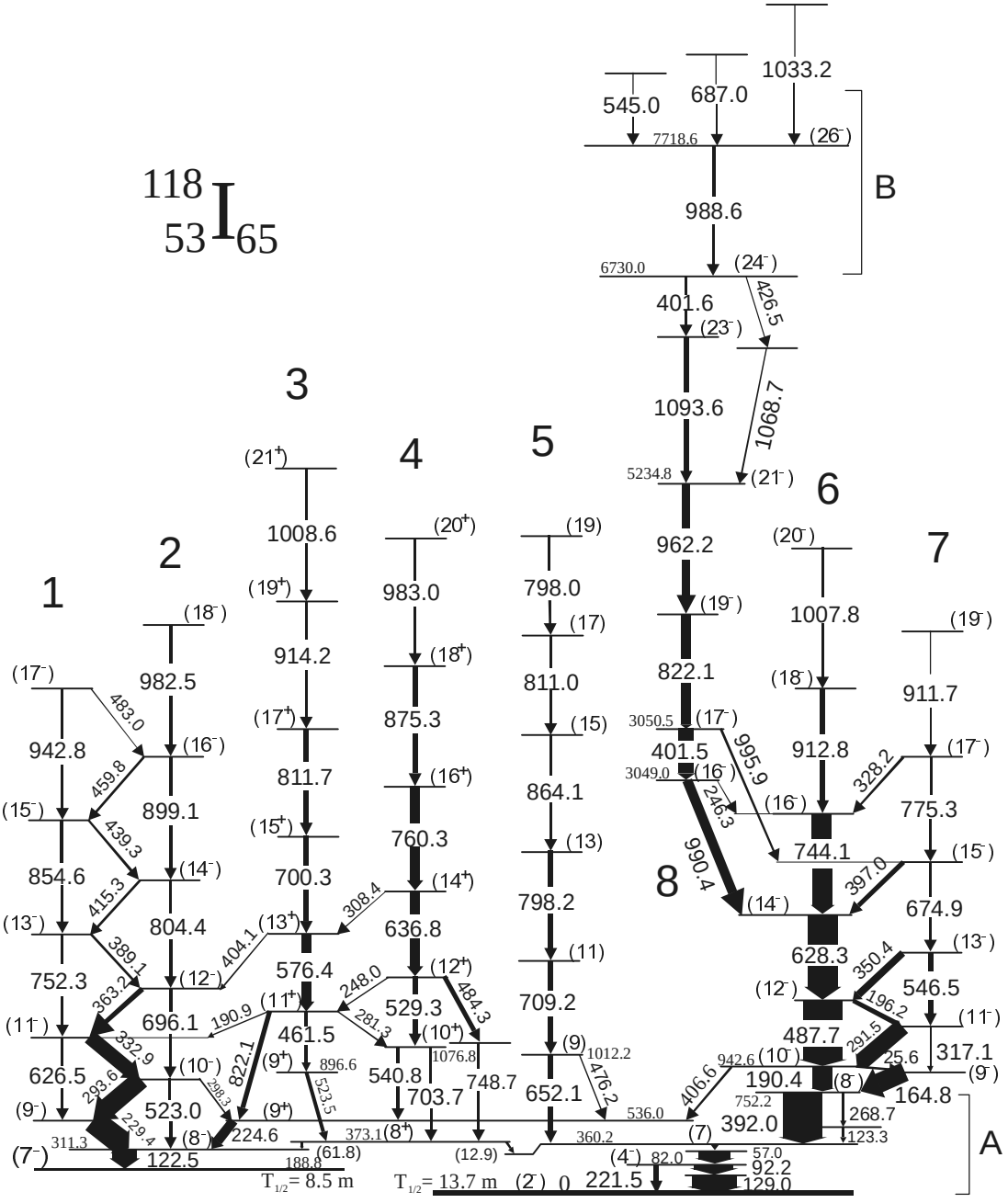

Fig. 1. Level scheme of ^{118}I deduced from the reaction of ^{103}Rh(^{18}O, 3n) ^{118}I at E_{lab} = 85 MeV. Transition and excitation energies are given in keV. The widths of the arrows correspond roughly to the intensities of the γ-ray transitions.

Bands 3 and 4, to which we assign positive parity, was already identified by Paul et al. [2] as a deformed rotational band built on the $\pi h_{11/2} \otimes \nu h_{11/2}$ configuration. Such a configuration was obtained by

the blocking arguments for the quasiparticle spin alignment. In the present work, we confirmed their result and determined the excitation energies.

Band 5 was newly identified in the present work. This band shows a regular sequence of E2 transition up to the 15 state where its structure changes showing a quasiparticles alignment.

Band 6, which is the yrast band, and its signature partner, band 7 were already reported in [2, 5]. The excitation energy and spin assignmet to the state of band head, however, could not be established. Noncollective low spin states below the 8^- state at 752.2 keV, labeled A, consist of the complicated transitions. The ground state of ^{118}I has been know to have the spin and parity of 2^- with a magnetic dipole moment 2.0 nm and a half-life, $T_{1/2}$ = 13.7 m [6]. We suggest that low spin transitions labeled A should be built on the ground state. Bands 6 and 7 could be interpreted as the $\pi g_{7/2} \otimes \nu h_{11/2}$ quasiparticle structure.

Band 8 was reported in [4] but the ordering of the transitions are quite different from each other. Considering the coincidence relationships and intensities of the γ-ray transitions, our result is more reliable. This band can be built on the four quasiparticle excitation and the 24^- state may be interpreted in terms of a noncollective oblate state with the full configuration of $[\nu g_{7/2} \otimes \pi h_{11/2} \otimes (\nu h_{11/2})^2]$.

References

[1] E.S. Paul, D.B. Fossan, K. Hauschild, I.M. Hibbert, H. Schnare, J.M. Sears, I. Thorslund, R. Wadsworth, A.N. Wilson, and J.N. Wilson, J. Phys. G: Nucl. Part. Phys. 21 (1995) 995.

[2] E.S. Paul, D.B. Fossan, K. Hauschild, I.M. Hibbert, H. Schnare, J.M. Sears, I. Thorslund, R. Wadsworth, A.N. Wilson, and J.N. Wilson, J. Phys. G: Nucl. Part. Phys. 22 (1996) 653.

[3] T. Komatsubara, K. Furuno, T. Hosoda, J. Mukai, T. Hayakawa, T. Morikawa, Y. Iwata, N. Kato, J. Espino, J. Gascon, N. Gjørup, G.B. Hagemann, H.J. Jensen, D. Jerrestam, J. Nyberg, G. Sletten, B. Cerderwall, P.O. Tjøm, Nucl. Phys. A 557 (1993) 419c.

[4] M.A. Quader, W.F. Piel, S. Vajda, W.A. Watson III, F.C. Yang, and D.B. Fossan, Phys. Rev. C 30 (1984) 1772.

[5] Harjeet Kaur, J. Goswamy, Jagbir Singh, A. Sharma, D. Mehta, Nirmal Singh, R.K. Bhowmik, P.N. Trehan, Z. Phys. A 350 (1994) 183.

[6] Table of Isotopes, 8th Edition, Wiely, 1996.

2.10 Preliminary measurement of the g-factor of the second excited state in ^{165}Ho

K. Furuno, K. Yamada, Y. Sasaki, S. Yokose, J. Y. Ma and T. Komatsubara

The experimetal data of the graound-state band of the nucleus ^{165}Ho are compiled in ref[1]. The ground state has the spin-parity of $I^\pi = 7/2^-$. The spin-parities and the halflives are reported to be $I^\pi = 9/2^-$ and 20.0(4) ps for the first exctied state at 94.7 keV; those of the second excited state at 115.1 keV are $I^\pi = 11/2^-$ and 12.8(6) ps. As regards nuclear g-factors, the value of $g = 1.01(1)$ is given to the ground state. The g-factor of the first excited state is measured to be $g = 0.91(4)$ using Mössbauer effect[2]. No other g-factor is reported for excited states.

We have measured the g-factors of the first and the second excited state of ^{165}Ho by means of ion-implanted time-integral perturbation method. The target consisted of 4 layers. A backing foil was prepared by rolling a 3 μm iron foil(Fe) on a 2μm copper(Cu) foil. To obtain firm contact of these two foils, a thin indium(In) foil was inserted in between Fe and Cu foils. A 500 μg/cm^2 thick Ho layer was evaporated in vacuum onto the surface of the Fe foil. Another foil consisting of Ho and Cu layers was made for the measurement of angular distribution without magnetic perturbation. The excited states of ^{165}Ho were produced by Coulomb excitation with ^{32}S beam at energies of 68.8 and 90.1 MeV delivered by the 12UD tandem accelerator. Back scattered ^{32}S ions were detected with an annulat-type silicon surface-barrier detector. Gamma rays were observed with 4 Compton-supprssed Ge detectors placed at angles of $\pm 63.5^\circ$ and $\pm 116.5^\circ$ with respect to the beam. A small permanent magnet was used to magnetize the Fe foil. The magnitude of the field produced by this magnet was measued to be 0.084 T at the target position.

Precession angles were derived from the standard double-ratio method and slope factors. The analysis of these data was performed according to the prescription described in ref[3]. In general, Larmor precession angles due to the perturbation at higher levels must carefully be included in the evaluation of the precession angle of a level of interest. We assumed that only two levels were populated, since the Coulomb excitation was very weak for levels higher than the 3rd excited state. With this assumption, the precession angles for the 1st and 2nd excited state can be written as

$$\theta_1 = (a\, g_1 + b\, g_2)\frac{\mu_N}{\hbar} B\, \tau_1 \qquad \text{and} \qquad \theta_2 = g_2 \frac{\mu_N}{\hbar} B\, \tau_2,$$

where g_1 and g_2 are the g-factors of the 1st and 2nd excitted states, τ_1 and τ_2 denote the mean lifetime, B stands for the effective magnetic field, μ_N is nuclear magneton. The parameters of a and b are the weight of the populations of the two states, and are given by

$$a = \frac{(N_1 + N_2)\tau_1}{(N_1 + N_2)\tau_1 + N_2\tau_2} \qquad \text{and} \qquad b = \frac{N_2\tau_2}{(N_1 + N_2)\tau_1 + N_2\tau_2}.$$

The populations of N_1 and N_2 were obtained from the intensities of the 94 and 115 keV γ rays. Using the known value of $g_1 = 0.91 \pm 0.04$, we obtained the g-factor of the second excited state to be $g_2 = 0.99 \pm 0.20$. The effective magnetic field B was also estimated to be 280 T. The value of the g-factor seems to be consistent with the prediction by the rotational model consisting of a deformed rotor and one proton. The effective magnetic field is, however, much smaller than the hyperfine field of Ho implanted in iron. It might be due to the small applied field of 0.084 T, which is inadequet for the saturation of the magnetization in the iorn foil. Further investivations are continued.

References

[1] R.S. Firestone and V.S. Shirley, Table of Isotopes, 8th edition, vol 2.
[2] E. Gerdau, W. Räth and H. Winker, Zeit. Phys. **257**(1972)29.
[3] O.Häusser, D. Ward and H. Andrews, Nucl. Instr. Meth. **169**(1980)539.

2.11 Measurements of fusion cross sections in the reactions of ^{82}Se + ^{138}Ba and ^{82}Se + ^{134}Ba

K.Sato, H.Ikezoe[1], K.Nishio[1] and S.Mitsuoka[1]

Evaporation residue (ER) cross-sections for the reactions of ^{82}Se+^{138}Ba and ^{82}Se+^{134}Ba were measured by using ^{82}Se beams from JAERI-tandem booster accelerator, where ^{138}Ba has the neutron closed shell of N=82 and ^{134}Ba has no such neutron closed shell. Main purpose of these experiments is to investigate how strongly the fusion process is affected by the nuclear shell structure. All evaporation residues produced in the present fusion reactions are α-emitting nuclei and their energy and lifetimes of α-decay are known in the literature [1]. Therefore we can identify each evaporation residue by detecting its α-decay energy and lifetime event by event.

The targets were made by sputtering a barium oxide on an thin aluminum foil of the thickness of 1.3μm. The abundances of the mass 138 in a ^{138}Ba target and of the mass 134 in a ^{134}Ba target are ≈100% and 73.5%, respectively. The thicknesses of the targets were measured by the energy loss of α particles (5.486 MeV) from a ^{241}Am source, where the energy loss of α-particles in the barium target was calculated by the code TRIM [2]. The measured thicknesses of ^{138}Ba and ^{134}Ba targets were 410 and 500 μg / cm^2, respectively. The targets were mounted on a rotating frame and were rotated during the beam irradiation to prevent breaking from heating by ^{82}Se beam.

The evaporation residues emitted in beam direction were separated in-flight from the primary and scattered beams by the JAERI-recoil mass separator (JAERI-RMS). The separated ERs were implanted into the double-sided position-sensitive strip detector (DPSD) mounted at the focal position of the JAERI-RMS. The energy resolution of the DPSD was 75 KeV. The time-of-flight signal (TOF) of incoming particles was obtained by two microchannel-plate detectors mounted in front of the DPSD and the other 30 cm upstream the DPSD, respectively. The TOF signal was used to distinguish the α decay events from the incoming particles. Moreover, the rough estimation of a mass number of the incoming particles was obtained by using a two-dimensional spectrum of the energy of the incoming particles versus the TOF signal. A silicon surface barrier detector was set at 45° with respect to the beam direction in the target chamber to measure the elastic scattering of the ^{82}Se beam from the barium targets. The elastic scattering events were used to determine the absolute values of the evaporation residues cross section.

We identified some specific channels by detecting ER-α1 and α1-α2 correlation chains, where α1 and α2 are the parent and daughter α decay event, respectively. The correlated event in position was identified under the condition (ΔX, ΔY)=(0.6, 0.6) mm, where the ΔX and ΔY are the position uncertainties in the horizontal (x) and vertical (y) directions. Fig. 1 shows a two-dimensional spectrum of α particle energy and the time interval between ER and α event, and Fig. 2 shows the two-dimensional spectrum of α1

1 Advanced Science Research Center, Japan Atomic Energy Research Institute, Tokai-Mura, Ibaraki 319-1195, Japan

energy versus α2 energy. In order to obtain the absolute cross sections of ERs, the transport efficiency of the ER through the JAERI-RMS was estimated by the method described in Refs. [3,4]. The estimated transport efficiency for each ER was obtained by taking into account the charge fraction calculated by Ref. [5]. The obtained transport efficiency was about 0.35 for the xn channel. Furthermore the probability of detecting the α decay of ER implanted in the DPSD was also estimated. The probability of full energy absorption of α particle from ^{216}Th was 0.64, for example, at the beam energy of 323 MeV.

Figure1

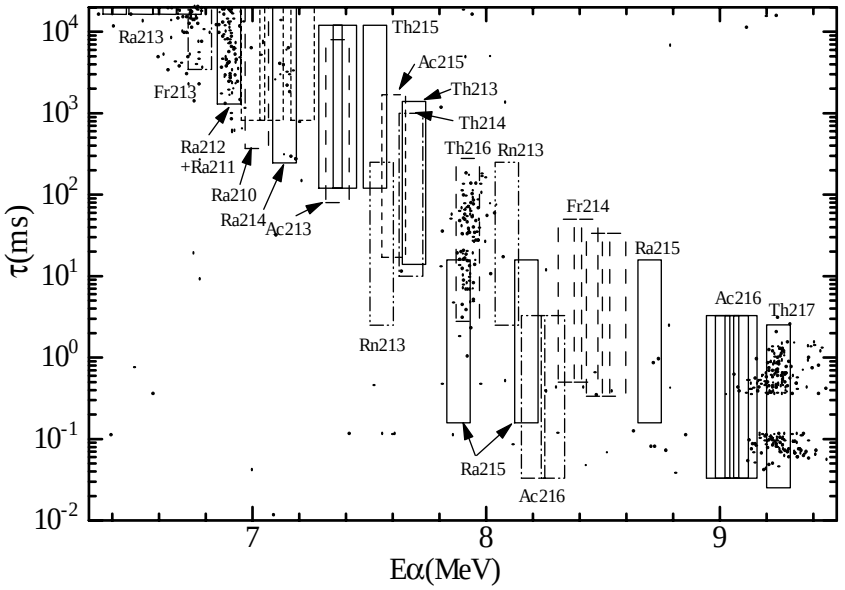

Figure 1

Two-dimensional spectrum of the energy versus the detected time interval between the α decay particle and the position-correlated ER, whose position difference was within ΔX=ΔY=0.6mm

Figure2

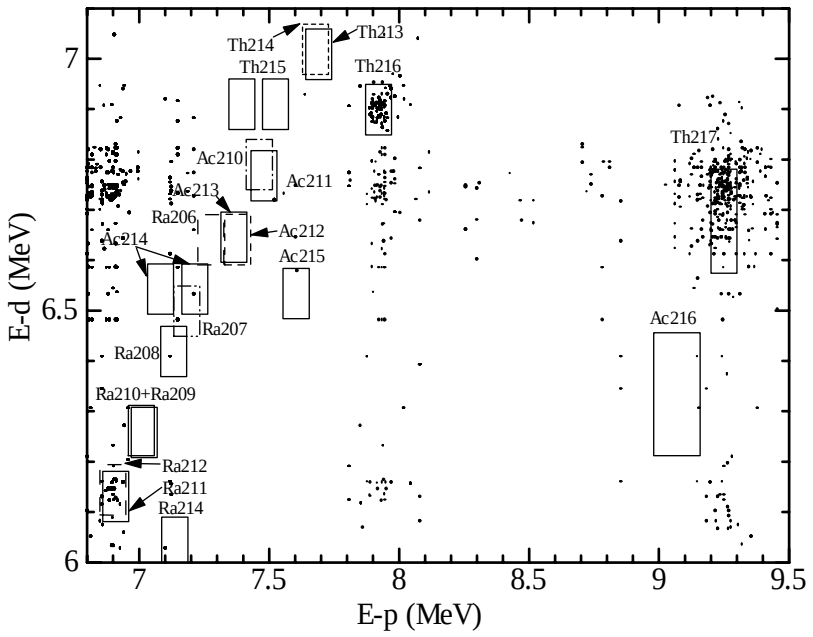

Figure 2

Two-dimensional matrix showing the correlated α1-α2 chain between parent and daughter α.

Boxes in Fig. 1 and in Fig. 2 indicate the eyes guide for each α-decay property of decay energy Eα and half lifetime $T_{1/2}$. (Eα - 50 KeV ≤ E ≤ Eα + 50 KeV, $T_{1/2}$ / 10 ≤ τ ≤ $T_{1/2}$ × 10)

The obtained evaporation residues cross sections (xn channels) for the reactions of $^{82}Se+^{138}Ba$ and $^{82}Se+^{134}Ba$ are shown in Fig. 3 as a function of c.m. energy determined in the middle of the target layer. The error includes both statistical and systematical contribution. The systematical uncertainty was 40% coming from the transport efficiency and charge distribution of ER.

Figure3

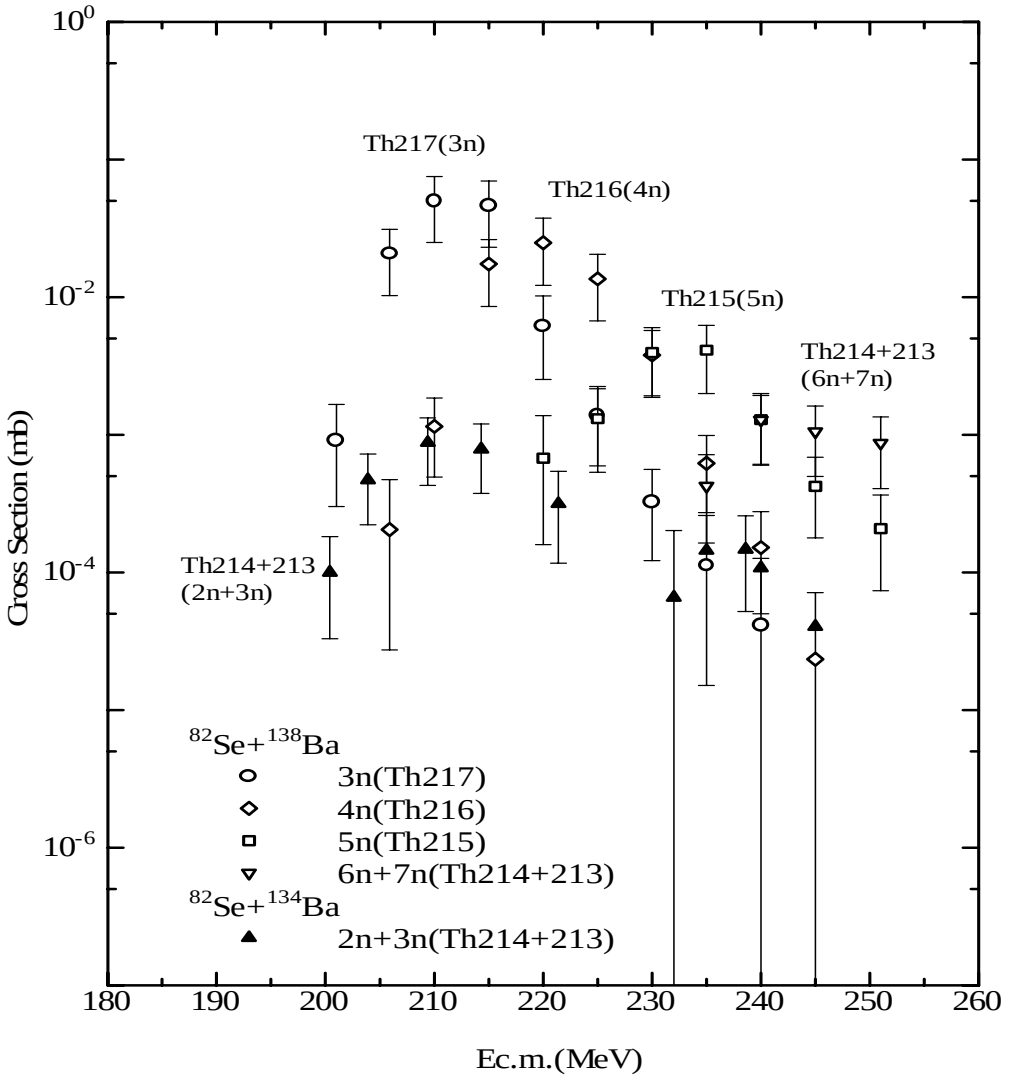

Figure3

Evaporation residues cross sections of xn channels for $^{82}Se+^{138}Ba$ and $^{82}Se+^{134}Ba$ reaction are shown together.

From Fig. 3, we can see that the 2n+3n cross sections in the reaction of $^{82}Se+^{134}Ba$ are about a hundred times smaller than the 3n cross sections in the reaction of $^{82}Se+^{138}Ba$ at the low energy region Ecm < 210 MeV. It is noted that at the high-energy region Ecm > 220 MeV the small contamination of heavier masses

138,137,136,135 of the present target (these contaminations are 5.26%, 1.94%, 4.03%, 15.24%, respectively) comes into play in the $^{82}Se+^{134}Ba$ experiment. The analysis is now proceeding by using the statistical model code HIVAP [6] to simulate the deexcitation process of the excited compound nucleus.

References

[1] R. B. Firestone et al.; Table of Isotopes 8th ed., New York, John Wiley, 1996

[2] The computer code to calculate the transport of ions in matter; see “The stopping and range of ions in solid” by J. F. Ziegler, J. P. Beersak, and U. Littnark, Pergamon Press, New York 1985

[3] K. Nishio, H. Ikezoe, S. Mitsuoka, and J. Lu, Phys. Rev. C 62, 014602(2000)

[4] T. Kuzumaki, H. ikezoe, S. Mitsuoka, T. Ikuta, S. Hamada, Y. Nagame, I. Nishinaka, and O. hashimoto, Nucl. Instrum. Methods Phys. Res. A 437, 107(1999)

[5] K. Shima, T. Ishihara, and T. Mikuno, Nucl. Instrum. Methods 200, 605

[6] W. reisdorf and M. Schadel, Z. Phys. A 343, 47 (1992)

2.12 Measurement of transient magnetic field by using polarized proton ions

T. Komatsubara, K. Sasa, T. Katabuchi, M. Yamaguchi, K. Kudo, K. Sawada, I. Masuno, T. Iizuka, H. Oshima, Y.J. Ma, Y. Sasaki, K. Yamada, S. Yokose, M. Ishizuka, M. Yoshimoto, Y. Tagishi, K. Furuno and T. Koyano [1]

For measurments of nuclear magnetic moments a transition magnetic field (TMF) is commonly used to obtain certain spin precessions in a wide range of nuclear mass region. When ions pass through a magnetized foil, nuclei of the ions feel strong magnetic field which is known as the transition magnetic field. However, velocity dependence of the field strength was studied only for some narrow velocity regions by measuring a precession angle determined by intensities of emitted gamma-rays. [1] In order to extend study of the TMF to higher velocity region, a new experiment has been started by using polarized proton beam.

For detection of proton spin precessions caused by the applyed TMF in a magnetized iron foil, spin directions were directly measured by use of nuclear reaction mechanism with polarized proton beam. Two proton polarimeters were located up-stream and down-stream of the magnetized iron foil. Both polarimeters consist of scattering targets of ^{12}C foil of 2mg/cm^2 thick and proton detectors at 45° in both left and right sides. Solid angles of proton detectors are 5.9 mstr for up-stream counters and 8.3 mstr for down-stream counters for the scattering ^{12}C targets, respectively. Incident beam energy was chosen to be 7.05 MeV to irradiate magnetized iron foil of 5μm thick. The beam was introduced to the up-stream ^{12}C target which is located at a distance of 77 mm up-stream of the iron foil. While a proton ion passed through the magnetized iron foil, direction of proton spin was rotated with degrading its kinetic energy to be 5.0 MeV by stopping power in the foil. The down-stream ^{12}C polarimeter was installed at 60 mm from the magnetized iron foil to measure the spin precession. In order to avoid multiple scattered protons, the down-stream ^{12}C target was covered by a copper window of 5 mm diameter.

The iron foil of 50 μm thick was prepared by annealing method at 970°C in 60 minutes under hydrogen atmosphere. A magnetic circuit was designed to apply sufficient extra magnetic field to magnetize the iron foil as shown in Fig.1. Eight small permanent magnets were located in both side in the magnetic circuit. The permanent magnets were cylindrical shape of 1.6 mm high and 3 mm diameter. Magnetic field was measured to be 2 kgauss on the surface. Fringing magnetic field was measured to be 100 gauss near the surface of the magnetized iron foil.

For the compensation of the inevitable fringing field, reference experiments were carried out by using copper foil. The other magnetic cicuit was prepared with a hole of 5mm diameter on the radiating position of the magnetized iron foil. The copper foil with the same thickness as the ion foil was covered on the hole so as to give the same stopping power for the proton beam. A number of permanet magnets was adjusted to be six to create simulating the fringing magnetic field.

In order to observe satulation of the magnetization of the iron foil, rf induction voltage was measured with changing external magnetic field. Two coils of 50 turns each were installed as shown in Fig.2. When an rf signal of 100kHz was appled to the excitation coil from an rf oscillator, V_{pp} of induction voltage on the pickup coil was measured. From these results shown in Table 1, eight permanent magnets were found to be enough to magetize the iron foil.

Analyzing powers for ^{12}C(p,p) reaction were measured with this system at the incident energy of 7.05 MeV and degreaded energy of 5.0 MeV with not-magnetized foils. Incident spin direction of polarized proton was chosen to be perpendicular to the scattering plane. Polarization of proton beam was measured to be 0.86 by quenching method. The analyzing powers were measured to be -0.30 for the up-stream counter and -0.84 for the down-stream counter, respectively. These

[1]Cryogenics Center

results were consistent to a previous report.[2]

For the measurement of the precession in the magnetized iron foil, two spin directions of polarized proton were chosen to be 0° and 180° those are parallel and anti-parallel to the beam axis. Fast spin flip operation system was used to change the proton spin and store individual spectra with the same integrated bean current. As a result of the experiment, precession angles are shown in Fig. 3. For the copper target, the precession angle is consistent to the fringing magnetic field. The extra precession observed for the iron target is derived by sum of the TMF and its magetization field. A time priod of the flight passing through the iron foil is calculated to be 1.45 [psec]. The corresponding strength of the magnetic field can be account to be 9 ± 4 [tesla] for the flight time.

Table 1 Induction voltage measured by pickup coil while 100kHz rf signal applied to excitation coil. An external magnetic field was induced by permanent magnets.

	Induction voltage V_{pp} [mV]
no iron foil	90
no magnet with iron foil	4900
8 magnets with iron foil	380
12 magnets with iron foil	315
16 magnets with iron foil	260

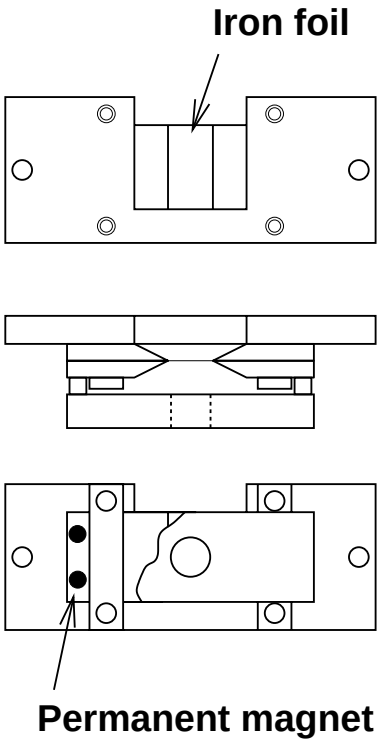

Fig. 1. An iron foil and a magnetic circuit.

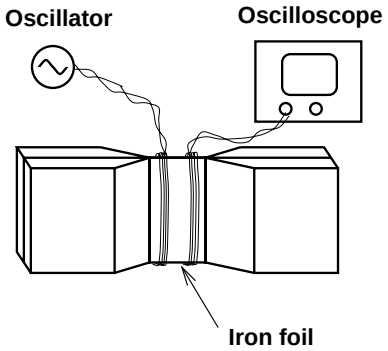

Fig. 2. An iron foil with exciation and pickup coils for the measurement of magnetization. Induction voltage was measured by changing a number of permanent magnets (which are not drawn in this figure).

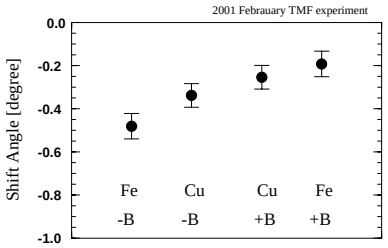

Fig. 3. Spin precessions of polarized proton beam pass through a magnetized iron foil depending on the direction of magnetization shown as +B and −B. Results for the copper foil are also shown for simulating the effect of the fringing magnetic field.

References

[1] M.P. Robinson, A.E. Stuchbery, E. Bezakova, S.M. Mullins, H.H. Bolotin, Nucl. Phys. A647 (1999) 175

[2] S.J. Moss and W. Haeberli, Nucl. Phys. 72 (1965) 417

3.1 Carbon KVV Auger electron emission from HOPG bombarded by fast protons

H. Kudo, K. Haruyama, T. Kinoshita, T. Azuma[1], S. Ishii, S. Seki[2]

We have continued the studies of ion-induced Auger spectra under the condition that the Auger yields depend on the layered structure of the target material, so that the commonly used macroscopic model of the Auger yield must be modified. Since Auger peaks are superposed on the continuum energy spectrum, precise analysis of the Auger yield requires knowledge on the continuum yield which results mainly from the binary-encounter processes [1]. Ion-induced electron spectroscopy at 180° with respect to the beam direction has a characteristic feature that the continuum energy spectrum is independent of the tilt angle of the target surface [2, 3]. The 180° electron spectroscopy therefore allows direct comparison of the electron spectra measured under oblique incidence conditions on the surface.

The sample we have used is highly-oriented pyrolytic graphite (HOPG), which has a layer structure of hexagon network of carbon atoms. The bond length in the network is 1.42 Å and the layer spacing is 3.35 Å. In the 180° electron spectroscopy, we observe carbon KVV Auger electrons of kinetic energy $E_{\rm A} = 260\,{\rm eV}$, which are emitted from the surface while bombarded by fast ions. When the HOPG surface is oblique to the ion beam, i.e., to the spectrometer direction, the measured Auger electrons produced inside the target move towards the surface and are refracted to 180° by the work function of $\phi \simeq 5\,{\rm eV}$.

The Auger peak height can commonly be related to the mean free path for inelastic scattering λ, which determines the attenuation of the elastically scattered Auger yield as $\exp(-z/\lambda)$, where z is the escape length of the electron. For incident direction of the ion beam with an angle θ from the HOPG surface, the relative intensity of the Auger yield $Y(\theta)$ is written

$$\begin{aligned} Y(\theta) &= \frac{1}{\sin\theta}\exp\left(\frac{-t}{\lambda\sin\theta_2}\right)\sum_{n=0}^{\infty}\exp\left(\frac{-nd}{\lambda\sin\theta_1}\right) \\ &= \frac{1}{\sin\theta}\exp\left(-\frac{t}{\lambda\sin\theta_2}\right)\left[1-\exp\left(-\frac{d}{\lambda\sin\theta_1}\right)\right]^{-1}, \end{aligned} \tag{1}$$

where θ_1 is related to θ by $\cos\theta_1 = (1 - e\phi/E_A)^{1/2}\cos\theta$, and t is the effective thickness of the electron distribution above the HOPG surface. θ_2 is the average emission angle at the surface, which is approximately given by $(\theta_1+\theta)/2$. The term $1/\sin\theta$ represents geometrical enhancement of the irradiated surface area. It is also assumed that the Auger electrons are produced at the atomic sites.

Figure 1 shows the values of $R = Y(\theta)/Y(90°)$ as a function of λ, calculated from eq.(1), for $\theta = 5.7$ and 10°, which correspond to $\theta_1 = 9.8$ and 12.8°, respectively. In this case, the values of t have been assumed to be $0.6d$ and d. Generally, $R \geq 0$ for $t = 0$. Also, R approaches $\sin\theta_1/\sin\theta$ as $\lambda \to \infty$, which corresponds to the macroscopic model of the Auger peak height.

In the experiments, a (0001) surface of HOPG has been prepared by peeling of the surface layer by an adhesive tape. The observations by an atomic force microscope in air assured that the fresh (0001) surface is atomically flat except for steps of a few monolayers, which are apart from each other by the order of a micronmeter. The HOPG samples were bombarded by a 1 MeV H^+ beam which were obtained from Tandetron at UTTAC. Under the present experimental conditions, the critical angle of HOPG(0001) planar channeling (∼0.42°) is much less than the values of θ noted earlier so that the specular reflection of the ions is unexpected to occur. The

[1]Tokyo Metropolitan Univ.
[2]SSL Tsukuba

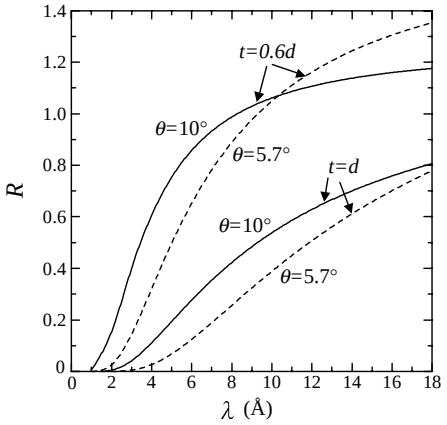

Figure 1: Calculated R as a function of λ. θ is the Auger emission angle relative to the HOPG surface.

electron measurements have been carried out using the 45° parallel-plate spectrometer of the double deflection type under the pressure of $\sim 3\times 10^{-7}$ Pa. Of course, the scattering effect of the emitted electrons by the steps should be minimized for observations at 180°. The measured

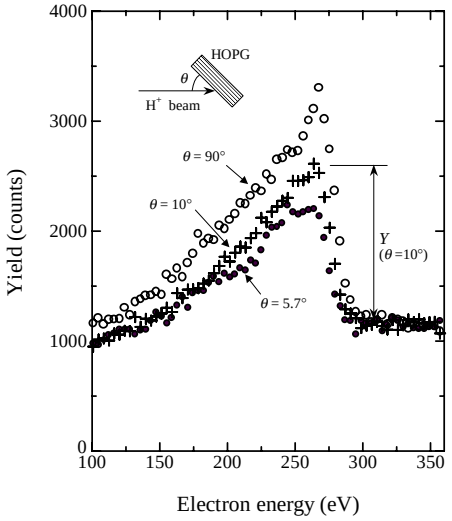

Figure 2: Electron energy spectra for $\theta = 5.7$ and 10°, measured for HOPG bombarded by 1 MeV H^+. The relative energy resolution of the spectrometer is ∼1%.

electron spectra for $\theta = 5.7$, 10, and 90° are shown in Fig. 2. The three spectra are plotted after they are normalized so that the continuum yields at 300–350 eV are equal. This assumption seems valid for the 180° electron spectroscopy, mentioned earlier. Furthermore, it is anticiaped that the smooth continuum spectrum should be less influenced by the scattering by valence electrons above the surface, noted earlier.

We see in Fig. 2 that the normalized Auger peak becomes lower with decreasing θ. The experimental values of R for $\theta = 5.7$ and 10° are 0.52±0.03 and 0.68±0.03, respectively. These values can be compared to the calculated results, shown in Fig. 1, taking into account that

$\lambda \simeq 10\,\text{Å}$ [4]. In this analysis, t may be regarded as an adjusting parameter. The observed values of R can be well reproduced for $t \simeq 0.8d = 2.7\,\text{Å}$. It should be noted that if the production sites of KVV Auger electrons are uniformly distributed in HOPG, i.e., not localized near the carbon nuclei, $t = 0$ must be assumed in eq. (1). In this case, $R(\theta)$ increases with decreasing θ from 90°, contrary to the observation. The experimental results therefore indicate that the KVV Auger production sites are localized near the carbon nuclei.

The analysis model used here is rather qualitative. However, the essential aspects of the phenomenon have been revealed from the present pexeriments, i.e.,

- The degraded KVV Auger peaks for emission in the oblique directions are due to the elastic and inelastic collisions with valence electrons distributed on the surface. Also, the Auger peak height reflects the layered structure of HOPG.
- Certainly, $R \geq 1$ for any θ if the Auger electrons are produced unformly in HOPG. However, the experiments indicate that $R < 1$. Detailed analysis of the experimental results should provide location of the preferential production sites of the valence Auger electrons in the layered structure.

References

[1] M. E. Rudd, Y. -K. Kim, D. H. Madison, T. J. Gay, Rev. Mod. Phys. 64 (1992) 441.

[2] H. Kudo, A. Tanabe, T. Ishihara, S. Seki, Y. Aoki, S. Yamamoto, P. Goppelt-Langer, H. Takeshita, and H. Naramoto, Nucl. Instr. and Meth. B 115 (1996) 125, and references therein.

[3] H. Kudo, *Ion-Induced Electron Emission from Crystalline Solids*, in press as a volume of 'Springer Tracts in Modern Physics', Springer-Verlag, Heidelberg, 2001.

[4] M. P. Seah, W. A. Dench, Surf. Interface Anal. 1 (1979) 2.

3.2 Ion-induced electron emission from damaged Si crystals

H. Kudo, M. Ohira, T. Kinoshita, K. Takeda, S. Seki[1]

Ion-induced electron spectroscopy in conjunction with ion channeling can be successfully used to structural analysis of crystalline solids under low beam dose conditions [1, 2]. This analysis technique provides structural information from the binary-encounter electron yield measured at 180° with respect to the beam direction. The purpose of the present expriments is to study an increase of the channeling electron yield due to the lattice disorder, whose depth distribution can be characterized by Rutherford backscattering spectroscopy (RBS) [3]. This should allow a better check of the analysis model.

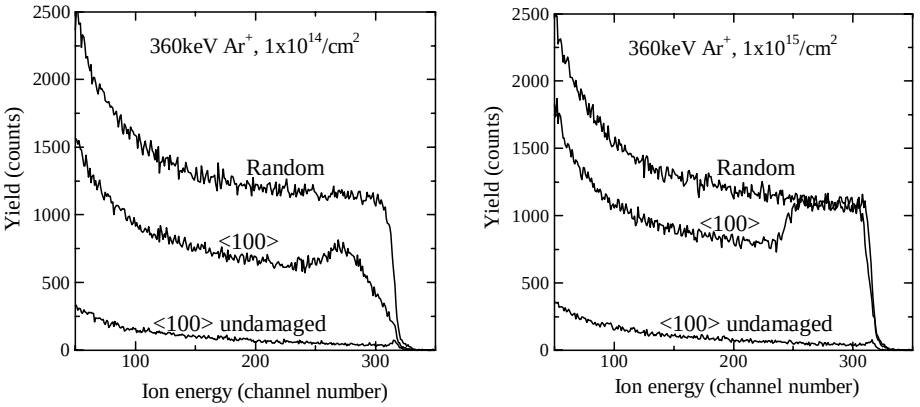

Figure 1: RBS spectra of damaged Si, measured with 2 MeV He^+ at 165°.

Si crystals were damaged by bombardment of 360 keV Ar^+ with beam doses of $1 \times 10^{14}\,cm^{-2}$ and $1 \times 10^{15}\,cm^{-2}$. Figure 1 shows RBS spectra measured with 2 MeV He^+ at a backward angle of 165°. For the damaged Si, the <100> channeling spectra clearly shows enhancement of the RBS yield, which results from the damaged layer ranging from the surface to a depth of ∼7000 Å, according to the energy-depth conversion using the ion stopping power.

The electron measurements have been carried out using 40 MeV O^{5+} and 56 MeV O^{8+} at UTTAC. The ratios of <100> to random (nonchanneling) electron yield W have been measured at 6.15 and 9.75 keV for 40 MeV O^{5+} and 56 MeV O^{8+}, respectively. These electron energies are higher than the corresponding values of the binary-encounter peak energies (5.43 and 7.61 keV, respectively), so that the measured yields stem mainly from Si inner-shell (mainly L-shell in this case) electrons. The values of W obtained are shown in Table 1.

For the beam dose of $1 \times 10^{15}\,Ar/cm^2$, the electron yield is close to unity. This can be accounted for by the effective escape depth of ±2000 Å, which has been determined from the electron measurements using overlayered Si crystals [2]. Actually, the RBS spectrum indicates that the Si crystal is seriously damaged from the surface to a depth of at least ±2000 Å. For the beam dose of $1 \times 10^{14}\,Ar/cm^2$, we have determined the values of z where W is equal to the integrated RBS yield $\mathcal{Y}(z)$, given by

$$\mathcal{Y}(z) \;=\; \int_0^z Y_c\,dz \,/\, \int_0^z Y_r\,dz, \qquad (1)$$

where Y_c and Y_r are the RBS yield for the channeling and random cases at z, respectively. The results obtained are 3800±230 and 3300±180 Å for 40 MeV O^{5+} and 56 MeV O^{8+}, respectively.

[1]SSL Tsukuba

Table 1: Experimental values of W for damaged Si. The values of the electron energies measured are noted in the text.

Projectile	1×10^{14} Ar/cm^2	1×10^{15} Ar/cm^2
40 MeV O^{5+}	0.264±0.011	0.949±0.038
56 MeV O^{8+}	0.214±0.009	—

These values are greater than the corresponding effective escape depths by a factor of 1.5–1.8. The discrepancy is probably due to the insufficient depth resolution of the RBS yield for the present analysis. High resolution RBS is needed for detailed comparison between the electron and RBS data.

References

[1] H. Kudo, T. Kumaki, K. Haruyama, Y. Tsukamoto, S. Seki, H. Naramoto, Nucl. Instrum. & Methods B174 (2001) 512.

[2] H. Kudo, *Ion-Induced Electron Emission from Crystalline Solids*, in press as a volume of 'Springer Tracts in Modern Physics', Springer-Verlag, Heidelberg, 2001.

[3] M. Ohira, Master thesis, University of Tsukuba, 2001.

3.3 New family member of active center created by multi-MeV ion bombardment of silica glass

Koichi Awazu[1], Satoshi Ishii and Kunihiro Shima

1. Introduction

In most insulators, the passage of swift (multi-MeV) heavy ions creates a heavily damaged, cylindrical zone known as the latent track. The majority of studies of latent tracks during the last 30 years or so were aimed at understanding the formation mechanism and a number of models have been proposed. Since the introduction rates of point defects due to nuclear collisions along the ion trajectory is far too small to explain the appearance of latent tracks, it is clear that the electronic stopping of the ions is responsible for the track formation. As a result of this electronic stopping, the wake of the ion contains a high density of energetic electrons. The proposed models differ in how, and how fast, these exited electrons transfer their energy to the atomic network. In the thermal spike model [1-3], the energy is rapidly and locally thermalized, leading to short-lived but extremely high temperatures along the ion track. In the ion spike or Coulomb explosion model [4,5], the ion track is denuded of electrons long enough for the mutual Coulombic repulsion of neighbouring atoms to occur. Hybrid models have also been proposed [6,7]. However, all these models focus on the very early stages of track formation and give little information on the expected atomic structure of the latent tracks. Moreover, the origin and structure of the defects responsible for the enhanced etch rate of the latent tracks have not been identified. Our experimental work described in this report attempts to improve our understanding of these latter issues by approaching the problem from a number of different angles correlating changes in infrared absorption with the etching enhancement in latent tracks.

Amorphous SiO_2 (hereafter a- SiO_2) has often been chosen as a target for ion implantation because the physical and structural properties of a- SiO_2 are well known [8]. In general, microscopic defects in a- SiO_2 as introduced by ion implantation can be classified in two types: paramagnetic centers on one hand, and non-stoichiometric defects such as oxygen deficient or excess centers on the other.

Macroscopic changes of a-SiO_2 resulting from radiation have been also reported by many authors. Bates et al.[9] reported that the densities of a-SiO_2 and α-quartz increased and decreased, respectively, upon neutron irradiation and that both materials stabilized at a nearly identical density of ~2.27 g/cm^3 after irradiation with 5×10^{19}n/cm^2 or more. Hiraiwa et al.[10] reported a frequency shift of the infrared (IR) absorption peak (ω_4) induced by ion implantation. This peak is associated with the asymmetric stretching mode of an oxygen atom in the Si-O-Si inter-tetrahedral bridge. They also reported that the shift $\Delta\omega$ of the frequency saturated at around –30cm^{-1} when the nuclear-deposited energy reached 3.4×10^{23}eV/cm^3, which is equal to the total Si-O bonding energy (3.8eV) in a unit volume of a-SiO_2.

The subject of the present work is to determine the defect(s) underlying the creation of individual conic holes in a-SiO_2. It was observed that a number of defect structures make up the latent track. We observed SiO_4 tetrahedra composed of planar three member rings, the E' center, and the oxygen deficient center in the latent tracks. We proposed that the planar three- and four member rings in latent tracks were responsible for the enhanced etching rate. Neither the E' center nor the oxygen deficient center exhibit any influence on the etching rate.

2. Experimental

Ion bombardment was performed at room temperature and at a residual pressure below 1×10^{-4} Pa. A 6 MV tandem accelerator in Université de Montréal was employed for irradiation with 10 MeV H^+, 15 MeV He^+, 2 MeV Li^+, 4 MeV C^+, 30 MeV Si^{6+} and 35 MeV Se^{6+}. We also used a 12 MV tandem accelerator in the Tandem Accelerator Center of University of Tsukuba (UTTAC) for irradiation with 120 MeV Br^{11+}, 127 MeV Br^{11+}, 98 MeV I^{12+} and 112 MeV I^{13+}. In order to avoid overlap of the individual conic holes that appear after chemical etching of latent tracks, very low ion fluences (typically 1×10^7 cm^{-2}) are required. This was achieved by diffusing the ion beam with either a C foil or an Au foil in either forward or back-scattering geometry. A variety of a-SiO_2 was used for these studies. Type III a-SiO_2 plates of 2 mm thickness, which contain 1000 ppm OH, were used for direct observation of latent tracks. Amorphous SiO_2 films 193 nm thick were thermally grown on (100) silicon wafers in O_2 atmosphere at 1000°C. The silicon

[1] Photonic Research Institute, National Institute of Advanced Industrial Science and Technology,1-1-1 Umezono, Tsukuba 305-8568, Japan

wafers used in the present experiment were prepared by the floating-zone method with resistance ~3000 Ω cm. These wafers of 200μm thickness were chemically polished on one side only in order to eliminate IR multiple interference effects. IR absorption was measured with a Fourier transform IR (FT-IR) spectrophotometer using light at normal incidence. Visible individual holes were created from the irradiated samples by chemical etching with 48% hydrofluoric (HF) acid and were observed with a scanning electron microscopy (SEM) at an angle 45° from electron incidence.

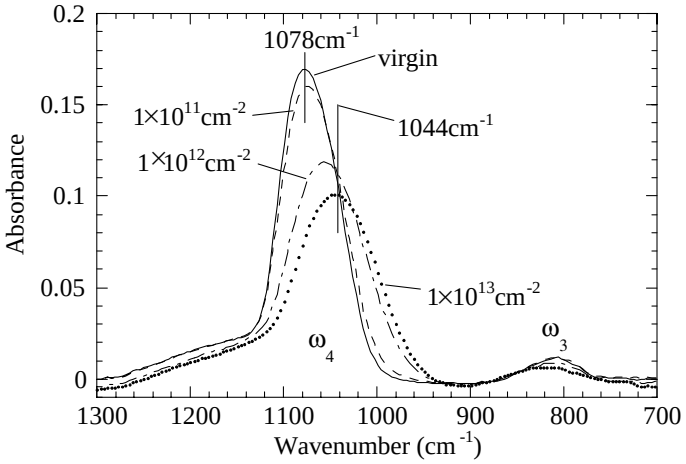

Fig.1 IR absorption spectra of an a- SiO_2 film 193nm thick bombarded with I ions at accumulated doses $1\times10^{11}cm^{-2}$, $1\times10^{12}cm^{-2}$ and $1\times10^{13}cm^{-2}$. Solid line shows the spectrum of the virgin sample.

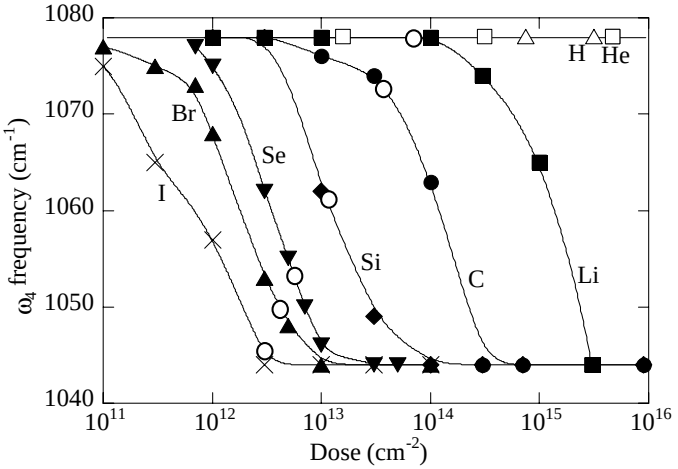

Fig.2 Frequency at an absorption maximum of the ω_4 band against dose. 10MeV H; open squares, 15MeV He; open triangles, 2MeV Li; closed squares, 4MeV C; closed circles, 30MeV Si; closed diamonds, 35MeV Se; closed and reversed triangles, 67MeV Br; closed triangles and 80MeV I; crosses. All lines are guides for the eyes. Open circles correspond to the bond energy of Si-O which was obtained from the electronic stopping power of each ions multiplied by dose.

3. Results

Fig. 1 presents IR absorption spectra of a 193 nm thick a-SiO_2 film before and after bombardment with 80 MeV I ions. The unirradiated film shows two first order features in the IR absorption 1078 cm^{-1} and at 805 cm^{-1}, which were labelled ω_4 and ω_3, respectively. Irradiation introduces a shift in opposite directions: the frequency of ω_4 decreases from 1078 cm^{-1} to 1044cm^{-1} whereas that of ω_3 increases from 807cm^{-1} to 822cm^{-1}.

The evolution of the position of the peak labelled ω_4 for a variety of ions and as a function of ion dose is shown Fig. 2. The following ion/energy combinations are shown: 10 MeV H, 15 MeV He, 2 MeV Li, 4 MeV C, 30 MeV Si, 35 MeV Se, 67 MeV Br and 80 MeV I. Peak shift was not observed for either 10 MeV H ions or 15 MeV He ions in the dose region of 10^{16} cm^{-2} and lower. For all other ions, the frequency ω_4 decreased and saturated at 1044 cm^{-1} with increase of dose. The ion dose where saturation is reached is very different for the different ions, spanning three orders of magnitude. Otherwise, the behaviour of the frequency shift as a function of ion dose is similar for all combinations with only a factor of 12 to 15 between the dose required to initiate a shift and that to saturate it. In order to facilitate comparison of the different ion / energy combinations, points of equal deposited energy have been identified. The open circles on each curve in Fig. 2 correspond to a deposited energy ~3.4×10^{23} eV/cm^3, which amounts to a deposited energy density approximately equal to the total Si-O bonding energy ~3.8 eV in a unit volume of a-SiO_2.[10] MDDZ = $0.65/\{(10^{-7}R_d)^2\pi\}$. Peak shifts of the frequency ω_4 at the MDDZ were estimated from Fig.2.

Fig.3 Diameter of holes introduced by bombardment of 80MeV I ions followed by etching vs shift of the frequency $_4$ at the minimum dose to cover the surface with damaged zones (MDDZ). Chemical signals for elements written near squares identify the bombarding ions. Circles present the relationship between diameter of holes introduced by bombardment of 80MeV I ions followed by etching and shift of the frequency ω_4 at the MDDZ with the annealing temperature as a parameter. Temperatures for each experiment are presented near each point.

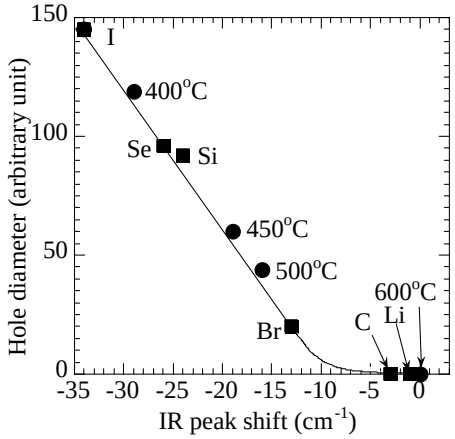

Fig.3 Diameter of holes introduced by bombardment of 80MeV I ions followed by etching vs shift of the frequency ω_4 at the minimum dose to cover the surface with damaged zones (MDDZ). Chemical signals for elements written near squares identify the bombarding ions. Circles present the relationship between diameter of holes introduced by bombardment of 80MeV I ions followed by etching and shift of the frequency ω_4 at the MDDZ with the annealing temperature as a parameter. Temperatures for each experiment are presented near each point.

	Li	C	Si	Se	Br	I
Rd (nm)	1.5	1.9	2.8	2.5	3.4	2.7
MDDZ (10^{12}cm^{-2})	9.8	8.0	6	5.5	2.7	5.1
ω_4 peak shift (cm^{-1})	0	-1	-5	-24	-25	-34
Hole diameter (arbitary unite)	0	0	20	92	96	145

Table 2MeV Li, 4meV C, 30MeV Si, 35MeV Se, 78MeV Br and 78MeV I. R_d value is the radius of a cylinder which absorbs 65% of the incident energy. The minimum dose to cover the surface with damaged zones (MDDZ) was estimated with the formula.

4. Discussion

The data shown in the preceding sections covers the effects of a wide range of ion species, energies, and fluences on the structure of a-SiO_2. To compare one ion mass with another, some scaling of the ion dose would be required. In particular, we would like to compare measurements at a fluence where the individual cylinders are just beginning to overlap. This can be estimated using an analytical formula[11] for the radial profile of the spatial energy deposition. Once this radial damage profile is known, the radius R_d of the damage cylinder is estimated at that which contains 65% of the incident energy. From R_d, the minimum dose to cover the surface with damaged zones (MDDZ) was estimated with the formula,

$$\text{MDDZ (cm}^{-2}) = 0.65/\{(10^{-7}R_d)^2\pi\} \qquad (1).$$

Values for R_d and MDDZ for each of the ions used are summarized in Table, as well as frequencies ω_4 at MDDZ estimated from the corresponding curves in Fig.2. Heavy ions such as Se, Br and I, which upon etching introduce clear individual holes on a-SiO_2, are seen to introduce a large shift of ω_4 at MDDZ. This would imply that even the passage of a single Se, Br or I ion creates a latent track where the shift of the frequency ω_4 is at least -20 cm^{-1}.

Using the data from Table, we now know which doses should be compared and thus re-plotted (as square symbols) the measured diameter of etched holes against the shift of ω_4, for all projectiles but in each case at MDDZ (Fig.3). As well, these data are compared directly with the annealing results of 80 MeV I irradiated samples: the circles show the diameter of holes made by 80 MeV I irradiation, annealing, and etching against the shift of ω_4. Annealing was performed prior to etching and IR absorption measurement. A

maximum shift in ω_4 (at MMDZ) of -34 cm^{-1} could be obtained by bombardment with 5×10^{12} cm^{-2} 80 MeV I ions. An increase of ω_4 and a decrease of the hole diameter are simultaneously observed with increasing annealing temperature. Clearly, the circles (annealing) fall on the same line as the squares (different ion mass) which strongly implies that the shift of ω_4 in the latent tracks is correlated with the etching efficiency of those tracks. Etching efficiency is strongly correlated the the shift of the frequency ω_4.

We will attempt to identify a structural model for the changes in silica induced by swift heavy ions that give rise to the observed shift in ω_4. The basic building block of amorphous silica is the SiO_4 tetrahedron with an O-Si-O bond angle of 109.5°; these rigid tetrahedra are then placed together in 6 to 9 member rings.[12] Molecular orbital calculations indicate that the bond energy is minimized for an inter-tetrahedral, Si-O-Si bridging bond angle θ ~144° and that for $120° \leq \theta \leq 180°$ there is only a weak variation in the bond energy with angle. The central frequency of the IR absorption peak ω_4 depends on the bond angle θ and, as a good approximation, is given by:

$$\omega_4 = a[2(\alpha \sin^2\theta/ 2 + \beta \cos^2\theta/2)/m]^{1/2} \qquad (2)$$

where α and β are the central and non-central force constants, m is the mass of the oxygen atom, and θ is the bridging bond angle of Si-O-Si. If m is in kg, a in N m^{-1}, and with a multiplying constant 5.305×10^{-12}, this equation yields ω_4 in cm^{-1}. A compilation of data on materials where θ has been measured directly by some method such as electron or X-ray diffraction shows that to a very good approximation, for $\theta \leq 150°$, α = 582 N m^{-1} and β = 264 N m^{-1}. Eq. (2) then enables us, with some confidence, to estimate Si-O-Si bond angles from measured IR absorption frequencies. A shift in ω_4 from 1078 cm^{-1} to 1041 cm^{-1} would imply a decrease in Si-O-Si bond angle from 144° to 129°. The Si-O-Si bond angle in a planar three member rings was estimated at 130.5°. [14] Therefore, one candidate to explain such a strong reduction of Si-O-Si bond angle would be the reduction of ring size from six member rings to planar three member rings.

We now recall that the open circles in Fig.2 denote the ion dose where the deposited energy reaches 3.4×10^{23}eV/cm^3, which is approximately equal to the total Si-O bonding energy (3.8eV) in a unit volume of a-SiO_2. The deposited energy was calculated from the electronic stopping power, multiplied by dose. The position of the open circles do not correspond with the starting point of the frequency shift of ω_4. For example, the peak shift started when the absorbed energy exceeded the total Si-O bonding energy for 2MeV Li ions. In contrast, the peak shift was over and saturated when the absorbed energy reached to the total Si-O bonding energy for 80MeV I ions. This suggests that the peak shift is not related to the scission of Si-O bonds. Details were reported in references 15 and 16.

5. Summary

In summary, the defect structure of ion tracks in a-SiO_2 created by swift heavy ions has been studied by IR absorption, XPS and ESR. These techniques showed how the ring statistics and the number of bond scissions changed with ion dose, and that these two phenomena behaved differently. The ion dose dependence of the etching rate enhancement correlated with the changes in ring statistics but not with bond scission or oxygen deficiency. It is concluded, therefore, that the major reason for the fast etch rate in the latent track is the generation of planar three- and four-member rings. These planar three- and four-member rings are likely introduced by a process of flash heating and quenching following the passage of a swift heavy ion.

References

[1] G. Bonfiglioli, A. Ferro and A. Monjoni, J. Appl. Phys., 32, 2499 (1961).
[2] Meftah, F. Brisard, J.M.Costantini, E. Dooryhee, M.Hage-Ali, M.Hervieu, J.P. Stoquert, F. Studer and M. Toulemonde, Phys. Rev. B 49, 12457 (1994).
[3] M. Toulemonde, J.M. Costantini, Ch. Dufour, A. Meftah, E. Paumier and F. Studer, Nucl. Inst. and Meth. In Phys. Res., B 116, 37 (1996).
[4] R.L. Fleischer, MRS Bulletin, 20, 17 (1995).
[5] R.L. Fleischer, P.B. Price and R.M. Walker , Nuclear tracks in solids – principles & applications, University of California Press, Berkley,1975)
[6] E. Dartyge and P. Sigmund, Phys. Rev. B32, 5429 (1985).
[7] K. Tanimura and N. Itho, Phys. Rev. B 46, 14 362 (1992).
[8] G.W. Arnold, J. Non-Cryst. Solids, 179, 288, (1994).

[9] J.B. Bates, R.W. Hendricks and L.B. Shaffer, J. Chem. Phys., 61, 4163 (1974).
[10] A. Hiraiwa, H. Usui and K. Yagi, Appl. Phys. Lett., 54, 1106 (1989).
[11] M.P.R. Waligorski, R.N. Hamm and R. Katz, Nucl. Tracks Radiat. Meas., 11, 309 (1986).
[12] C.E. Jesurum, V. Pulim and L.W. Hobbs, Nucl. Inst. and Meth. In Phys. Res., B 141, 25 (1998).
[13] P.N. Sen and M.F. Thorpe, Phys. Rev. B15, 4030 (1977).
[14] F.L. Galeener, Solid Stat. Commun., 44, 1037 (1982).
[15] K.Awazu, S.Ishii, K.Shima, S.Roorda, J.L.Brebner, Phys.Rev. B, 62, 3689 (2000).
[16] K.Awazu, S.Ishii, K.Shima, Jpn. J. Appl. Phys., 39, 7058 (2000).

3.4 Foil thickness for ions attaining charge equilibrium

K.Shima

Energetic ions after penetration in matter change their charge fractions until projectile charge states become equilibrated at certain penetration depth. This charge equilibrium thickness, T_{eq}, is very important in various fields where ion beam interaction is involved. Actually, in most cases, there has been no way to estimate the T_{eq} values. One reason for this is because non-equilibrium charge distribution data are much less than equilibrium charge distribution data, and hence the systematic trend of T_{eq} on projectile atomic number Z_1, target atomic number Z_2, and ion energy E is little known. Particularly, the dependence of T_{eq} on Z_2 in solid targets has little been investigated except for a few combination of Z_1+Z_2 [1]. On the other hand, theoretical study of T_{eq} from the view of collision process is also limited [2] since many parameters involved in charge exchange process make the investigation complicated.

In order to serve as a milestone for the systematic understanding of T_{eq} in matter, the dependence of T_{eq} on Z_2 has been investigated for the incidence of 95 MeV F ions passing through the solid target foils of C, Al, Cu, Ag and Au. The reason to have adopted such swift F ions as projectiles is that the dominant charge states involved in the collision are limited to F^{9+} and F^{8+}, and hence, charge exchange process is rather simplified. For this purpose, charge distribution of F ions was measured at the foil thickness region where projectile charge states vary from non-equilibrium to equilibrium.

Obtained mean charges, q_b , of ions after passage through foils are plotted in Fig.1as a function of target thickness x. A noticeable result is that the charge equilibrium thickness T_{eq} is strongly dependent on Z_2 , i.e., the T_{eq} values are higher for ions passing through a foil with lower Z_2. When the target thickness is expressed in units of atoms/cm^2, the T_{eq} value of 95 MeV F ions in C foil is about one order higher than that of F ions in Au.

From observed data of charge fractions of ions as a function of foil thickness, charge exchange cross sections have been estimated by means of two different ways of curve fitting method and slope method. The σ_{qk} values deduced from slope method are charge exchange cross sections in single collision at very small penetration depth, meanwhile those from curve fitting method are cross sections of ions from

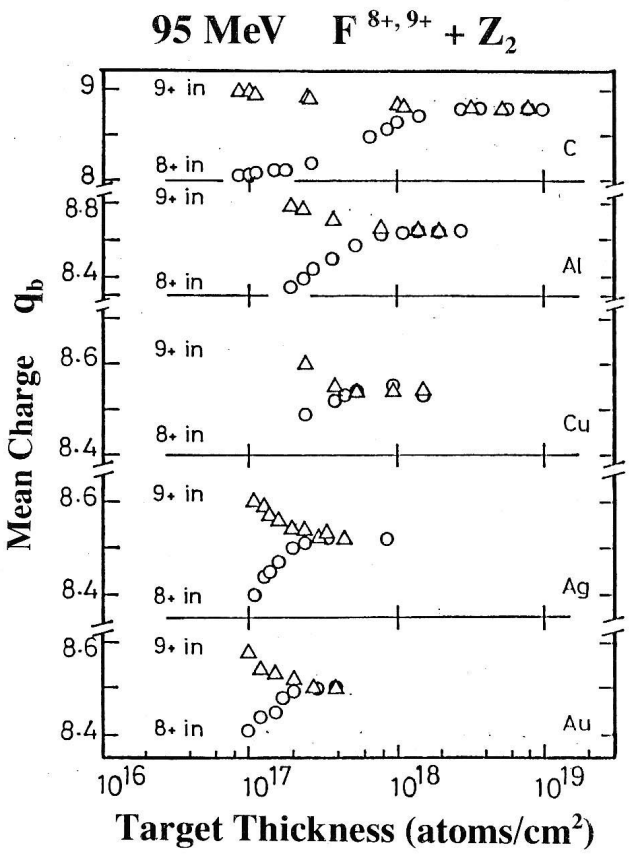

Fig.1. Observed values of mean charges, q_b , of 95 MeV F ions after passage through C, Al, Cu, Ag and Au foils as a function of foil thickness in units of atoms/cm^2.

charge non-equilibrium to equilibrium penetration region. The fact that the σ_{qk} values of these two methods are in good agreement, suggests that the ionic charge exchange process in carbon foil is dominated with step-by-step single electron transfer where the excited state of ions during the collision is of minor contribution. In other word, the collision process of highly charged 95 MeV F ion in carbon is rather simple, and the effect of residual excitation collision may be of minor contribution to charge exchange process. The reason is as follows.

In the analysis of charge exchange of 9.6 to 38 MeV F ions in carbon foils, Nielsen et al. adopted 3-component model in which the probability of ions bearing L-shell electrons was taken into account for each component of projectile double-, single- and no-K-vacancy states. One of the solutions they obtained was that the mean numbers of L-shell electrons attached to an ion of single-K-vacancy state are 1.55 for 9.5 MeV F ions and 0.28 for 38 MeV F ions inside the carbon foil. Since these numbers should rapidly tend to decrease with increasing collision energy, 95 MeV F ions inside the carbon foil may be considered to be mostly in the ground state.

In the present collisions, charge states of F^{9+} and F^{8+} are mainly correlated with the charge exchange process, and so, equilibrium mean charges are around 8.5 (see Fig.1). For simplicity, if we assume that the collision is dominated by F^{9+} and F^{8+} ions, then, the solution of rate equation is given by,

$$F_9(x) = (\sigma_{89}/\sigma_T)\{1-\exp(-\sigma_T x)\}, \quad (1)$$

$$F_8(x) = 1 - F_9(x), \quad (2)$$

$$\sigma_T = \sigma_{89} + \sigma_{98}, \quad (3)$$

for the incidence of F^{8+} at $x=0$. Generally, the total cross section σ_T is higher for higher Z_2. On the other hand, charge equilibrium thickness T_{eq} is subject to the variation of the function $\exp(-\sigma_T x)$. Hence, T_{eq} values are smaller for the higher Z_2. In fact, if we list the σ_{89}, σ_{98} T_{eq} and $\sigma_T T_{eq}$ values of observed at present in table 1, the $\sigma_T T_{eq}$ values are almost indifferent to Z_2.

Above mentioned fact indicates that in a very simple collision where only two charge states are involved in charge changing process, the magnitude of the sum of electron loss and electron capture cross sections determines the magnitude of charge equilibrium depth T_{eq}.

For ions whose degree of charge states, q_b/Z_1, is not so high as that of 95 MeV F ions, the number of charge states mainly involved in charge exchange process would be more than two. In that case, the solution of the rate equation becomes a little complicated function of charge exchange cross sections. However, on the analogy of 95 MeV F+Z_2 collisions, we can easily estimate that, the T_{eq} values of ions in matter would be dominated with the charge exchange cross sections of ions around the mean charge states in matter. In order to be able to predict reliable values of T_{eq} for any given collisions of Z_1+Z_2, more accurate cross sections as well as experimental data compilation are necessary.

Experimental reports on the Z_2-dependence of T_{eq} are much less compared with reports on T_{eq} of Z_1 + C foil collision. As is clear from above description, this is because, equilibrium thickness T_{eq} of ions in C foil is larger than that in other foils with higher Z_2, and hence, the observation of the former collision is easier. In this work, by using thin self-supporting foils of Z_2=6 to 79, the T_{eq} values have first been obtained over the wide range of Z_2.

Table 1. Charge exchange cross sections σ_{89} and σ_{98}, charge equilibrium thickness T_{eq}, and the product $\sigma_T T_{eq} = (\sigma_{89} + \sigma_{98}) T_{eq}$ for 95 MeV F ions colliding with foils of C, Al, Cu, Ag and Au.

foil	σ_{89} (10^{-18} cm^2)	σ_{98} (10^{-18} cm^2)	T_{eq} (10^{18}atoms/cm^2)	$\sigma_T T_{eq}$
C	0.7±0.15	0.4±0.1	3.0±0.5	3.3
Al	2.8±0.3	1.5±0.3	1.0±0.2	4.3
Cu	6.0±0.8	3.5±0.4	0.50±0.2	4.7
Ag	8.0±1.4	6.0±1.1	0.30±0.08	4.2
Au	10±1.8	8.0±1.9	0.24±0.06	4.3

References

[1] C.S.Sofield, N.E.B.Cowern, J.Draper, L.Bridwell, J.M.Freeman, C.J.Woods and M.Spencer-Harper, Nucl. Instrum. Meth. 170, 257 (1980).

[2] V.P.Zaikov, E.A.Kral'kina, N.F.Vorobjev, I.S.Dmitriev, V.S.Nikolaev and Ya.A.Teplova, Nucl. Instrum. Meth. B5, 10 (1984).

3.5 Difference of the diffusion and trapping of the implanted deuterons in metals between the single crystal and poly-crystal

N. Kawachi, T. Katabuchi, M. Yamaguchi, M. Imon, and Y. Tagishi

We have proposed the method to measure the density of the implanted deuterons in solid materials during the deuteron implantation [1,2]. In this method, the density of the implanted deuterons is measured by detecting the emitted protons from the nuclear reaction $^{2}H(d,p)^{3}H$ between the implanted deuterons and the incident deuteron beam. In the present work, the D^- ion beam with an energy of 90 keV was used as an implanted beam and at the same time as a probe beam. The temperature of the target materials was kept constantly during the implantation, by using a thermoelectric cooler. The emitted protons from the nuclear reaction $^{2}H(d,p)^{3}H$ were detected with a silicon solid-state detector. We measured the time-dependence of the yield of the emitted protons as a function of time from the beginning of the bombardment. The time-dependence of the proton yield reflects diffusion and trapping of the implanted deuterons in the target materials.

Experimental results were obtained for various metal targets (Al, Ti, Ni, Cu, Pd, Ta, Pt and Au) at various temperatures. A drastic difference of the time-dependence of the proton yield was observed between the single crystal and poly-crystal of Ta. On the other hand, no difference was observed in case of those in Cu (Fig. 1). Further, the depth profiles of the implanted deuterons are able to be obtained from the energy spectrum of the emitted protons by using the kinematics of the $^{2}H(d,p)^{3}H$ reaction. Further systematic studies are now in progress.

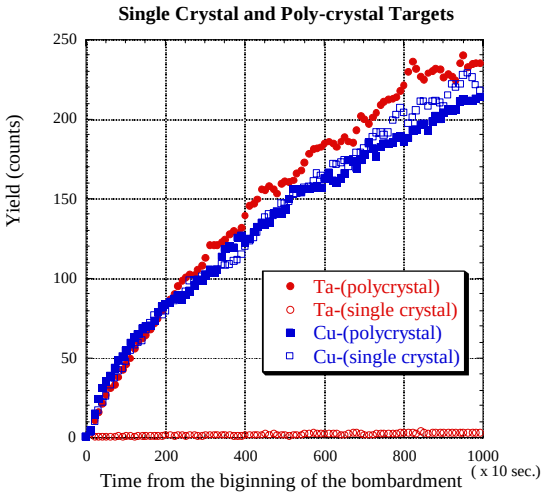

Fig.1. Proton yield from the $^{2}H(d,p)^{3}H$ reactions during implantation of D^- ions in Ta and Cu (single crystal and poly-crystal) at room temperature.
Beam energy: 90keV
Intensity: 500nA
Diameter: 3mm

References

[1] N. Kawachi et al. UTTAC annual report **66**(1997)62

[2] N. Kawachi et al. UTTAC annual report **67**(1998)95

3.6 Formation of transition metal cluster silicides on gas phase reactions

A.Negishi, N.Kariya, K.Sugawara†, I.Arai and S.M.Lee

The study of the clusters composed of metal and silicon atoms has been carried out so far in some way using the laser ablation method [1]. Unfortunately the clusters including more than two metal atoms were rarely found in such a way. The results were explained owing to the fact that the binding energy between two Si atoms is higher than that between Si and metal atoms. In our previous studies mainly concerned with the reactivities of cluster cations toward simple molecules in gas-phase, we proposed a method to make stabilized clusters in advance react to silane molecules. The present experiment intends an investigation of the formation processes of clusters including more than two metal atoms and their stabilities using a spectrometry with a high mass-resolving power.

The experimental apparatus mainly consists of an external laser ablation/supersonic jet cluster ion source and an Fourier transform ion cyclotron resonance(FT-ICR) mass spectrometer [2]. Cluster cations were produced by irradiation of Nd:YAG laser(532nm,15mJ/pulse) toward a rotating niobium target. Only the cluster caions of roughly predetermine mass could pass an acceleration/deceleration tube. They were introduced into an FT-ICR chamber in a magnetic field of 3T, and finally trapped there by an electrostatic field of 10V in an FT-ICR cell. The FT-ICR chamber is in a vacuum of about 1.0×10^{-9} Torr. The trapped ions were thermalized by collisions with argon atoms introduced through a pulsed valve. Later on, the ions began to collide and react with $^{28}SiH_4$ molecules. After a certain time duration, reaction products were observed. We have measured mass spectra under changing the time duration($t = 0 - 30$ sec) and the reaction gas pressure of SiH_4 gas($p = 1.0 \times 10^{-8} - 2.0 \times 10^{-6}$ Torr).

Fig.1. shows the obtained mass spectra for $Nb_n^+(n = 1 - 12)$ on several conditions. The reaction was frequently occurred and produced the hybrid clusters $Nb_nSi_mH_l$. Because the observed hydrogen atom number l was only even, the dehydrogenation seems to proceed by releasing an H_2 molecule at a time. There was no detached ion including a fragment of niobium cluster.

$$Nb_n^+ + SiH_4 \longrightarrow Nb_nSiH_2^+ + H_2 \qquad (n = 1, 2) \tag{1}$$

$$Nb_n^+ + SiH_4 \longrightarrow Nb_nSi^+ + 2H_2 \qquad (n = 3 - 9) \tag{2}$$

While, the dehydrogenation takes place continuously through either (1) or (2) process, it can be apparently recognized that the process eventually reaches at saturation. One explanation for this saturation may be that the process can not proceed any more once the niobium clusters have been covered with one monolayer of Si atoms. This is because the binding energy between Si and Nb is higher than that between Si atoms. Assuming that the number of attached Si atoms at the saturation depends on the surfice area of the metal cluster, i.e., a seed, and estimated how many Si atoms can be attached to the surface of niobium cluster cation. As Fig.2. indicates that the dependence of the number of attached Si atoms at the saturation depends on the cluster size in agreement with the above mentioned geometric model.

References

[1] S.M.Beck, J.Chem.Phys., **90**, 6306(1989).

[2] A.B.Vakhtin and K.Sugawara, Chem.Phys.Lett., **299**, 553(1999).

†Nanotechnology Reseach Institute, National Institute of Advanced Industrial Science and Technology,Tsukuba 305-8565,Japan

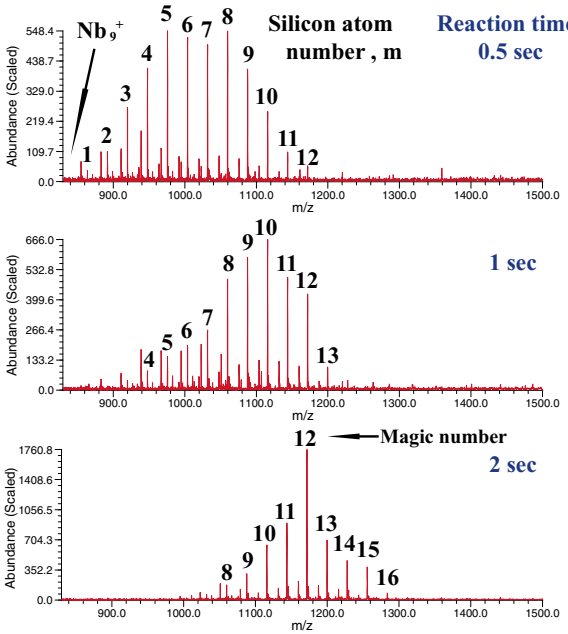

Fig. 1. Mass spectra for $Nb_nSi_mH_l$; observed after the time durations 0.5sec, 1sec, and 2sec, respectively.

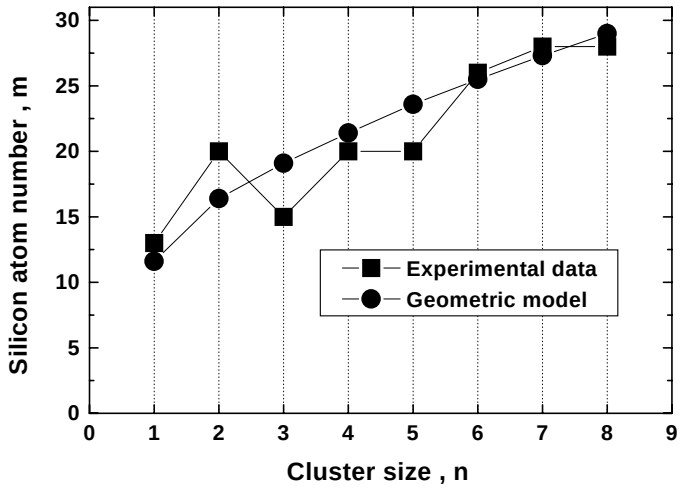

Fig. 2. Number of attached Si atoms; experiment (painted sqaures) and model calculations (painted circles).

3.7 Measurement of large-sized Cu cluster ions by using a quadrupole deflector and a TOF mass spectrometer

H. Sasaki, S. G. Lee, I. Arai and S. M. Lee

During recent years we have developed a metal cluster ion source, some ion optics and a TOF mass spectrometer for investigation of a multi-charged cluster fission[1]. For that purpose, we need to produce large-sized clusters and to observe to the change of their instability in the vicinity of phase transition. As for a Na cluster, the phase transition occurs near the size of 1400. Other metals has similar critical sizes[2]. As a preliminary experiment, we have tried to generate and measure a large-sized metal cluster.

Main features of the experiment are shown in Fig. 1. The metal cluster was generated by a magnetron type sputtering source with an aggregation cell cooled down by liquid nitrogen. The pressure inside the aggregation cell was 1torr filled with a mixture of He and Ar gases while the flow was controlled over the range from 40sccm to 60sccm. The length of aggregation region was also controlled from several cm to 20cm. Both the flow and the aggregation length influenced the distribution of cluster size seriously. We used copper for a target material. The cluster ions were continuously accelerated to -1kV floating tube which contains two electrostatic lenses to transport them efficiently. The DC cluster ion beam was chopped and accelerated toward a ground potential level by an acceleration grid consisting of four electrodes. The electrodes were separated in a length of 2mm from each other and their applied voltages were -1kV, -10V, +655V and 0V, respectively. The ion beam was decelerated between the first electrode and the second one. After passing through the second electrode, the ions were stopped at the point of 0.03mm ahead from the second electrode. Then, we changed the voltage of the second electrode to +1kV rapidly so that the ions were accelerated toward the third electrode as a pulsed bunch. The kinetic energy of the ions became 1keV when they arrived at the fourth electrode. The ions were bent at an angle of 90 degree by the quadrupole deflector in order to separate uninteresting neutral clusters from the bunch. At the exit of the quadrupole deflector, cluster ions enter a 4m long field-free region where their drifts separated themselves in a time domain. The cluster ions were detected by an electron conversion type detector biased up to -8.5kV for a post acceleration effective to detect heavier cluster ions. We measured TOF spectra by using the pulse switch trigger as a start signal and the detector output as a stop signal, both of which were lead to the inputs of a multi-stop time to digital converter(P7886E, FAST ComTec). The range of TOF should be over a few ms in the case of larger clusters. Therefore, we adjusted a frequency of the trigger to 30Hz.

Fig. 2 shows a typical mass spectrum of copper cluster ions. The peaks of $^{40}Ar^{+}$, $^{63}Cu^{+}$, $^{65}Cu^{+}$, Ar_2^{+} and Ar_3^{+} were used for mass calibration. The large-sized Cu clusters with the size n ranging from 2,400 to 24,000, i.e., the mass ranging from 150,000amu to 1,500,000amu were observed. The spectrum had a dip structure around 600,000amu. We can not explain why the observed spectrum splits into two bump structures. The mass distribution could be controlled to a certain extent by adjusting the aggregation length or pressure in the aggregation cell. For example, the mass distribution shifted to the low mass side resulting in the spectrum over the region from 100,000amu to 600,000amu when we decreased the flow of Ar up to 40sccm. In conclusion, by using this cluster source and ion optics, various-sized clusters have become available for the use of multicharged cluster fission experiment.

References

[1] H. Sasaki, S. G. Lee, I. Arai and S. M. Lee, UTTAC annual report 4.9 (1999)

[2] T. P. Martin, T. Bergmann, H. Göhlich and T. Lange, Z. Phys. **D19**, 25(1991).

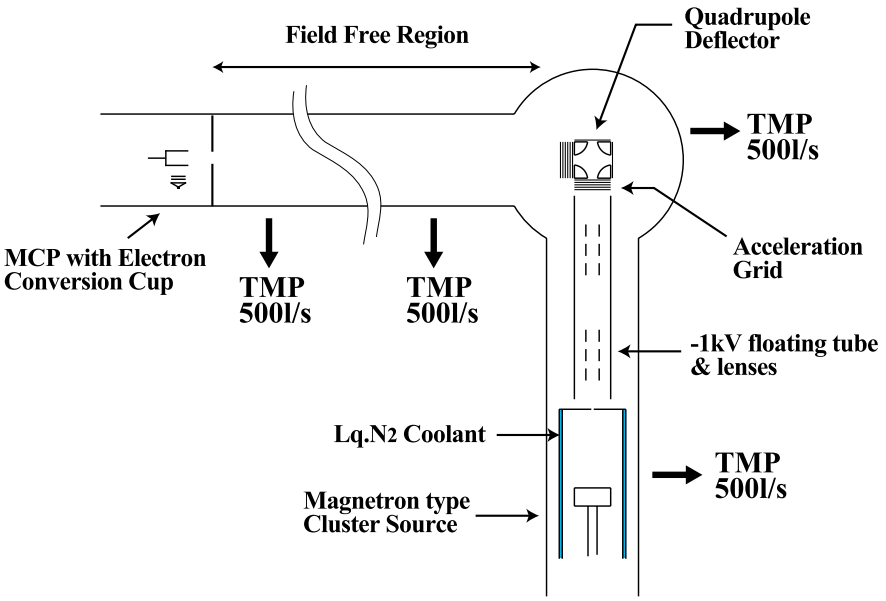

Fig. 1: Schematics of experiment.

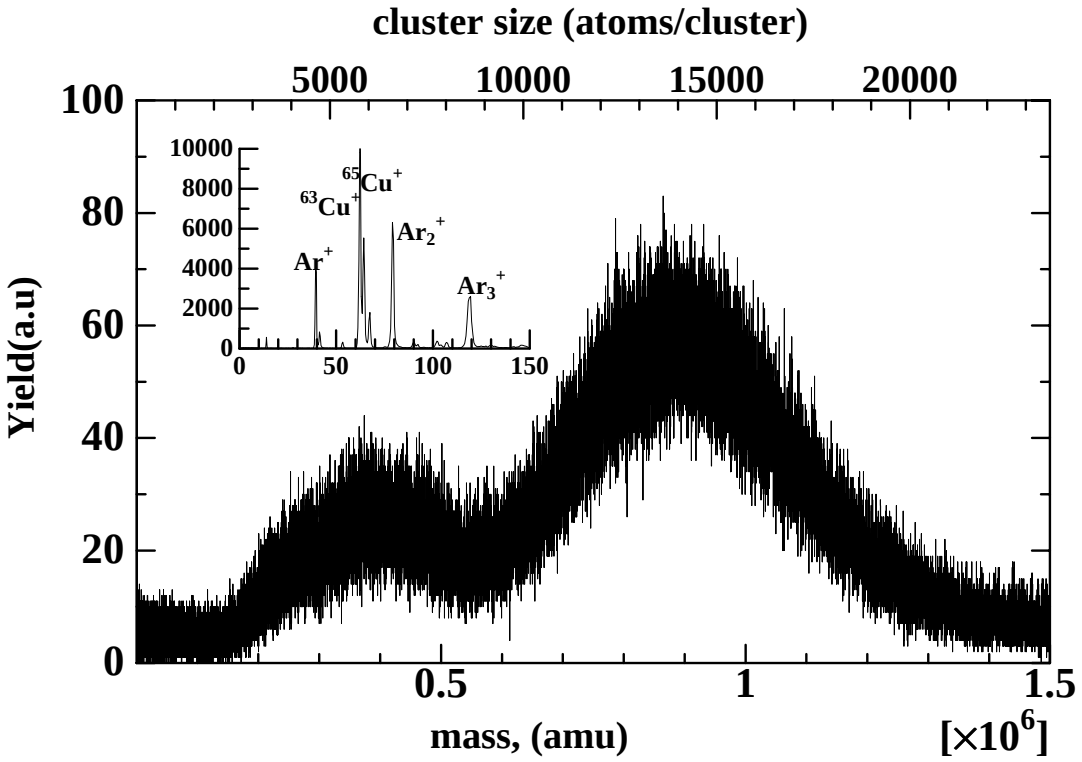

Fig. 2: Mass distribution of $(Cu)_n^+$. The length of aggregation region was 13cm while the amount of the flow of He/Ar gases was 60sccm/60sccm.

3.8 The effect of biased electrode on operation of ECR ion source using liquid He free superconducting solenoid coils

M. Imanaka, T. Kurita, M. Tsukada, T. Nakagawa[1] and S.M. Lee

To produce an intense highly charged ion beam from an electron cyclotron resonance ion source (ECRIS), various methods have been developed. One of those methods is to install a negatively biased electrode on microwave injection side in the source[1]. A beam intensity enhancement with this method is often explained due to an increase of the electron density caused by a reflection of electrons from negatively biased electrode[2-4]. However, little is known about its detailed mechanism.

We have constructed a liquid He free superconducting ECRIS (SHIVA) and successfully extracted various intense beams of heavy ions[5]. For example, the beam intensity of 1.4eμA and 5.7eμA have been achieved for Xe^{35+} and Xe^{32+}, respectively. In SHIVA, the biased electrode method was used and its effectiveness was recognized. We have studied the mechanism of the bean intensity enhancement systematically by observing how the electrode effects on the beam intensity.

For a detailed setup of SHIVA, see the figures in ref. [5]. Fig. 1 shows a schematic diagram of the plasma chamber and the biased electrode in SHIVA. The biased electrode is movable along the beam axis. In the present experiment, we have measured the intensity of highly charged Xe ion beam and the current of biased electrode as a function of both the applied negative bias voltage and the position of electrode. Main experimental parameters are listed in Table 1. In addition, we have observed a time structure of the beam intensity with use of digital storage oscilloscope.

Figs. 2 and 3 show the intensity of measured Xe^{20+} beam and the current of biased electrode according to the changes of bias voltage and electrode position, respectively. In Fig. 2, we can see that both the beam intensity and the current of biased electrode become higher with an increase of bias voltage. It seems reasonable to suppose that this fact supports the above mentioned mechanism providing reflected electrons from the electrode. The current of biased electrode is thought to be a current of the electrons reflected by the electrode into ECR plasma. On the other hand, Fig. 3 shows that the beam intensity changes largely depending on the position of biased electrode, although the current of biased electrode has little dependence. It may be said that the change of bias voltage and the change of the electrode position can act on different dynamics of ECR plasma from each other.

Some of the measurements of time structure for the beam intensity are shown in Fig. 4. In these measurements, we observed that the beam intensity oscillated strongly when the negative bias voltage was applied to the electrode. Fig. 5 shows the measured Xe^{24+} beam intensity and the oscillation frequency as a function of the biased electrode position. Furthermore, we have plotted a correlation chart between the Xe^{24+} beam intensity and the oscillation frequency in Fig. 6. Fig. 6 indicates an apparent positive correlation between them, i.e., that the frequency becomes higher with an increase of the negative bias voltage. It follows that the biased electrode causes a certain instability in the ECR plasma, resulting in the

[1] The Institute of Physics and Chemical Research (RIKEN)

enhancement of beam intensity.

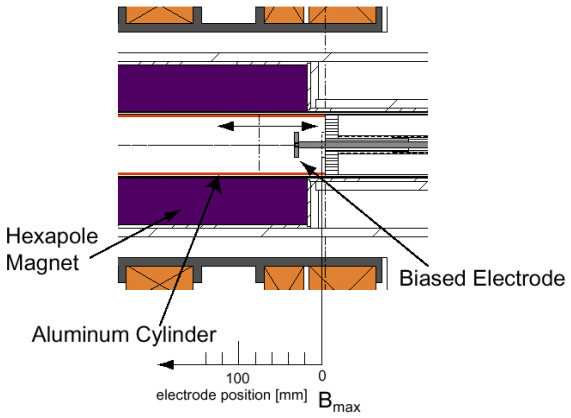

Fig. 1. A plasma chamber and a biased electrode in the sources SHIVA.

Table 1. Main experimental parameters

extraction voltage		15kV
14.5 GHz RF power		565W
axial magnetic field	injection side	1.85T
	central side	0.40T
	extraction side	1.18T
vacuum of injection side		$1.6*10^{-6}$Torr
vacuum of extraction side		$3.3*10^{-7}$Torr

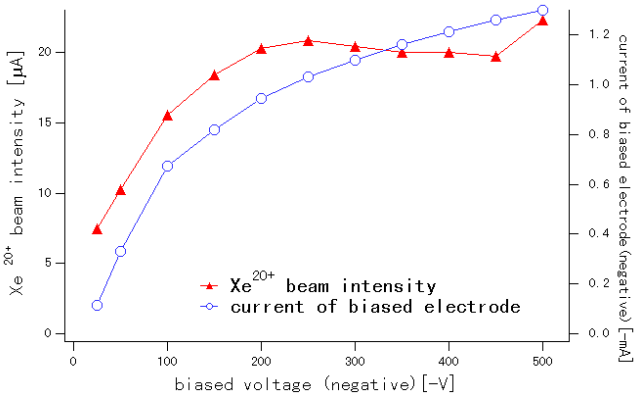

Fig. 2. A Xe^{20+} ion beam intensity and a current of biased electrode as a function of electrode position.

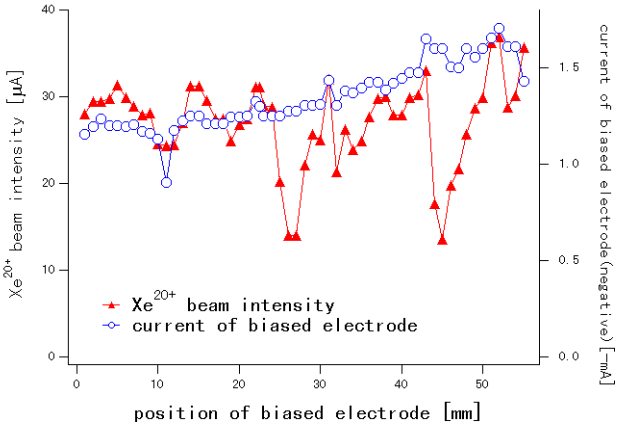

Fig. 3. A Xe^{20+} ion beam intensity and a current of biased electrode as a function of electrode position.

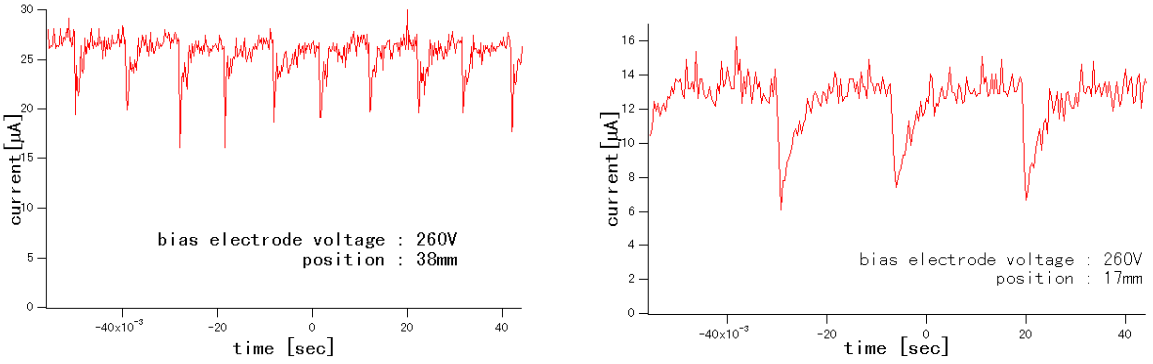

Fig. 4. A time structure of Xe^{24+} beam intensity

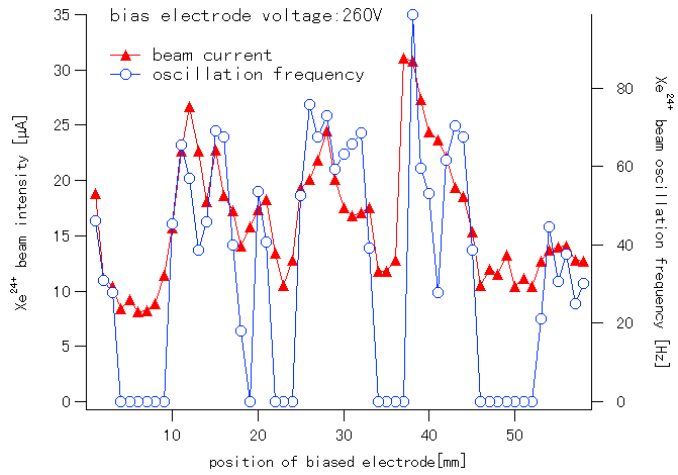

Fig. 5. A Xe^{24+} ion beam intensity and an oscillation frequency as a function of biased position.

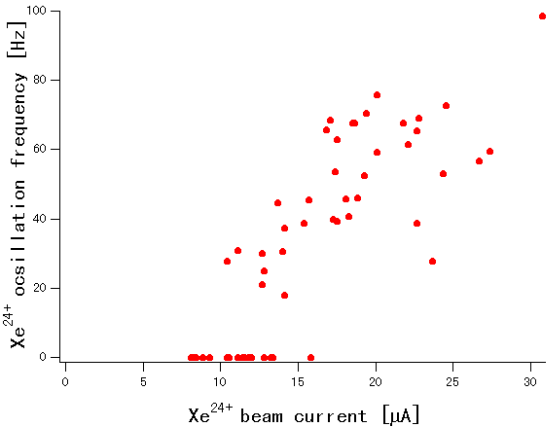

Fig. 6. A correlation between Xe^{24+} beam intensity and oscillation frequency

References

[1] G. Melin et al., Proceedings of the 10th Int. Workshop ECR Ion Sources, Oak Ridge Nat. Lab., Knoxville, 1991, 1.

[2] R. Geller, Electron Cyclotron Resonance Ion Sources and ECR Plasmas, IOP, Bistol (1996).

[3] T. Nakagawa et al., Proceedings of the 14th Int. Workshop ECR Ion Sources, CERN, Switzerland (1999)1.

[4] S. Biri et al., Proceedings of the 14th Int. Workshop ECR Ion Sources, CERN, Switzerland (1999)81.

[5] T. Kurita et al. Rev. Sci. Instrum., 71(2000)909.

3.9 Production of highly charged xenon ions from liquid-helium-free superconducting electron cyclotron resonance ion source (SHIVA)

T.Kurita, M.Imanaka, M.Tsukada, T.Nakagawa[1] , I.Arai and S.M.Lee

In recent years, we are constructing a facility for experiments to study dynamic behaviors of metal clusters like fission, multi-fragmentation. For studying it, we need to produce a highly charged metal cluster through multiple ionization. For that purpose, one of the most effective methods is a soft peripheral collisions of highly charged heavy ions with a metal cluster [1]. In this method, it is crucial to use an intense beam of highly charged heavy ions such as Xe^{32+}. In the last 15 years, the performance of Electron Cyclotron Resonance Ion Sources (ECRISs) have been so intensively improved that they are able to produce intense beam of heavy ions [2]. To produce the intense beam of highly charged heavy ions for the experiment in which the ions collide with metal clusters, we have constructed a superconducting ECRIS called by the name of SHIVA. The source has remarkably unique characteristic that it dose not need liquid helium to obtain the superconductivity of solenoid coils. In this paper, we report the performance of SHIVA for the production of highly charged xenon ions.

Figure 1 shows the cross sectional view of SHIVA. A detail design of the source is described in Ref. [3]. Main characteristics of SHIVA are listed in Table .1. The superconducting solenoid coils are cooled by small Gifford-McMahon type refrigerators below 5 K. It allows to keep the superconductivity of solenoid coils without supplying liquid helium. These solenoid coils are used to supply the mirror magnetic field to confine the plasma in the axial direction. The maximum strength of mirror magnetic field is 3 T at the microwave injection side (B_{inj}) and 2 T at the beam extraction side(B_{ext}). The center coil works in a reversed current mode, which allows to adjust the minimum strength of the mirror magnetic field around the center. The hexapole magnet which consists of 24 segment of permanent magnets is used to confine the plasma in the radial direction. The inner and outer diameters of the hexapole magnet are 80 and 174 mm, respectively. The maximum magnetic field strength at the inner surface of the plasma chamber is 1 T. The inner diameter of the plasma chamber is 72 mm. To protect the hexapole magnet from demagnetization due to a possible increase of operating temperature, the wall of plasma chamber has a double-layered structure to allow a flow of cooling water. The injected microwave frequency is 14.5 GHz. Its maximum power is 2 kW.

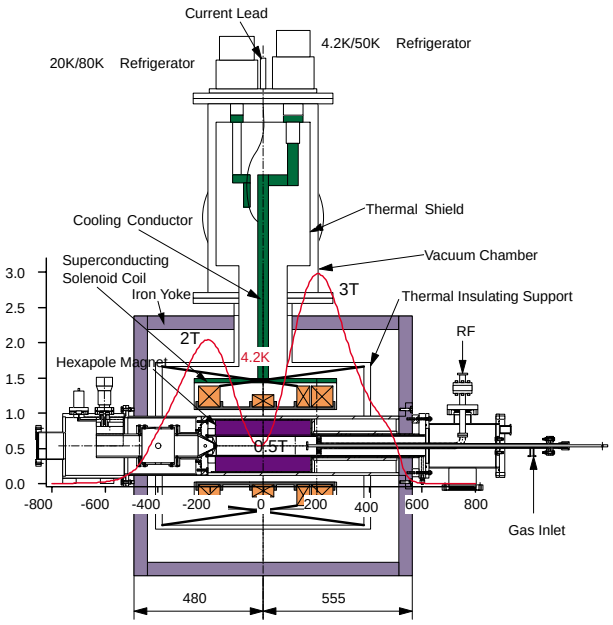

Fig. 1. A schematic of SHIVA

For production of xenon ions, we used an enriched ^{136}Xe gas with enrichment of 85 %. As the gas mixing method is very effective effective to increase the beam intensity for all elements with a mass heavier than a carbon [2], we used natural oxygen gas as the mixing gas. In addition, a negatively biased electrode was placed in the plasma chamber for increasing the beam intensity[2]. The electrode is circular disc of 25 mm in diameter made of stainless steel. The inner surface

[1]The Institute of Physical and Chemical Research (RIKEN)

Table 1. Main characteristics of SHIVA

maximum axial field strength (superconducting coils)	3 T (B_{inj}) - 2 T (B_{ext})
hexapole field strength at surface of plasma chamber (permanent magnets)	1 T
inner diameter of plasma chamber	72.1 mm
length of plasma chamber	375 mm
microwave frequency	14.5 GHz
maximum microwave power	2 kW

of plasma chamber is covered by aluminium of 1 mm thickness. The Al_2O_3 formed on the wall increased the secondary electrons produced under the impact of plasma particles, which may in turn increase the electron density and the source performance [4]. The extracted xenon ions by a potential difference of 15 kV were analyzed by a 90 degree bending magnet, and their charged state distribution was measured with a Faraday cup at the focusing point of the bending magnet.

Figure 2 shows a typical charge state distribution of xenon ions when the ion source is tuned for producing Xe^{32+} ions. The main parameters for producing these ions are also listed in Fig. 2. Under this condition, we have achieved obtained 9.6 μA of Xe^{30+}, 5.7 μA of Xe^{32+} and 0.9 μA of Xe^{36+} with a microwave power of 760 W. A typical configuration of the mirror field is shown in Fig. 3.

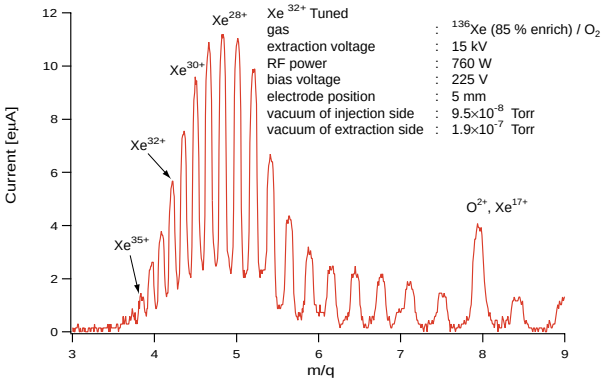

Fig. 2. A charge stage distribution for xenon ions, optimized for Xe^{32+}

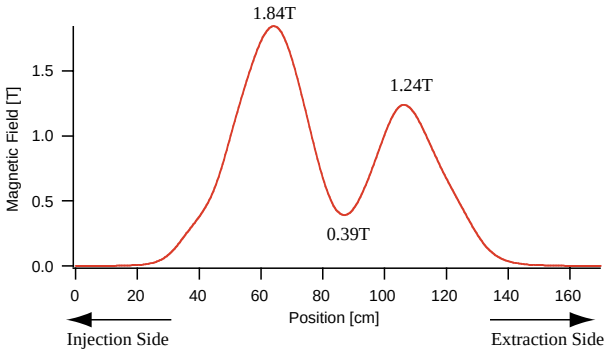

Fig. 3. A typical magnetic field configuration

Figure 4 shows a comparison the beam intensities of highly charged xenon ions among SHIVA and other high performance ECRISs using 14.5 GHz microwaves. SERSE is a superconducting ECRIS of the Laboratorio Nazionale Sud (L.N.S.), Catania [5]. The ion source has a large plasma chamber and superconducting coils which are refrigerated with liquid helium and applied to solenoid coils and a hexapole magnet. Caprice is a compact ECRIS using room-temperature coils, which was developed in CEA, Grenoble [6]. It is clearly seen in Fig. 4 that the beam intensity becomes rel-

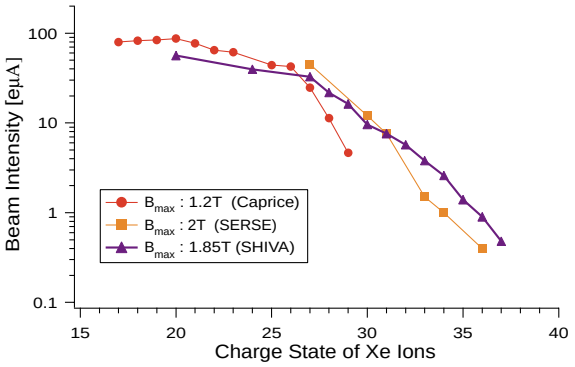

Fig. 4. Comparison of intensities of xenon ions among various ECRISs using 14.5 GHz microwaves

atively enhanced so much in comparison with those of other sources in the region of higher charge state. It means that SHIVA is suitable for producing higher charge state compared to SERSE and Caprice.

The dimensions and other parameters of SHIVA, SERSE and Caprice are listed in Table 2. From Table 2, we consider that following characteristics of SHIVA contributes the high performance of SHIVA.

- A long plasma chamber; A long plasma chamber contribute to a longer ion confinement time [7].
- High magnetic field; A high magnetic field contribute to a longer ion confinement time [7] and a higher plasma density [2].
- An aluminium cylinder in the plasma chamber; The aluminium cylinder may helps to increase the plasma density with secondary electrons emitted from its surface [4]. Also it is experimentally confirmed that aluminium oxide on inner wall of a plasma chamber reduce plasma potential [8] and ion confinement time is extended.

Table 2. Comparison of dimensions and other parameters among various 14.5 GHz ECRISs

	SHIVA	SERSE	Caprice
B_{max} of axial magnetic field	1.85 T	2 T	1.2 T
radial magnetic field	1 T	1.1 T	1.08 T
length of plasma chamber	375 mm	420 mm	160 mm
aluminium cylinder or chamber	yes	no	yes
typical injected RF power	∼800 W	∼1200 W	∼1200 W

To summarize, SHIVA shows a remarkable performance to produce highly charged xenon ions. It has been found that SHIVA is the most suitable for producing a highly charged state compared to other currently working 14.5 GHz ECRISs.

References

[1] F. Chandezon, C. Guet, B. A. Huber, D. Jalabert, M. Maurel, E. Monnandand, C. Ristori, J. C. Rocco, Phys. Rev. Lett. 74 (19) (1995) 3784.

[2] R. Geller, Electron Cyclotron Resonance Ion Sources and ECR Plasmas, IOP, Bristol, 1996.

[3] T. Kurita, T. Nakagawa, T. kawaguchi, S.-M. Lee, Rev. Sci. Intrum. 71 (2) (2000) 909.

[4] T. Nakagawa, Y.Miyazawa, M. Hemmi, T. Chiba, N. Inabe, M. Kase, T. Kageyama, O. Kamigaito, A. Goto, Y.Yano, Jpn. J. Appl. Phys. 35 (7) (1996) 4077.

[5] S. Gammino, G. Ciavola, L. Celona, M. Castro, F. Chines, S. Marletta, Rev. Sci. Intrum. 70 (9) (1999) 3577.

[6] D. Hitz, F. Bourg, M. Delaunay, P. Ludwig, G. Melin, M. Pontonnier, T. K. NGuyen, Rev. Sci. Intrum. 67 (3) (1996) 883.

[7] T. Rognlien, T. Cutler, Nucl. Fusion 20 (8) (1980) 1003.

[8] Z. Q. Xie, C. M. Lyneis, Rev. Sci. Intrum. 65 (9) (1994) 2947.

3.10 Physical process of cluster formation in sputtering of various metals with $6keV\ Xe$ atoms

I. Arai, J. Hirose, H. Sasaki, K. Teranishi and S.-M. Lee

The sputtering, i.e., the particle emission from the surface of bulk material bombarded by an energetic atomic particle, has long been studied. However, most of the published works on the sputtering have focused mainly on the measurement of the total sputtering yield while the study of the phenomenon such as cluster emission remains as one of the least understood field. Even the basic mechanism of the cluster formation has not been established yet [1].

In the earlier stage of study, the cluster formation in the sputtering was perceived as the emission of a whole particle from the bulk surface of bombarded material[2][3]. Subsequently, the statistical agglomeration processes of individual sputtered atoms was perceived as an alternative [4][5]. Later,*first principles* calculations of cluster emission based on molecular dynamics(MD) simulation have been carried out[6]. It was found that the MD simulation in combination with a new many-body potentials among target atoms successfully described the formation of Ag clusters in sputtering of metallic surface. Very recently, a more simplified model inspired by the results of MD simulation was proposed[7]. By considering a metal as a system of harmonic oscillators, the model successfully described the emission of large clusters in sputtering of metals Al, Nb, Ag and Ta with atomic and polyatomic ion bombardments. It was concluded that the larger clusters are emitted as whole agglomerates during the early stages of collision cascade.

It should be noted that a completely different approach to this issue emerged from a related field of research for supported clusters in parallel with the progress of such *first principles* calculations. Recent studies of the cluster formation on bulk surface with a molecular beam epitaxy[8][9][10] have successfully applied the scaling *Ansatz*[11][12] [13] for the analysis and understanding of a fundamental cluster formation mechanism. They have proved the usefulness of a scaling concept and strongly suggest that the application of scaling *Ansatz* should be also useful for the study of cluster formation in the sputtering. Indeed, they have shown an alternative way to describe the cluster formation, i.e., to describe it in terms of *critical phenomena*[14]. It is greatly expected that we can get a new insight on the cluster formation in the sputtering from this new point of view.

As for the experimental observation of cluster formation in the sputtering, a power law nature of cluster abundance spectra has long been discussed in many literatures(see, for instance, [4][15] [16][6]). In the reference [15], it has been remarked that the abundance spectra of Cu, Ag and Au cluster ions produced by the bombardment of Cu, Ag, and Au targets with $10keV\ Xe$ ions [17][18] can be fitted very well with a power law $N(s) \sim s^{-2.7}$ up to the highest mass s of 40. At the same time, it has been also suggested that this observation may be a signature of *critical phenomena* related to the universality classes belonging to fragmentation phenomena which concern a wide diversity of objects in nature.

Very recently, the abundance spectra of fragments produced by high energy nuclear collision has been reproduced remarkably well within a framework of a parameter free percolation model treating a nucleus as a simple fluid and it has been suggested that the percolation could be an universal mechanism to explain the fragmentation of simple fluid[19]. It has been also remarked that experiments with atomic clusters would help to confirm the hypothesis. In this connection, the cluster formation in the sputtering could be considered as a fragmentation of the solid surface bombarded with energetic atoms and a new systematic measurement and a new analysis along the above direction should be done urgently.

In our previous experiment, we measured the abundance spectra for 3d transition metal clusters produced by the bombardment of $6keV\ Xe$ atoms [20]. We successfully applied the scaling *Ansatz* for the cluster abundance spectra in the sputtering of 3-d transition metals for the first time and observed a striking similarity among the scaled spectra. To understand further, we carried

out a model calculation based on a 2-dimensional bond percolation model with the concentration of broken bonds p as an only parameter. The model worked quite well. Furthermore, a strong anti-correlation between the concentration of broken bonds and the thermal conductivity at 976K for each bombarded material was found[21].

In the present experiment, we have examined cluster abundance spectra for various metals with diverse melting temperatures ranging from $500K$ to $4000K$. Our previous experiment has strongly suggested that the physical process of cluster formation in sputtering is closely related to the series of thermal transport phenomena, e.g., the injection of heat by $6keV\ Xe$ atom bombardment, the diffusion of heat around the metal surface, the associated structural changes in the surface, and the resulting cluster emission. We have considered that the melting temperature is a key issue making a serious effect on such structural changes.

We have observed cluster abundance spectra for various metals by bombarding a target material with a $6keV\ Xe$ atom coming from a FAB source(see Figure 1). The cluster cations accelerated by an extraction potential of 10 kV were guided to a high resolution mass analyzer(JEOL $JMS-HX110$) with a mass resolution of $\frac{m}{\Delta m} \sim 5000$ and a mass range up to 5000 amu.

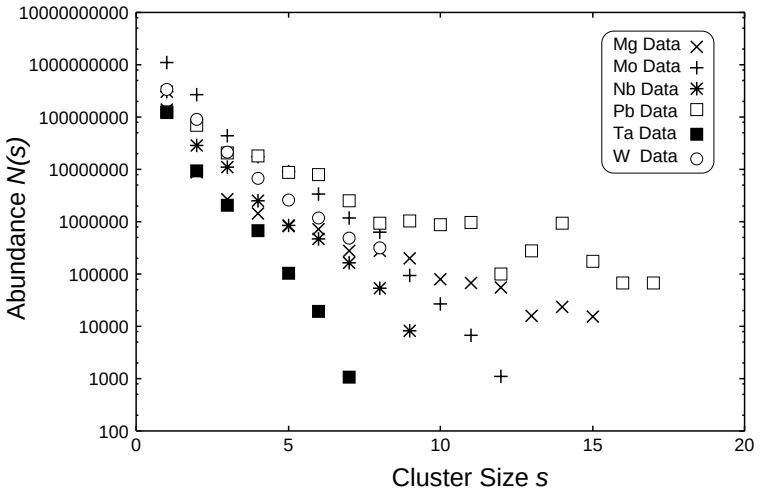

Figure 1: Cluster abundance spectra for various materials

We have applied a scaling *Ansatz*[13] for those spectra. The abundance spectrum $N(s)$ for the cluster size s should be given by a scaling form

$$N(s) \quad = \quad N_0 s^{-\tau} f(s/S), \tag{1}$$

where N_0 is a normalization factor, τ is a critical exponent, $f(s/S)$ is a cutoff function and S is a mean cluster size, i.e., only one characteristic size, defined by

$$S \quad = \quad \frac{\sum_{s=1}^{\infty} s^2 N(s)}{\sum_{s=1}^{\infty} sN(s)}. \tag{2}$$

In the equation (1), the term $s^{-\tau}$ describes a scale-independent part while the term $f(s/S)$ describes a scale-dependent one, i.e., a finite-size effect.

We have made scaling plots for the measured cluster abundance spectra $N(s)$ with a value of 2, i.e., *a superuniversal value*, for τ(see Figure 2). Surprisingly, it is found that all the spectra overlap each other by adjusting their normalization factors. As a result, we have found a remarkable regularity among the measured cluster abundance spectra.

To understand further, we have carried out a calculation based on a percolation theory[22][23]. To keep the situation as simple as possible, it is assumed that the metal surface consists of the

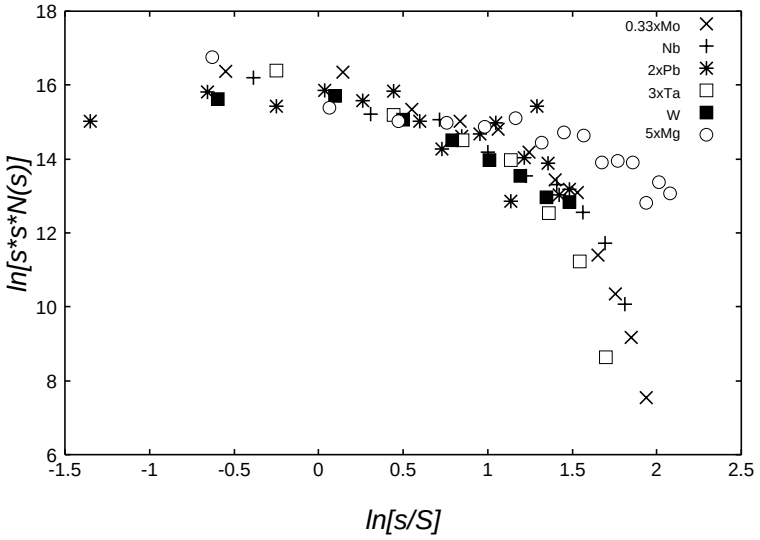

Figure 2: A scaling plot of abundance spectra for various metals

atoms arranged in 2-dimension and connected with each other by a bond and that a cluster is formed when all of its circumferential bonds are broken Here, it should be noted that the concentration of broken bonds p is an only parameter to fit the experimental data.

Each of the measured cluster abundance spectra has been reproduced very well with a suitable value of p(see Figure 3). We assume that the bonds are broken by a thermal excitation so that the value of p for each target material should depend on both the effective bond energy and local temperature of bombarded surface at the stage of cluster formation, which are considered closely related to the melting temperature T_m[24] and thermal conductivity k[25] of a bulk material, respectively. We have examined possible correlations between the concentration of broken bonds p and each of the T_m and k for all target materials. As shown in Figure 4, it is found that the p is strongly correlated with the T_m. As for k, any meaningful correlation has not been observed.

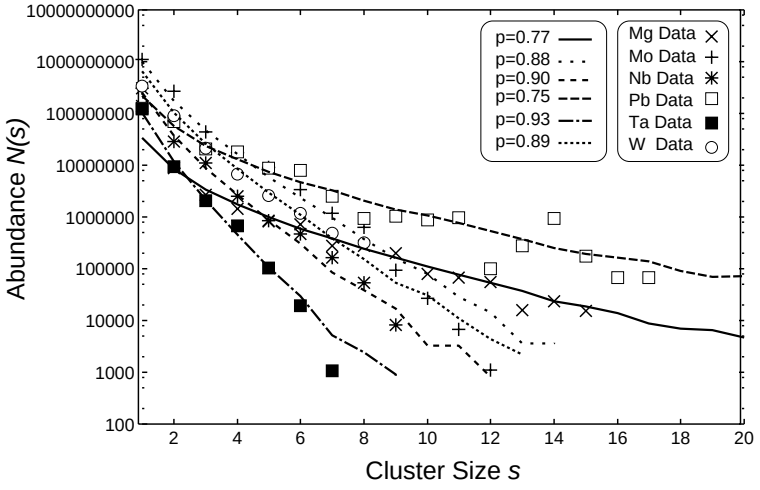

Figure 3: Size distributions of clusters for various metals; calculations based on bond breaking model(lines) and experimental data(symbols)

To understand such a strong correlation, we have considered a substantially new model of the physical process underlying the cluster formation in sputtering. Our idea consists of the

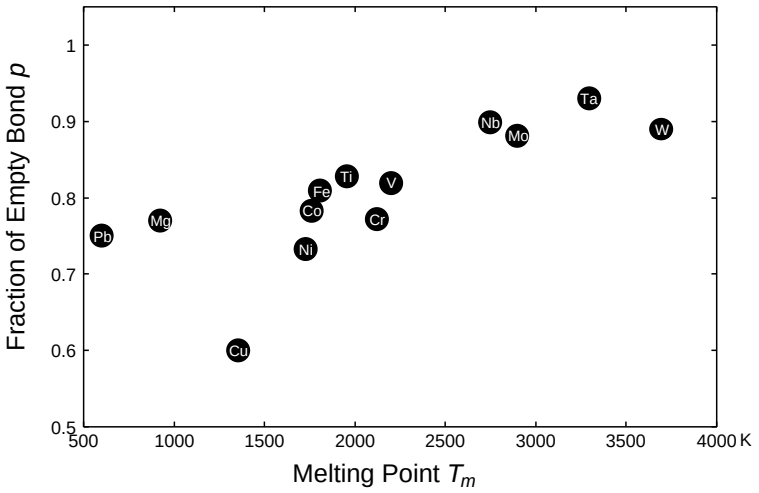

Figure 4: A strong correlation between the melting temperature T_m and the concentration of broken bonds p for various metals;previous experimental results are included

followings;(1)thermal diffusion on the surface, (2)the associated formation of thermally isolated small area, the equilibrium temperature being kept much higher than the melting temperature at around the bombardment position, and (3)cluster formation within the thermally isolated area as a result of bond breaking.

At first, a δ-function like temperature distribution is formed around the bombardment position. Secondly, the thermal energy is transported following the diffusion equation $\frac{\partial T}{\partial t} = \kappa \nabla^2 T$. The diffusion coefficient is given by the formula $\kappa = \frac{k}{C_\rho \rho}$ where C_ρ and ρ are the specific heat and density of target metal, respectively. At a certain time in a course of the thermal diffusion, a mechanical stress take place around the peripheral circular area where the temperature goes down to under the melting temperature T_m for the first time shortly after going up above the T_m. As a result, the inner part bounded by the area becomes thermally isolated due to a structural discontinuity such as a flaw or a crack caused by the stress. Finally, the isolated part is kept in the equilibrium temperature T_{eq}, which is greater than the T_m, and clusters are formed by bond breaking.

At the time t, the temperature distribution $\phi(x, y, t)$ on the surface is given by the equation

$$\phi(x, y, t) = \frac{\phi_0}{2\pi\kappa t} \exp\left(-\frac{x^2 + y^2}{2\kappa t}\right), \tag{3}$$

where ϕ_0 is a normalization constant which depends on the initial condition. The bombardment point is chosen as an origin of the coordinate system. If we assume $\phi(x, y, t) = T_m$, the corresponding radius $r = \sqrt{x^2 + y^2}$ is reduced as

$$r^2 = 2\kappa t \ln\left(\frac{\phi_0}{2\pi\kappa T_m t}\right). \tag{4}$$

Then, the position of discontinuity r_{iso} is evaluated as a maximum of r as follows;

$$r_{iso} = \frac{\phi_0}{\pi e T_m} \tag{5}$$

while the corresponding time t_{iso} is given by

$$t_{iso} = \frac{\phi_0}{2\pi\kappa e T_m}. \tag{6}$$

The inner part surrounded by the discontinuity becomes thermally isolated resulting in the equilibrium temperature

$$\begin{aligned} T_{eq} &= \frac{1}{\pi r_{iso}^2}\int_0^{r_{iso}} \phi(x,y,t_{iso})dxdy \\ &= T_m(e-1). \end{aligned} \tag{7}$$

According to a statistical theory, the concentration of broken bonds p is a function of T_{eq} given by the equation

$$\begin{aligned} p &= P_0 \exp(-\frac{D^*}{4k_B T_{eq}}) \\ &= P_0 \exp(-\frac{D^*}{4sk_B(e-1)T_m}), \end{aligned} \tag{8}$$

where P_0, D^*, and k_B are a normalization factor, an effective dissociation energy of bond, and a Boltzmann constant, respectively. In Figure 5, it is found that the equation (8) is hold well for various metals while Mg and Pb seem not to follow the equation. Here, we assume that P_0 and D^* are constant for simplicity. In the case of Mg and Pb, the dissociation energy D^* is expected to be considerably small compared to the case of other metals because of their small cohesive energies[24]. The smaller D^* gives the larger p.

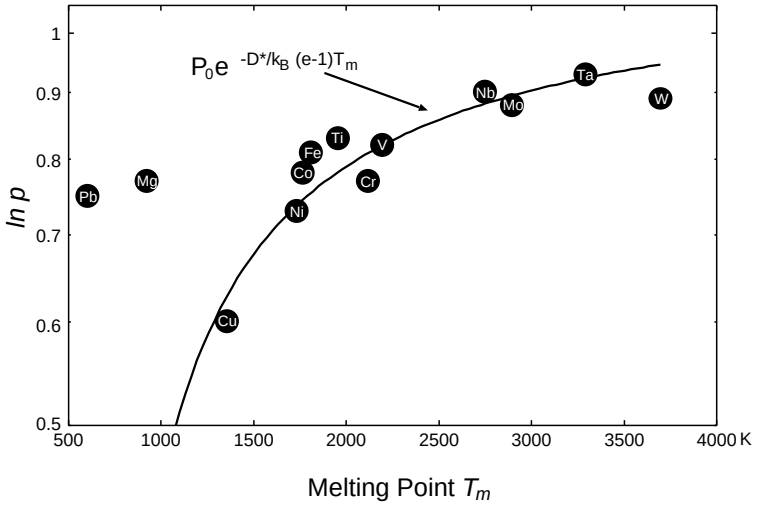

Figure 5: A correlation between the melting temperature T_m and the concentration of broken bonds p for various metals; a model calculation (solid line) and experimental results(symbols)

In summary, we have measured the abundance spectra of clusters for various metals produced by the bombardment of $6keV\ Xe$ atoms. Applying a scaling *Ansatz* for those spectra, we have found that all the spectra coincide with each other. Guided by the observation of this remarkable regularity, a bond breaking model, i.e., a variant of bond percolation model assuming a mechanical break-up of the sputtered surface, has been examined. The model has successfully reproduced all the spectra resulting in an effective value for the concentration of broken bonds p of each material. The p's are strongly correlated with the melting temperatures of bulk materials. To understand such strong correlation, we have proposed a substantially new model of the physical process underlying the cluster formation in sputtering. Our idea consists of the followings; (1)thermal diffusion on the surface, (2)the associated formation of thermally isolated small area, the equilibrium temperature being kept much higher than the melting temperature at around the bombardment position, and (3)cluster formation within the thermally isolated area as a result

of bond breaking. The model has reproduced the effective value for the concentration of broken bonds p of each material very well.

References

[1] W.O. Hofer, in *Sputtering by Particle Bombardment III* eds.:R. Behrisch and K. Wittmaack, Topics in Appl. Phys., 64, Springer-Verlag, Berlin, 1991(chapter2)74.

[2] G. Staudenmaier, Radiat. Eff., 13(1972)87.

[3] W.O. Hofer, Nucl. Instrum. Methods, 170(1980)275.

[4] F. Honda et al., J. Chem. Phys., 69(1978)4931.

[5] R.A. Haring et al., Nucl. Instrum. Methods Phys. Res., B28(1987)205.

[6] A. Wucher et al., J. Chem. Phys., 105(1996)5999.

[7] S.F. Belykh et al., Nucl. Instrum. Methods Phys. Res., B155(1993)409.

[8] M. Zinke-Allmang et al., Phys. Rev. Lett., 68(1992)2358.

[9] J.G. Amar et al., Phys. Rev., B50(1994)8781.

[10] G.S. Bales et al., Phys. Rev., B50(1994)6057.

[11] M.E. Fisher, Rep. Prog. Phys., 30(1967)616.

[12] K. Binder, Ann. Phys. (N.Y.), 98(1976)390.

[13] D. Stauffer, Phys. Rep., 54(1976)1.

[14] H. E. Stanley, Rev. Mod. Phys., 71(1999)S358.

[15] X.Campi, in *The Chemical Physics of Atomic and Molecular Clusters*,Proceedings of International School of Physics $\gg$ *EnricoFermi* $\ll$ (1988:Varenna, Italy), edited by G. Scoles, North-Holland, Amsterdam, Course CVII(1990)231.

[16] M. Wahl et al., Nucl. Instrum. Methods Phys. Res., B94(1994)36.

[17] I. Katakuse et al., Int. J. Mass Spectrom. Ion Processes, 67(1985)229.

[18] I. Katakuse et al., Int. J. Mass Spectrom. Ion Processes, 74(1986)33.

[19] X.Campi et al., Eur. Phys. J., 11(2000)233.

[20] I. Arai et al., Proceedings of 4th CCST Symposium, Sendai, Japan, May 11-12(2000)57.; I. Arai, *Desorption2000* Int. Conf., Saint Malo, France, Sept. 3-7, 2000; I. Arai et al., Transactions of MRS-J 26(2001) to be published.

[21] For a high-purity metal, the k is almost constant above the room temperature[24]. Actually, we need the k at a few thousands K, which is probably similar to the k at 976K, i.e., the available highest temperature in the cited tables. As for Co, we adopted the k at 373K because of the lack of value at 976K.

[22] M.B. Isichenko, Rev. Mod. Phys., 64(1992)961.

[23] D. Stauffer , *Introduction to Percolation Theory*, Taylor and Francis, London, 1994.

[24] C. Kittel, *Introduction to Solid State Physics*, Sixth Edition, John Wiley and Sons, New York(1986).

[25] *CRC Handbook of Chemistry and Physics*, ed. D.R. Lide, 80^{th} Edition, CRC Press, Boca Raton(1999); *American Institute of Physics Handbook*, eds.: B.H. Billings et al., Third Edition, McGraw-Hill Book Company, New York(1972).

3.11 Metal cluster growth in a gas aggregation cell combined with a magnetron sputter

C. K. Chung, H. Sasaki, S. G. Lee, I. Arai and S. M. Lee

In order to elucidate the processes of metal cluster formation and growth, we have constructed a metal cluster source controlled with a magnetron, and a reflective TOF mass spectrometer[1]. A series of mass spectra of the growth of metal clusters from a monomer vapor to several thousands of atoms per cluster for Ti were observed for the first time. As expected, the Ti monomers grew into clusters upon increasing the growth length of the cluster source; the size distribution unexpectedly split into two dominant bands of peaks. One band extended over the range from 1 to 15 atoms par cluster and the other was in the region above 15 atoms per cluster. Moreover, we observed that the position of the boundary between the two bands of peaks was independent of the temperature of the aggregation cell and the vapor pressure of the Ti atoms.

To assess the dependence of the position of the boundary point on the compositions of the clusters, we observed cluster growth for Al and several transition metals: Zn, Zr, Ta and W. All the materials displayed two separated bands of peaks at the initial stages of growth in the same way as Ti did. However, the positions of the boundary between the two bands of peaks are different. Surprisingly, our experimental results deviated enormously from the expectations of classical nucleation theory[2]. Furthermore, at the initial stages of the cluster growth, abrupt decreases of monomer concentration were observed. This suggests that cluster formation via monomer absorption can be restricted within the growth of clusters of several atoms.

Up to now, it has been thought that the cluster formation from a vapor phase involves a stepwise process. The monomer absorption is believed to be dominant among small-sized clusters. And, when the density of clusters becomes high enough for coalescence, it is believed that a coagulation gradually become a dominant process[3]. However, no complete theory exists to explain such a stepwise process. Unfortunately, no experiments have quantitatively elucidated the details of the stepwise process in cluster growth, up to now. However, we have observed experimentally for the first time the transition from successive monomer absorption to cluster coalescence in the cluster growth.

Our experimental results suggest a new model of cluster growth in a gas aggregation source controlled with a magnetron as shown in Fig. 1. Our model, which is a time-limited monomer absorption model based on coalescence, describes the experimental results very well, including the dependence of the position of the boundary between the two bands of peaks observed in the size distribution on the composition of the clusters[Fig.2]. Furthermore, with the interpretation of growth process provided by our model, we found an interesting tendency observed at the initial stages. As shown in Fig. 3, the cluster growth of lighter materials by monomer absorption is stronger than that of heavier ones because the collision frequency between atoms of lighter materials is higher than that of heavier ones. In addition, a material, which has a high cohesive energy, shows a stronger monomer absorption through an increase of the monomer absorption length(W). In general, a heavy material has a high cohesive energy. As the mass number increases, the collision frequency decreases slowly; however, the cohesive energy abruptly increases. Therefore, monomer absorption process should be maintained for a longer time for the cluster growth of heavy materials than for that of light materials. As a result the position of boundary in the mass spectra reflects the competition between the monomer absorption and the coalescence for each material. This is the first attempt to describe metal cluster growth from a monomer to a cluster on the basis of experimental observations.

There remains the problem of how the heat of condensation is evacuated from a cluster. With a high enough vapor pressure for the carrier gas and cooling with liquid nitrogen, it is thought that all of the latent heat can be extracted by collision with the carrier gas. However, this hasn't been quantified yet.

On this point, it must be realized that the heat produced by the coagulation of an i-sized cluster with a j-sized one is enormously less than the heat produced by the condensation of monomers on a j-sized cluster. The clusters can transfer the in internal heat into translational energy [4]. Therefore, after the cluster has attained a certain size, the coagulation can continue under a relatively little production of internal heat. However, it is not known whether the internal heat produced by monomer absorption in a gas aggregation cell is negligible.

In addition, there are problems concerned with the clustering of the carrier gas and the attachment of the carrier gas to the metal clusters. The Ar attachment seems to promote the speed of cluster growth and lower the internal energy of the metal clusters. This effect is dependent on the composition of the clusters. However, little data on effects of gas attachment to metal clusters appears to exist.

Finally, the details of the cluster growth process are very complicated. Various factors, e.g., the temperature, pressure and velocity of the gas and metal vapor, the geometry of the aggregation cell, the diameter of the diaphragm and the available pumping speed, should influence the cluster growth. The fact that they are all interdependent makes an accurate quantitative analysis extremely difficult. We must acquire a better understanding of such interdependency in order to fully explain the cluster growth.

References

[1] C. K. Chung, I. Arai, and S. M. Lee, UTTAC Annual Report 1999, Tandem Accelerator Center, University of Tsukuba.

[2] C. K. Chung, I. Arai, and S. M. Lee, Transactions of the Materials Research of Japan, 25[4] 955-958 (2000).

[3] C. K. Chung, Doctoral thesis, 2001, University of Tsukuba.

[4] J. M. Soler and N. Garcia, Phys. Rev. A, 27, 3300 (1983)

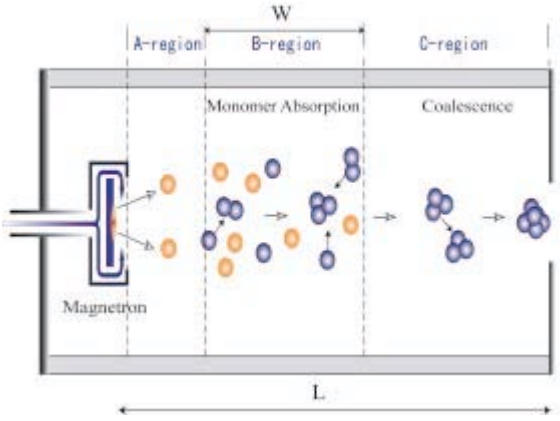

Fig. 1: Model of cluster growth in ourcluster source. L is a total growth length and W a length of monomer absorption region.

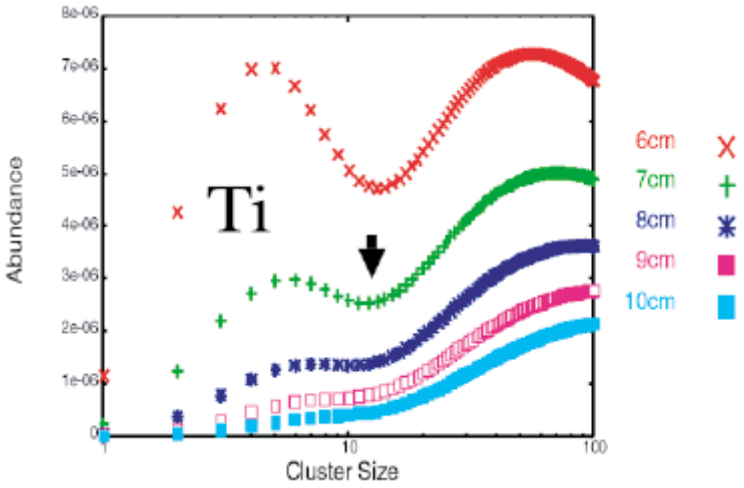

Fig. 2: Size distributions of Ti clusters calculated from the rate equations of our model[4].

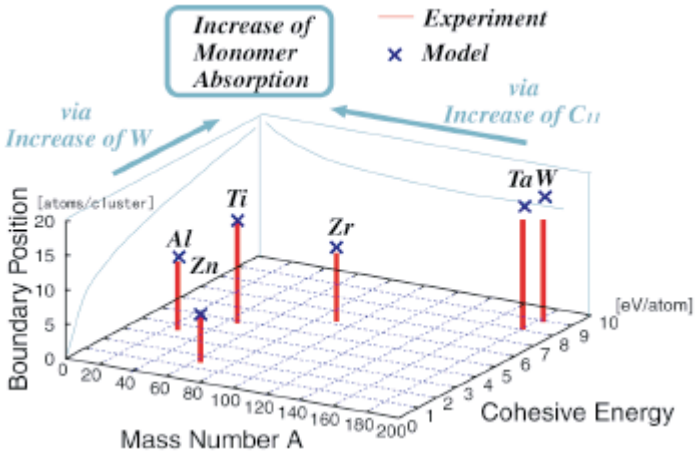

Fig. 3: Comparison of model calculations with experiment. The boundary points of the size distributions are plotted with respect to mass number and cohesive energy for severalmaterials.

3.12 The science of 3d transition-metal oxide system

M. Onoda, N. Nishiguchi, R. Arai, I. Amemiya, K. Kogure, J. Hasegawa, A. Oyadomari, D. Kasuga, K. Kanbe, H. Imai, K. Sekine, A. Tokunaga and T. Banno

The structural and electronic properties of 3d transition-metal oxides and bronzes have been explored by means of x-ray four-circle diffraction and through measurements of magnetic resonance (NMR and EPR), magnetization, and electronic transport, in order to extract peculiar properties in the correlated electron and electron-phonon-coupling systems, low-dimensional spin configurations, and novel materials.

Varian continuous-wave and Bruker pulse NMR spectrometers have been used at the Tandem Accelerator Center. In spite of rather old equipments, these spectrometers have been working by a careful maintanance. However, in order to obtain more detailed results, it is necessary to renovate the equipments.

In 2000-2001, the following investigations have been performed:

- Correlated-electron and electron-phonon-coupling systems
  - Spin-gap state in $M_xV_2O_5$ (M = Ag and Tl)
  - Mixed valence state in $Cu_7V_6O_{19}$
  - Metal-insulator transition in $V_{1-x}Cr_xO_2$
  - Anomalous diamagnetism in $RVO_{3+\delta/2}$ (R = La and Y)
- Quantum spin-fluctuation system
  - Superexchange interaction in MV_3O_7 (M = $Cd_{1-x}Ca_x$ and $Ca_{1-x}Sr_x$)
  - Geometrical frustration in CdV_2O_4
- Lithium secondary battery system
  - Li inserition effect in $M_{1+x}V_3O_8$ (M = Li, Ag and Na)
  - High capacity in $Ag_2V_{4-x}Mo_xO_{11}$

Geometrically frustrated system; CdV_2O_4

The geometrically frustrated system has been investigated for a long time. Here, a state where all pairs of the nearest-neighbour spins are aligned to the opposite direction is not allowed and the spin correlation is suppressed, so that the transition temperature to possible ordered states is reduced significantly. This system sometimes undergoes a structural transition to the lower symmetry, since it brings the profits of the orbital and magnetic energies with resolving the degeneration. The triangular $S = 1$ system $LiVO_2$ is one of such materials, where spin-singlet trimers are formed [1].

The spinel-type Mott insulator MV_2O_4 with nonmagnetic M^{2+} and magnetic V^{3+} also exhibits the frustration effect [2, 3]. Here, M has a tetrahedral coordination (A-site) and V has an octahedral one (B-site). The network of V ions is expressed as the linkage of a regular tetrahedron block that has the V ion at each apex. On the other hand, LiV_2O_4 with average valence of $V^{3.5+}$ is a metal and it has recently been considered as being one of the heavy-fermion system at low temperatures [4]. Moreover, the mechanism of metal-insulator transition in the $Li_xMg_{1-x}V_2O_4$ system has been investigated in detail [5]. In this report, the structural and magnetic properties of CdV_2O_4 are described briefly, revealed through measurements of x-ray diffraction, magnetization and NMR.

The lattice constant of CdV_2O_4 is determined to be $a = 8.688(1)$ Å, which is consistent with the previous report [6]. A part of the x-ray diffraction patterns at 82 and 296 K is shown in Figs.

1(b) and 1(c). The (440) peak at 296 K splits to two peaks at 82 K with the intensity ratio of about 2:1, whereas the (111) peak at 296 K does not change at 82 K. This result indicates that the crystal system at 82 K may be tetragonal with the axial ratio $c/a = 0.990$. The temperature dependence of the lattice constant is shown in Fig. 1(a). In the heated process, the first-order cubic-tetragonal transition appears at $T_{c1} = 97$ K.

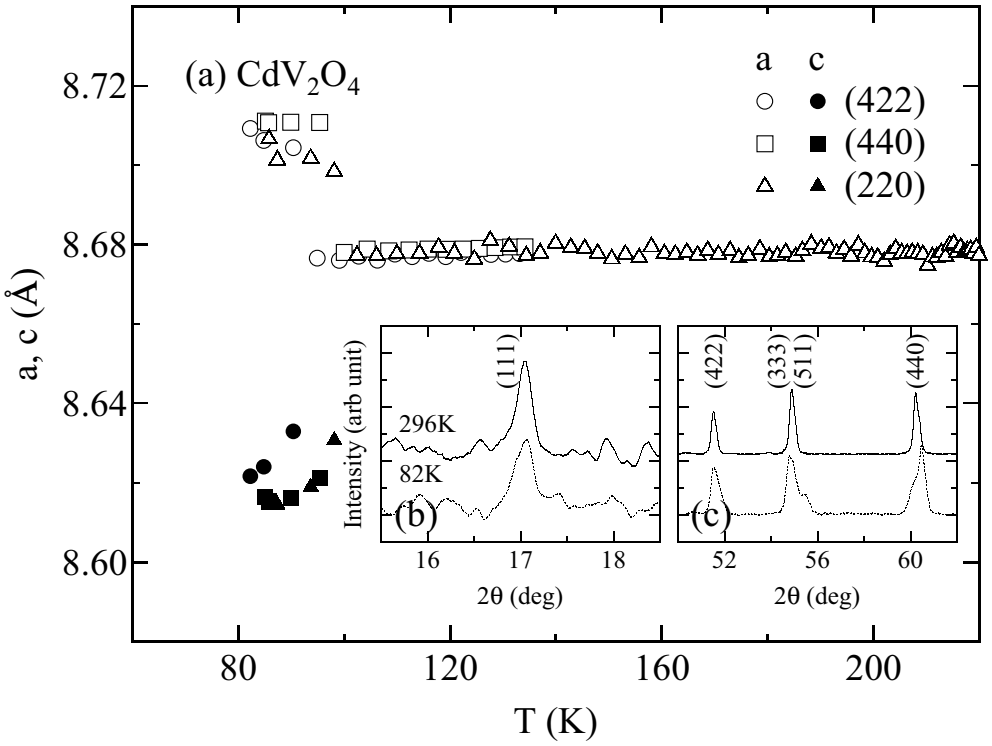

Fig. 1: (a) The temperature dependence of the lattice constants for CdV_2O_4 estimated from the peaks of (422), (440) and (220) reflections; (b) and (c) a part of the x-ray diffraction patterns at 82 and 296 K.

The temperature dependence of the magnetic susceptibility χ for CdV_2O_4 is shown in Fig. 2(a) and the low-temperature part is indicated in Fig. 2(b). A jump of the susceptibility appears at 97 K, corresponding to the cubic-tetragonal transition temperature T_{c1}. At temperatures below T_{c1}, the susceptibility has a maximum at 73 K, and another anomaly with an abrupt change of the temperature-derivative occurs at $T_{c2} = 35$ K. No difference was observed between the susceptibilities for the zero-field-cooled and the field-cooled process at 1 T.

The magnetic susceptibility of the B-sublattice with $S = 1$ is expressed in terms of high-temperature series expansion (HTSE) of up to the 8th-order as follows,

$$\begin{aligned} \chi &= \frac{C}{Jt}(1 - 4/t + 12.33333/t^2 - 32/t^3 + 76.80556/t^4 - 187.4963/t^5 \\ &+ 478.71677/t^6 - 1221.6871/t^7 + 2978.22367/t^8) + \chi_0, \end{aligned} \tag{1}$$

where C is the Curie constant, J is the exchange coupling constant [7], t is the reduced temperature $t = T/J$, and χ_0 is the constant susceptibility. The full curve for CdV_2O_4 in Fig. 2(a) is drawn on the basis of the parameters; $C = 0.98(2)$ emu K $(\text{molV})^{-1}$, $J = 44(1)$ K and $\chi_0 = 1.8(2) \times 10^{-5}$ emu $(\text{molV})^{-1}$. C agrees well with the value calculated from the spin with $S = 1$ and $g = 2$. Comparing the present result with those of MgV_2O_4 and ZnV_2O_4 [2, 3, 5], we conclude that the V-V direct exchange coupling is the most effective in the MV_2O_4 system.

A single resonance line of the ^{51}V-nuclei in CdV_2O_4 was observed, although the intensity was very weak. A plot of the Knight shift K against χ is shown with an implicit parameter T in Fig.

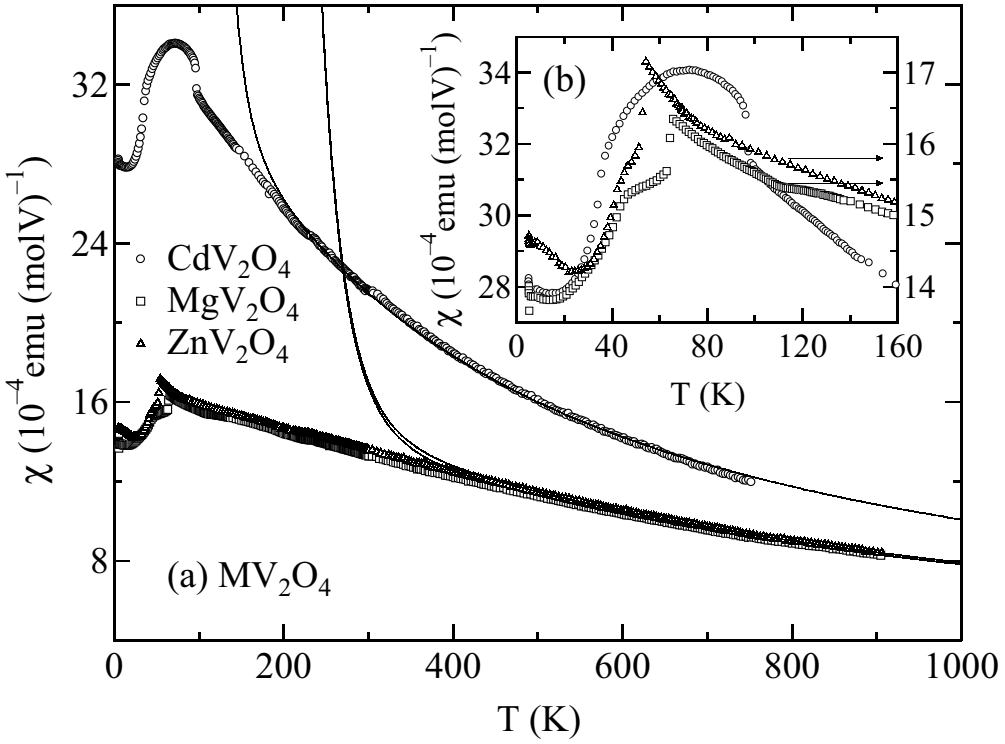

Fig. 2: (a) The temperature dependence of the magnetic susceptibility χ of CdV_2O_4; and (b) the behaviour at low temperatures. The full curve in (a) indicates the result on the basis of HTSE analysis of up to the 8th-order. The results for MgV_2O_4 and ZnV_2O_4 are also presented.

3. The linear relation is seen and the hyperfine coupling constant $H_{\rm hf}^{\rm d}$ is estimated to be –7.1 T $\mu_{\rm B}^{-1}$, which is close to the value for V^{3+} of $LiVO_2$ [1] and is smaller than those of V_2O_3 [8]. The ^{51}V-NMR has not been observed at temperatures below $T_{\rm c1}$. It is not clear whether the signal disappears or becomes weaker.

In summary, the structural and magnetic properties of CdV_2O_4 have been revealed for the first time. The structural transition at 97 K, and the magnetic anomalies at 97 and 36 K exist there. The HTSE analysis of up to the 8th-order indicates that the V-V direct exchange coupling is the most effective in MV_2O_4.

References

[1] M. Onoda M and T. Inabe: J. Phys. Soc. Jpn. **62** (1993) 2216.

[2] H. Mamiya and M. Onoda: Solid State Commun. **95** (1995) 217.

[3] H. Mamiya, M. Onoda, T. Furubayashi, J. Tang and I. Nakatani: J. Appl. Phys. **81** (1997) 5289.

[4] S. Kondo, D. C. Johnston, C. A. Swenson, F. Borsa, A. V. Mahajan, L. L. Miller, T. Gu, A. I. Goldman, M. B. Maple, D. A. Gajewski, E. J. Freeman, N. R. Dilley, R. P. Dickey, J. Merrin, K. Kojima, G. M. Luke, Y. J. Uemura, O. Chmaissem and J. D. Jorgensen: Phys. Rev. Lett. **78** (1997) 3729.

[5] M. Onoda, H. Imai, Y. Amako and H. Nagasawa: Phys. Rev. B **56** (1997) 3760.

[6] B. L. Chamberland and J. F. Wu: J. Electrochem. Soc. (1988) 921.

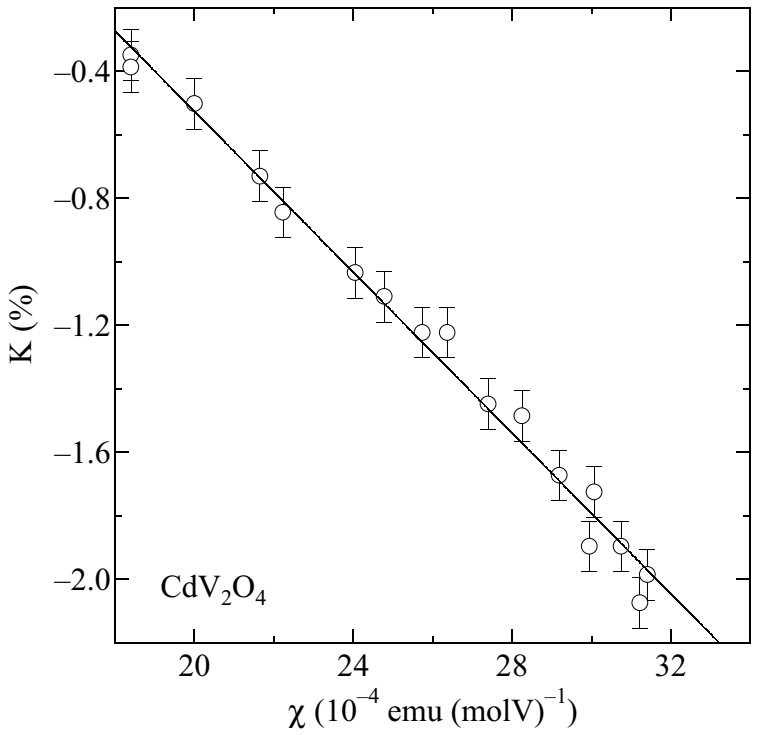

Fig. 3: The $K - \chi$ plot of CdV_2O_4 at temperatures above 100 K.

[7] The Heisenberg Hamiltonian is defined as $H = \sum_{<i,j>} J\boldsymbol{S}_i \cdot \boldsymbol{S}_j$, $\boldsymbol{S}_i$ being the spin operator at site i.

[8] A. L. Kerlin, H. Nagasawa and D. Jerome: Solid State Commun. **13** (1973) 1125.

3.13 Mössbauer study of some granular magnetic materials

F. A. Khan*, K. Ono, M. Nakazumi and E. Kita

Granular magnetic materials have been investigated as a candidate of magneto transport materials such as giant magneto-resistance (GMR) and tunneling magneto-resistance (TMR). They are composed of ferromagnetic fine grains and nonmagnetic matrix of both metals and insulators, and are rather novel magnetic materials compared with traditional materials such as bulk soft magnetic materials or magnetic recording media. These must be categorized into the nano structured material. In this report we examined some ferromagnetic granular systems that include Fe atoms as a magnetic element. Mössbauer study and magnetization measurements of Fe-Cu granular system(metallic granular material) and Fe-CoO(insulating granular system) will be described. The strong magnetic coupling between ferromagnetic Fe atoms and antiferromagnetic CoO can be expected and its magnetic property and electrical conduction are also of interest.

Samples of granular materials were prepared with sputtering. For a metallic system such as Fe-Cu, it is possible to use dc sputtering that makes production rates high when small Fe tablets are placed on the Cu base plates. In order to increase the quantity of Fe in the fabricated samples, we use an Fe metal mask with high coverage area. In this case, the sputtering system was necessary to be switched to the rf-sputtering because of a difficulty in keeping plasma discharge on the ferromagnetic mask by using dc sputtering. The dc power supply had to be replaced by a rf-power source with an impedance box connected with it. The composite target was a circular disc of pure Cu of 5-mm thickness. The Cu disc was covered with the Fe mask which was of same diameter as the Cu disc. For the deposition of Fe-Cu nano-granular films, both thin glass sheets and Kapton films were used as substrates. After ultrasonic cleaning by ethanol, the substrates were dried up by air jet and set on to the target. Several films of Fe-Cu were made on Kapton films and also on the thin glass substrates with different sputtering time and rf-power. Table 1 shows the thickness of three different samples of Fe-Cu thin films produced at three different base pressures and with rf-power constant at 200 watt.

Table 1. Fe-Cu rf-sputtered nano-granular thin films

Sample	Ar pressure (Torr)	Thickness(Å)	Sputtering time (min.)	Fe composition (at %)
#1	5.4×10^{-2}	2450	5	32
#2	7.5×10^{-2}	1680	5	35
#3	1.0×10^{-1}	1550	5	38

The sputtering time was 5 minutes with 5 minutes of pre-sputtering in each case. Composition analysis was carried out with an ICP (Inductively Coupled Plasma photoemission) spectroscopy for Fe-Cu thin

* JSPS short term visiting fellow from Bangladesh University of Engineering and Technology

film. The compositions were ranged between 32 and 35 at % of Fe. The data suggest high repeatability in controlling their composition by using this technique.

Figure 1 shows Mössbauer spectra of Fe-Cu granular thin films in a as-prepared state (a), annealed at 300 °C for l h. (b) and annealed at 400 °C for l h. (c). No significant changes in the Mössbauer spectrum were observed in the annealed sample at 300 °C. The spectrum is composed of a paramagnetic doublet. However remarkable change in the spectrum was observed after annealing at 400 °C for 1 hr. A well defined ferromagnetic sextet was observed in the Mössbauer spectrum (see Fig.1 (c)), indicating the presence of α-iron in the sample. Magnetization measurements were done with a commercial SQUID magnetometer. For the measurements of magnetization the samples were cut into 5 x 5 mm^2 pieces. Field cooled and zero-field cooled measurements were done on the sample. The magnetization curve shows a typical Langevin function indicating that the magnetization process is mainly dominated by large scale particles. The magnetization shows an gradual increase with the decrease of temperature and has a broadened peak around 20 K, suggesting the presence of the super-paramagnetic blocking. This would however have to be confirmed by relaxation measurements. No relaxation measurements have been done on the samples.

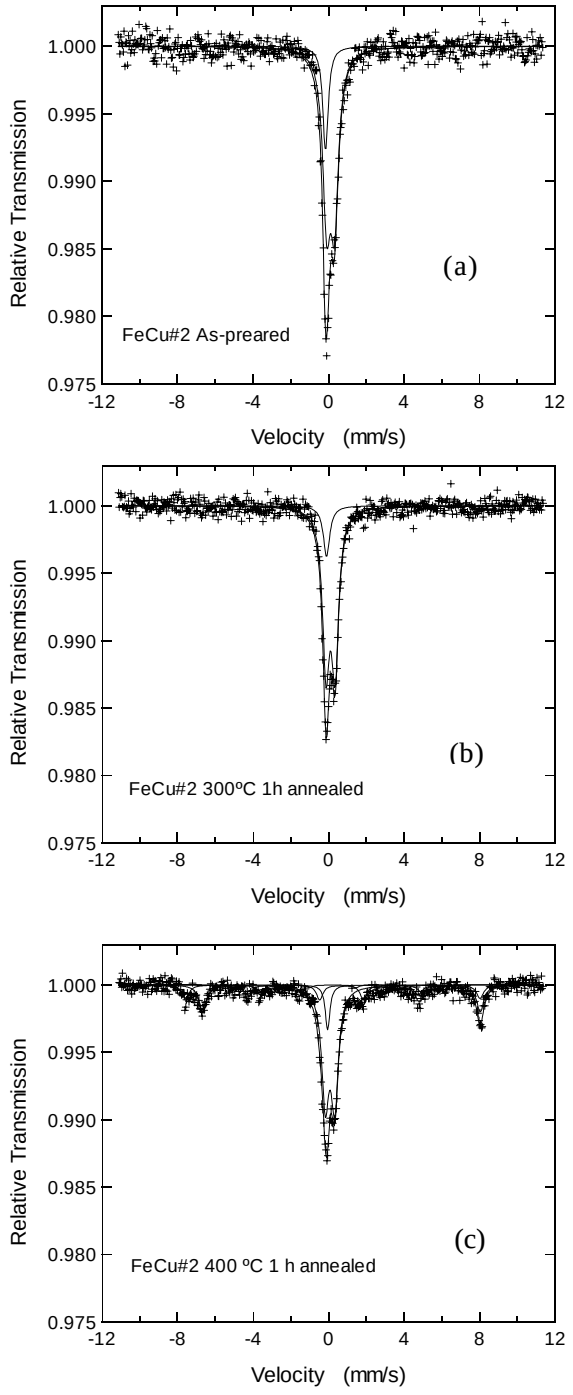

Fig. 1. Mossbauer spectra of an FeCu granular thin film(sample#2), (a) as-grown, (b) annealed at 300 °C for 1 h and (c) annealed at 400°C for 1 h.

For the fabrication of Fe-CoO granular thin films, Fe-CoO composite target was used. As CoO is very fragile it is convenient to use the iron mask instead of iron screw tablets. Similar deposition conditions to Fe-Cu cases were used to fabricate the samples. Figure 2 shows the Mössbauer spectrum of an as-deposited Fe-CoO sample. The sputtering time for this sample was 30 minutes. Figure 3 shows the Mössbauer spectrum of the same sample after annealing at 400 °C for 1 h. From the result for the as-prepared sample, Fe

atoms in the film were not in a ferromagnetic state, but in a paramagnetic state. This means that Fe atoms form small grains in a superparamagnetic state or form compounds with lower magnetic transition temperature than room temperature. The field cooled magnetization measurements were carried out at an applied magnetic field of 3 T at 5K. The curve shows a shifted hysteresis with different values of remanent magnetization and cohesive fields. Such asymmetry may have originated in the exchange anisotropy of the sample due to the magnetic coupling between ferromagnetic Fe and antiferromagnetic CoO layers.

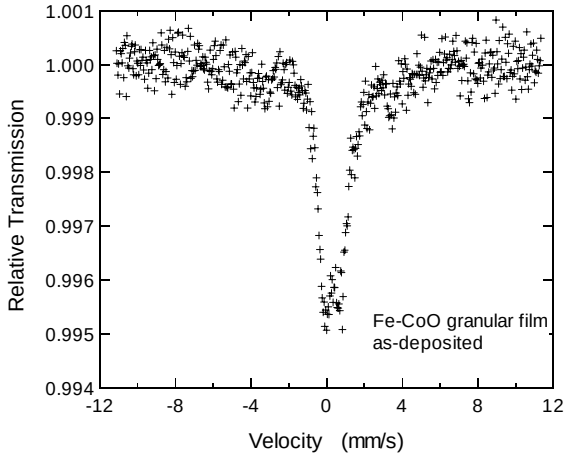

Fig.2. Mössbauer spectrum of an as-prepared Fe-CoO. granular thin film.

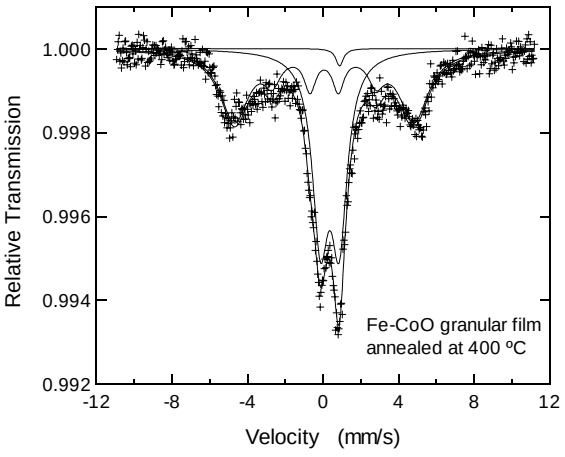

Fig.3. Mössbauer spectrum of an Fe-CoO. granular thin film annealed at 400 °C for 1 h.

Further magnetization measurements and low temperature Mössbauer studies are necessary in order to make the magnetic property more clear.

4.1 Quantitative trace element analyses of single fluid inclusions in hydrothermal quartz by PIXE

M. Kurosawa, S. Shimano, T. Kato, K. Shima and S. Ishii

Fluid inclusions in hydrothermal veins are important as the most convincing information of fluid activities and vein-type ore formation. In particular, elemental compositions of fluid inclusions provide a direct evidence for chemistry of hydrothermal fluids and ore-forming processes. Thus considerable efforts have been invested in the development of techniques for the precise quantitative elemental analyses [e.g.; 1-6]. Fluid inclusions are extremely small, typically less than 30 μm, and a single mineral grain contains several generations of fluid inclusions with distinctly different compositions. As a consequence, high sensitive microbeam analyses of individual fluid inclusions in the grain are essential. Owing to its high spatial resolution, non-destructive character and high sensitivity for almost element (Z>22), proton-induced X-ray emission (PIXE) is a reliable technique for quantitative element analysis of single fluid inclusions [7-9]. In this study, we have reported determinations of trace elements in fluid inclusion from hydrothermal quartz and examined the relationship with vein-type skarn Fe-Cu deposits.

The quartz sample was collected from Kawahage quartz veins at Kawakami village, Nagano Prefecture in the central Japan. The quartz veins intrude Mesozoic sandstone, mudstone and limestone strata and has a genetically relationship to the Kinpusen biotite-granite body at the distance, 2 km, from the veins. Fe-Cu mines of skarn type are also present near the veins and are regarded as the same hydrothermal generation with the veins. The quartz veins are simple quartz veins and consisted partly of a skarn body formed by reactions with the calcareous country rock. The main quartz part had a large amount of rock crystals and a small amount of chlorite and native gold. The skarn part contained calcite, quartz, hedenbergite, vesvianite, andradite, scapolite, pyrite, pyrrhotite, chalcopyrite. Measured fluid inclusions in the specimen were included in a milky quartz crystal, 5 cm in length, from the main quartz part. The quartz crystal sample was cut parallel to the C axis, 500 μm in thick, and was mounted on a slide glass and polished; then were coated with a carbon film to avoid the charging-up. The measured fluid inclusions were selected from a trail of secondary inclusions with negative crystal shapes, 30-170 μm in size, and contained saline water, vapor bubbles, and NaCl crystal (Fig.1). The estimated NaCl equivalent concentration was of ca. 30% and the inclusion depth was 12 to 20 μm.

These samples were measured by the PIXE facility at the Tandem Accelerator Center, the University of Tsukuba [10]. A 0.1 to 0.4 nA beam of 4-MeV proton was focused to a 50 x 100 μm spot on the sample using slits and magnetic lenses. The incidence beam angle was normal to the sample surface, and the X-ray measurement take-off angle was 45˚. Analytical points were chosen based on optical viewing using a CCD camera mounted on the microscope. The characteristic X-rays excited by the incident beam were collected by the Si(Li) X-ray-energy

Fig. 1
Photomicrograph of fluid inclusions in quartz crystal from Kawahage. The inclusions contained saline water, vapor bubbles, and cubic NaCl crystal (white arrow). Scale bar is 200 μm.

detector with a nominal resolution of 145 eV at 5.9 keV, and the spectra were recorded by a multi-channel analyzer. A graphite plate, 1.3-mm thick, was located between the specimens and the detector in order to attenuate the intense X-rays from the light major elements. The total charge was determined by integrating the target currents, and all samples were analyzed to the integrated charges of 0.5 to 5.0 μC.

The measured X-ray intensity for each element was converted to the elemental concentration by the developed quantification method using sensitivity curve [11]. The method included three calculations necessary for X-ray analyses of inclusions buried in matrix: 1) energy loss of incident protons in the matrix; 2) intensities of characteristic X-rays emitted from the inclusion; and 3) absorption of the X-rays by the matrix. Sensitivities of the detector for each element was determined by measurements of multi-element reference glass material NIST SRM 1412 (Table 1). The sensitivity was a maximum at Fe, so that the present analytical condition was suitable to determinations of transition metal elements. By using the method, trace elements in fluid inclusions at levels of a few to several thousands μg g^{-1} can be determined with the precision of ±11 % [11]. Detection limits for the measurements depended mainly on elemental species and the integrated charge. The lowest run detection limits with the integrated charges of 5.0 μC were of 1.8 x 10^{-13} g for Ga and 5.7 x 10^{-11} g for Ba. For measurements of fluid inclusion with 30 μm diameter, estimated detection limits for Ga, the most easily detectable, was of a few μg g^{-1}.

Observed spectra of the fluid inclusions consisted mainly of the K-X ray peaks from Ca, Mn, Fe, Ni, Cu, Zn, Ga, Br, Rb, Sr, and the L-X ray peaks from Pb (Fig. 2). These peaks were present in all the inclusions in the same trail. L-X ray peaks from Ba, La, and Ce were also visible in large inclusions, 150 μm length (Fig. 2). In addition, small Cu peak was detected from the quartz matrix, so that fluid inclusion contents were quantified by subtracting contributions of Cu in the matrix to the inclusion contents. Determined concentration of the

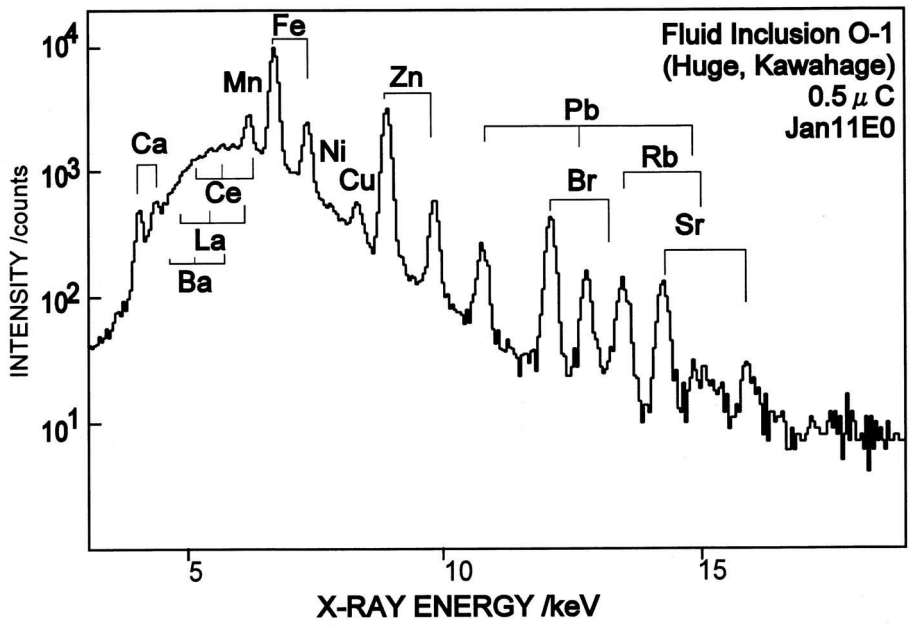

Fig. 2
X-ray spectrum of large single fluid inclusion recorded using 0.5 μC of 4 MeV protons with 1.3 mm graphite.

large inclusion was shown in Table 1. Ba, La, and Ce, were unable to be determined due to the small intensities. The determined values of Mn, Fe, and Cu, were 2-3 orders of magnitude higher than those of cold spring water near the veins [12], indicating higher transition metal contents in the hydrothermal fluid related with ore formations. By considering a fractionation of Cu-Pb-Zn in hydrothermal fluid, features of the lower Cu, higher-Zn and -Pb have demonstrated a generation of the fluid at shallower depth conditions: it consisted with geological occurrences and mineral assemblages of the veins and the adjacent skarn mine. The presence of La and Ce has shown a strong contribution of residual components generated by crystal fractionations of granite to the fluid. In addition, the high concentration of Ca agreed with an occurrence of the skarn part in the veins, showing Ca supply in the fluid from the calcareous country rock.

The present results have proven that the fluid in the inclusions contained transition metal elements and Ca at several 100-1000 μg g^{-1} level and detectable light rare earth elements. These chemistries have indicated a fluid generation by the mixture of granitic and country rock components and by the Cu-Pb-Zn fractionation at a relatively shallower depth conditions (~1 kb). In the future, it would be required further elucidation of origin for these transition metals, for example, crystal fractionation of granite or scavenging them from

Table 1. PIXE analyses of single fluid inclusion in quartz crystal.

	X-ray intensity (cts)	sensitivity (cts (μC cm^{-2})$^{-1}$ g^{-1})	concentration (μg g^{-1})
Ca	1018	707147919	6781
Mn	4553	13473129052	365
Fe	33103	15326418531	2189
Cu	1275	13385639168	71
Zn	12466	11381919498	891
Br	1834	3548738939	400
Rb	612	2139246646	214
Sr	550	1671372584	246
Pb	1202	1870619833	491

sedimentary rock. As further works, analyses of fluid inclusions in the hydrothermal veins are in progress.

References

[1] J. D. Frantz, H. K. Mao, Y.-G. Zhang, Y. Wu, A. C. Thompson, J. H. Underwood, R. D. Giauque, K. W. Jones and M. L. Rivers, Chem. Geol., 69 (1988), 235.

[2] L. W. Diamond, D. D. Marshall, J. A. Jackman and G. B. Skippen, Geochim. Cosmochim. Acta, 54 (1990), 545.

[3] A. H. Rankin, M. H. Ramsey, B. Coles, F. Van Langevelde and C. R. Thomas, Cosmochim. Acta, 56 (1992), 67.

[4] T. J. Shepherd and S. R. Chenery, Cosmochim. Acta, 59 (1995), 3997.

[5] P. Philippot, B. Menez, P. Chevallier, F. Gibert, F. Legrand and P. Populus, Chem. Geol., 144 (1998), 121.

[6] A. Audetat, D. Gunther, C. A. Heinrich, Science, 279 (1998), 2091.

[7] C. A. Heinrich, C. G. Ryan, T. P. Mernagh and P. J. Eadington, Econ. Geol., 87 (1992) , 1566.

[8] C. G. Ryan, C. A. Heinrich, and T. P. Mernagh, Nucl. Instrum. Meth. Phys. Res. B77(1993), 463.

[9] M. Kurosawa, S. Shimano, T. Kato, S. Sueno, K. Shima and S. Ishii, UTTAC-67 annual report (1998), 112.

[10] M. Kurosawa, S. Sueno, K. Shima, H. Ohshima, S. Ishii, H. Kamiya, S. Kimoto, H. Ohyi and K. Hayashi, Nucl. Instrum. Meth. Phys. Res. B142 (1998), 599.

[11] M. Kurosawa, S. Shimano, T. Nakajima, T. Kato, S. Sueno, K. Shima and S. Ishii, UTTAC-68 annual report (1999), 94.

[12] K. Sugihara and T. Shimaguchi, Sci. Rep. Edu. Yamanashi Univ. 36 (1985), 23.

4.2 Permeability modification of rat intestine induced by inflammation shown with PIXE measurement

K.Nakao[1], Y. Suzuki[1], Y. Saito[1], I. Tamanoi[2], K.Shima, S. Matsumoto[3]

1. Introduction

Intestinal tract, in particular small intestine, plays a part in control of digestion and absorption of nutrient, while defending from poison, bacteria, virus and so on. Inflammatory bowel disease, Crohn's disease and ulcerative colitis, are multi-factorial disorders whose etiology remains unknown. Although the exact pathogenesis is poorly understood, there is evidence that it involves interactions among the immune system, genetic susceptibility, and the environment, most notably the bacterial flora. In patient with Crohn's disease, the intestinal inflammation mainly occurs in small intestine. It is difficult to evaluate technically the severeness of the disease in small intestine by endoscopic and radiographic examinations. Activity of the disease is evaluated by clinical symptoms and sub-clinical features, for example, laboratory data by blood test. In patient with the inflammatory bowel disease, abnormal increase in intestinal permeability has been responed as a characteristic symptom. It is afraid that substances which can't be usually uptaken by the organ permeate through the mucosa. Current methods to measure intestinal permeability need much time and also laborious work. More simple method to measure intestinal permeability is desired.

We measured the intestinal permeability of mice by PIXE method, as one of the methods to assess the activity of intestinal inflammation. PIXE method is able to measure a small amount of elements, which is not easy to measure with usual one. We successively measured the amount of element in blood after oral administration of heavy metals such as rubidium, manganese to mice[1-5]. The usefulness of PIXE method is presented in measurement of intestinal permeability.

2. Materials and Methods

2.1. Animals and inflammation induction

We used Sprague-Dawley male rats (weight 200-250g) of 7 weeks old. These rats were obtained commercially from Japan SLC. Inflammation was induced with injection of indomethacin with an amount of 10mg/kg/day, which was solved in 5% sodium hydrogen-carbonate ($NaHCO_3$). Physiological saline solution was injected to control groups.

2.2. Sample preparation

A mixture solution of 300mg of rubidium chloride (RbCl), 52.0 mg of manganese chloride ($MnCl_24H_2O$) and 18.7mg zinc chloride ($ZnCL_2$), was administered orally into rats. The amount of RbCl, $MnCl_2$ and $ZnCL_2$ administered was calculated from LD50 in rat according to Merk Index. After the

1 School of Medicine, Chiba University, 1-8-1, Inohana, Chuou-ku, Chiba-shi 260
2 National Institute of Radiological Sciences, 4-9-1, Anagawa, Inage-ku, Chiba-shi 263
3 Chiba Institute of Technology, 2-1-1, Shibazono, Narashino-shi 275-0023

administration of RbCl, $MnCl_2$ and $ZnCL_2$, blood was drawn from vein into a heparinized glass capillary tube at 0, 15, 30 min and l, 2 and 4 hrs. Drawn bloods in capillaries were centrifuged for 5 min to read hematocrit values. 10μ 1 of plasma after centrifugation were deposited on a polycarbonate membrane filter (Nuclepore, Costar Scientific Corporation,0.1μm pore size, 6 μm thick and 25 mm in diameter) with a micropipette for PIXE analysis, as described previously [1-5]. The specimens of plasma were dried under a room temperature and used for PIXE analysis.

2. 3 PIXE measurements

Specimens of the plasma were bombarded with proton beams of 1.52 MeV from a Tandetron accelerator installed at Accelerator Center of Tsukuba University for an accumulated charge of 2000 nC [6]. The beam spot was 2 mm in diameter and the current was kept at 5 - 8 nA. The measurement of X-rays was carried out with a Si (Li) detector. The method of PIXE measurement and analysis were described in previous papers [1-5].

3. Results

Changes of each element contents after Rb+Mn+Zn administration was obtained with the analysis of element contents in rats by PIXE method. Figure 1 shows changes in the relative amounts of Rb after the administration. The variation curves according to the injection times of indomethacin indicate gradual increases with no significant differences between the single injection group and none. In comparison with twice injection group, the content in the twice injection increased clearly after 30min to 2hrs with ratios higher than the control and the single.

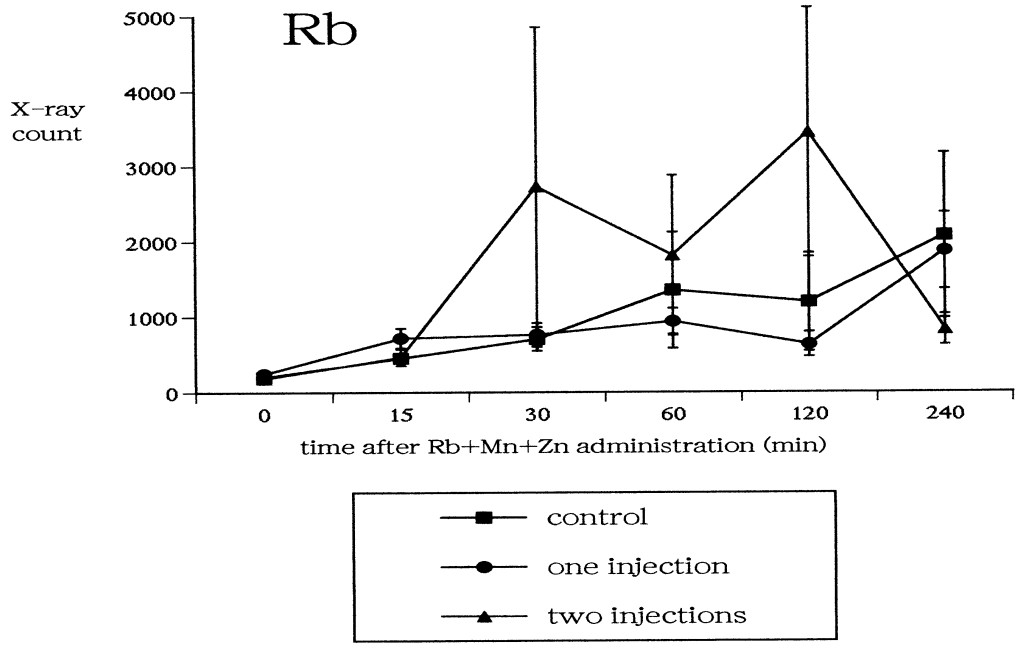

Fig.1 Variation of Rb content in the plasma of rats injected with indomethacin after the administration of the tracer elements of Rb, Mn and Zn.

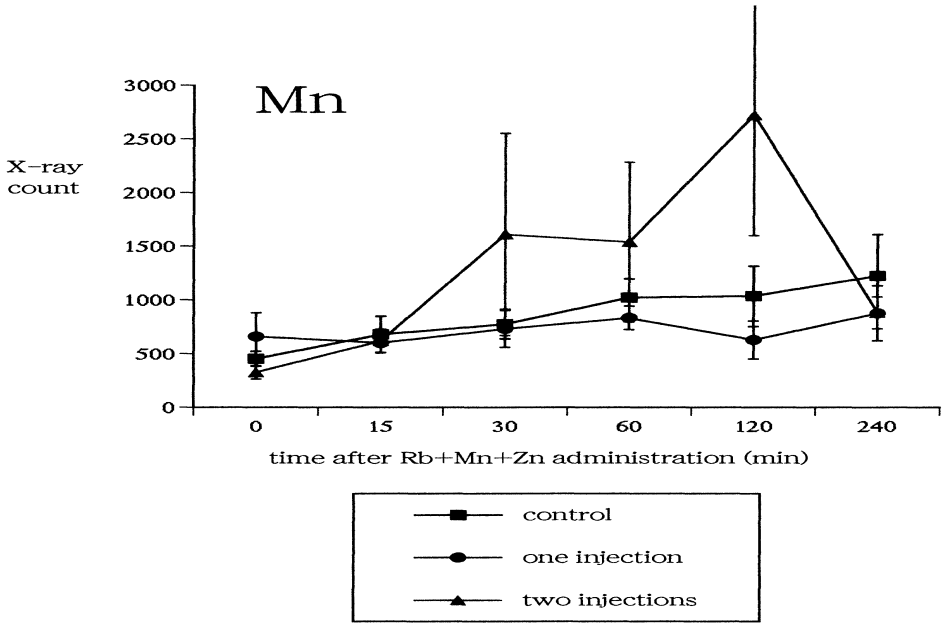

Fig.2 Variation of Mn content after the administration.

Figure 2 shows changes in the relative amounts of Mn after the administration. The curves in the figures behaved similarly to the correspond data in Fig.1. The amount of Mn in the twice injection group increases slightly with a low rate until 30 min after the administration; but begins to increase remarkably at the point. The value in the plasma reaches maximum at 2hrs and then decreases. Gradual increases in the control and the single injection group, however, continued until 4hrs.

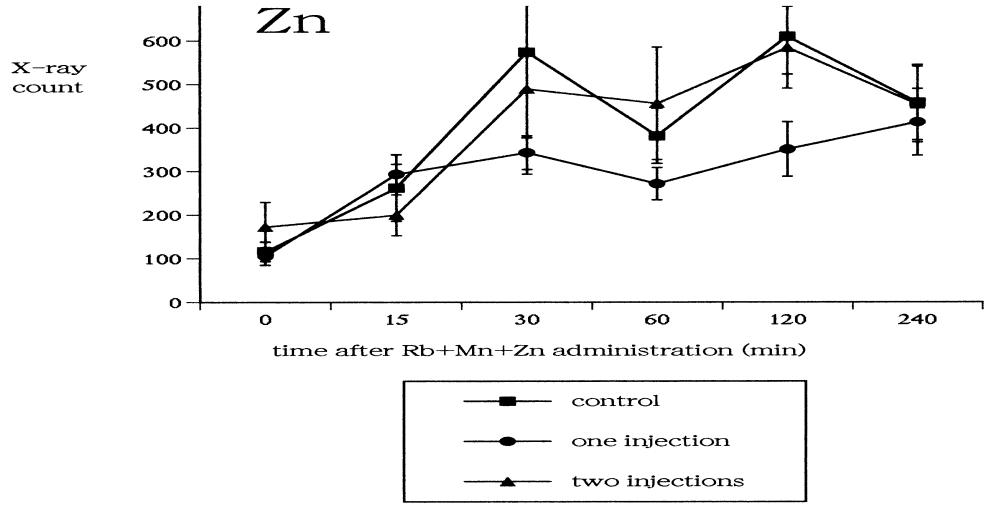

Fig.3. Variation of Zn content after the administration.

On the contrary, the content of Zn behaved differently as shown in Fig.3. All of the curves seem to be interpreted as gradual increase with maximum at 2hrs. There are no apparent difference among the

three groups as observed in Fig.1 and 2. Thus, the tracer of zinc exhibited a different response to inflammation of intestine.

4. Discussion

The Rb content in control group is very little. There is little or no Rb in normal mouse blood. After the administration of Rb, it is taken up by the intestinal mucosa into blood and its content increases. The values of Rb and Mn reached maximum at 2hrs after the administration and decreases. Rb is probably transferred into plasma from intestinal mucosa at first and subsequently moves into blood cells.

Increases in the elements of Rb and Mn in the twice injected samples are clearly observed after the oral administration. There is a little Mn in normal mouse blood. After the administration, Mn is taken up by the intestinal mucosa into blood and the Mn content increases. This result suggested that intestinal mucosal barrier was destroyed by inflammation and intestinal permeability upraised. They are probably permeated into blood from intestinal mucosa. Recently the intestinal permeability has been noted as one of the indicators to assess the activity of inflammatory bowel disease, for example Crohn's disease [7-9]. In patients with Crohn's disease, the tight junctions appear to be abnormal with increased separation between cells and abnormalities in the structural strands of the tight junctions [7]. Wyatt *et al*.[8] measured intestinal permeability in patients with Crohn's disease using the lactulose-mannitol test. Each subject was administered with a solution containing mannitol and lactulose. Urine was collected for next 5 hrs. Lactulose and mannitol in the urine were measured. The permeability index (lactulose/mannitol) was significantly higher in patients than in controls. A significant correlation was found between the value of the permeability index and the probability of clinical relapse in Crohn's disease. These results show that increases in intestinal permeability precede relapse in the disease and so are an indicator of sub-clinical disease. Howden *et al*.[9] measured intestinal permeability in patients with Crohn's disease using the ^{51}Cr-EDTA test. Each subject was orally administered ^{51}Cr-EDTA. Urine was collected over the next 24 hrs to measure ^{51}Cr-EDTA in the urine. Small intestinal permeability to ^{51}Cr-EDTA was raised in patients with Crohn's disease affecting the small intestine, and the degree of permeability is correlated with some measures of disease activity. On the other hand, urinary excretion of ^{51}Cr-EDTA was not elevated in patients with Crohn's disease who were judged to be in clinical remission or in their apparently healthy first-degree relatives. Above-mentioned methods have been applied to measure intestinal permeability. However, these methods have difficulty in practice, since they need much more time for measurement and also laborious work. Radioisotopes, such as ^{51}Cr-EDTA, are radio toxin. More easy and safe method to measure intestinal permeability is desired.

5. Summary

In this study, we found that the element contents of Rb and Mn increased to peak level at 2 hrs after the administration. These were conspicuously observed in the plasma of the rats with intestine inflamed by twice injection of indomethacin in contrast with the Zn contents. It is possible to assess intestinal permeability to compare the element contents of Rb and/or Mn at a short time after the administration. Rb and Mn are useful as one of the tracers to study of intestinal disease with measurement by PIXE method.

The merit of this method with Rb and Mn tracers lies in its high sensitivity. They are easily and clearly detected in the samples with PIXE method after the administration, in contrast with negligibly lower levels of these element in normal mouse blood. Thus, intestinal permeability can be measured more simply by PIXE method than other methods. At present, we are trying to induce the experimental animal models of inflammatory bowel disease [10] and to measure intestinal permeability by PIXE method. Further investigations are in progress.

References

[1] K. Nakao, Y. Suzuki, R. Sato, Y. Saito, I. Tamanoi. S. Matsumoto. H. Joshima, H. Imazeki, Possible application of PIXE method to intestinal permeability measurement. Int. J. PIXE, 7, 219-231(1997)

[2] K.Hoshikawa, I.Tamanoi, A.Nakamura, M.Kachi, K.Ohashi. S.Matsumoto, Possible characterization of mouse strain by plasma analysis with PIXE. Int. J. PIXE. 4, 97-106. (1994)

[3] I.Tamanoi, A.Nakamura, K.Hoshikawa. M.Kachi. B.Goto. H.Joshima, S.Matsumoto, Changes of blood plasma element contents in X-ray irradiated mice by PIXE analysis. Int. J. PIXE. 5. 85-95. (1995)

[4] I.Tamanoi. A.Nakamura, K.Hoshikawa, M.Kachi, K.Ohashi. B.Goto. H.Joshima, S.Matsumoto, PIXE studies on potassium and calcium in mouse blood plasma after transplantation of EL4 tumor cells, Int. J.PIXE, 5, 255-264, (1995)

[5] I.Tamanoi, S.Ishizuka, S.Matsumoto, H.Joshima, H.Imazeki, K.Nakao, R.Sato, Y.Suzuki, PIXE studies on the gastro-intestinal syndrome induced by radiation. Proceedings of the 34th Seminar on Science and Technology, Small Accelerators & Their Application, 203-221, (1997)

[6] S.Matsumoto, M.Seki, H.Shima, T.Ishihara, Proton irradiation effect on the conductivity and the surface structure of polymer materials. UTTC Annual Report 67, 118-121 (1999)

[7] D.Hollander. Crohn's disease - a permeability disorder of the tight junction?. Gut, 29, 1621-1624. (1988)

[8] J.Wyatt, H.Vogelsang, W.Hubl, T.Waldhder, H.Lochs, Intestinal permeability and the prediction of relapse in Crohn's disease, Lancet, 341, 1437-1439, (1993)

[9] C.W.Howden, I.Gillanders, A.J.Morris, A.Duncan, B.Danesh, R.1.Russell, Intestinal permeability in patients with Crohn's disease and their first degree relatives, Am. J. Gastroenterology, 8, I 175-1176, (1994)

[10] C.O.Elson. R.B.Sartor. G.S.Tennyson, R.H.Riddell, Experimental models of inflammatory bowel disease, Gastroenterology, 109, 1344-1367, (1995)

4.3 A proposed method of the determination of the number of hydrogen atoms in a standard target for hydrogen analysis

K. Furuno, H. Ohshima, K. Sasa, Y. Sasaki, K. Yamada, S. Yokose, M. Ishizuka
and T. Komatsubara

A standard hydrogen target used in the hydrogen analysis by means of resonant nuclear reaction(RNRA) must fulfill several conditions. An important condition is that the number of hydrogen atoms per unit area in the target is known. In previous works, the number of hydrogen atoms was determined by weighing[1] or by normalizing the yield of a target to that obtained with such an organic material as Kapton[2]. In this report, we propose an alternative method. It is the simultaneous observation of the angular distribution of γ rays and the α-γ angular correlation for the H(^{19}F,$\alpha\gamma$) reaction at the bombarding energy of the 16.44 MeV resonance. Although this proposed method could be applied to the H(^{15}N,$\alpha\gamma$) reaction, the following discussions are referred to the H(^{19}F,$\alpha\gamma$) reaction only. Elastic recoil protons can also be observed with the identical target-detector arrangement simultaneously. This is also used to measure the hydrogen concentration as described below.

1. Resonant nuclear reaction and elastic scattering by protons

It is well known that the ^{1}H(^{19}F,α,γ)^{16}O reaction can be employed to detect hydrogen atoms in materials. Many resonances are observed in this reaction at energies of ^{19}F ions between 4 and 26 MeV(lab). In this energy range, the resonance at $E(^{19}\mathrm{F})_{lab} = 16.44$ MeV shows the largest cross section of 590 mb. This resonance was investigated by Seed and French[3] and Peterson[4]. The experimental data are summarized in ref[5]. As indicated in Fig. 1, the system consisting of a proton and ^{19}F forms a compound nucleus ^{20}Ne at an excitation energy of 13.676 MeV, when the laboratory energy of ^{19}F reaches 16.44 MeV which corresponds to $E_{cm} = 0.828$ MeV in the center of mass system.

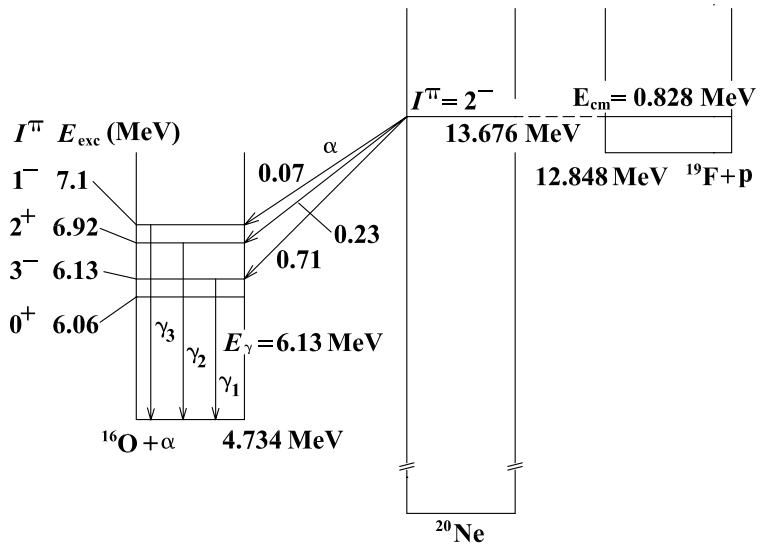

Figure 1: An energy diagram of ^{1}H(^{19}F,$\alpha\gamma$)^{16}O resonant reaction. The branching ratios of 0.71, 0.23, and 0.07 for the α decay from the $I^\pi = 2^-$ compound state to the 6.13, 6.92, and 7.1 MeV state in ^{16}O are average values of two different data reported in ref[3] and [4].

From the spins and parities of the proton, ^{19}F and of the state of the compound nucleus ^{20}Ne, the orbital angular momenta should be odd in the entrance channel. The dominant partial wave is p wave at low center-of-mass(c.m.) energies. The resonance width Γ is reported to be 4.5 keV in the laboratory system, if we observe the resonance by the bombardment of protons on ^{19}F target.

The 2^- compound state decays into the excited states in ^{16}O *via* α-particle emission. The transitions to

the ground and the first excited 0^+ state are forbidden from the parity rule. Dominant transitions are those to the 6.13 and 6.92 MeV state, while the transition to the 7.12 MeV state is weak.

The measurement of the number of hydrogen atoms can be accomplished by observing α-particles or γ rays emitted from the 6.13, 6.92 and 7.12 MeV state in ^{16}O. It should be noted here that the α-particles and γ rays are emitted in successive transitions. One nuclear reaction produces one α-particle and one γ ray. The lifetime of the 6.13 MeV state is measured to be 24 ps, and the 6.92 and 7.12 MeV state are also shortlived states. The emission of α-particles and γ rays can be substantially regarded as simultaneous emission in comparison with the resolving time of a conventional detection system.

In the ^{1}H(^{19}F,$\alpha\gamma$)^{16}O reaction, the kinetic energy of α-particle is high enough at forward angles because of large c.m. velocity in the reaction kinematics. It is about 11 MeV(lab) at 0° at an incident ^{19}F energy of 16.5 MeV. The range of this α-particle is much longer than that of incident ^{19}F ions. Therefore, if we place an appropriate absorber foil behind a thin target which includes hydrogen atoms, ^{19}F ions stop in the absorber foil, whereas α-particles pass through the foil. We can observe the α-particles at forward angles.

Recoil protons produced in the elastic scattering of ^{19}F on H in the target are emitted with energies around 3 MeV at forward angles near the beam direction. Since the energy loss of protons is low, recoil protons pass through the target and absorber foil. It is not always obvious whether the ^{19}F+p scattering is pure Coulomb scattering or not, because the detection of protons in the forward angle corresponds to the extremely backward scattering of ^{19}F. It should be noted, however, that the Coulomb barrier is as high as 2.45 MeV in the c.m. system. It is about three times as high as the c.m. energy of 0.828 MeV at 16.44 MeV resonance. If we assume the pure Coulomb scattering for the ^{19}F+p system at 0.828 MeV, the yield of recoil protons gives the number of hydrogens in the target according to ERDA method. The solid angle of the α-particle detector must carefully be calibrated in this case.

2. The principle of the proposed method

The method consists of the *simultaneous* observation of a singles α-particle spectrum, a singles γ-ray spectrum and α-γ coincidence spectrum at the resonance energy for the incident ^{19}F ions. The α-particle detector can be designed in such a way that recoil protons can be observed simultaneously.

If we observe α-particles at an angle of $(\theta_\alpha, \varphi_\alpha)$ and γ rays at an angle of $(\theta_\gamma, \varphi_\gamma)$ with respect to the incident beam, the yield of α-particles obtained in the singles mode is given by

$$Y_{\rm singles}(\alpha;\, \theta_\alpha) = I_0\, n\, x \cdot \left(\frac{d\,\sigma(E_R,\, \theta_\alpha)}{d\Omega_\alpha}\right)_{\rm lab} d\Omega_\alpha \varepsilon_\alpha. \tag{1}$$

If the target and the incident beam are not polarized, the cross section does not depend on the azimuthal angle φ_α. In the above expression, I_0 stands for the number of incident ^{19}F ions, n is the number of hydrogen atoms per unit volume, x denotes the thickness of the target, $d\sigma(E_R, \theta_\alpha)/d\Omega_\alpha$ is the differential cross section of the reaction at the resonance energy E_R, $d\Omega_\alpha$ means the solid angle of the α-particle detector. The symbol ε_α is the detection efficiency of the α-particle detector, but this can be put to unity in most of the cases. The energy resolution of the α-particle detector must be high enough to resolve the transition to the 6.13 MeV state from that to the 6.92 MeV state in ^{16}O.

The yield of γ rays is written as

$$Y_{\rm singles}(\gamma;\, \theta_\gamma) = I_0\, n\, x \cdot \sigma(E_R) W_S(\theta_\gamma) \frac{d\Omega_\gamma}{4\pi} \varepsilon_\gamma, \tag{2}$$

where the cross section $\sigma(E_R)$ is the integration of the differential cross section in eq(1) over the whole solid angle. This is the value of the Breit-Wigner formula at the resonance energy E_R. The function $W_S(\theta_\gamma)$ is the angular distribution of γ rays. The energy resolution of the γ-ray detector must be high enough to resolve two transitions to the excited states in ^{16}O mentioned above.

Since the resonance is a p-wave single resonance in good approximation, the angular distribution of γ rays is not isotropic. The general expression of the angular distribution is expanded in a series of Legendre functions as follows;

$$W_S(\theta_\gamma) = \sum_{L=0,\, even} a_L P_L(\cos\theta_\gamma) \tag{3}$$

with the normalization of $a_0 = 1$. The solid angle and the detection efficiency of the γ-ray detector are expressed by $d\Omega_\gamma$ and ε_γ, respectively. In practice, these are not independent; the product in the form of $(d\Omega_\gamma/4\pi)\varepsilon_\gamma$ can be calibrated.

The α-γ coincidence yield is given by

$$Y_{\rm coin}(\alpha,\,\gamma;\,\theta_\alpha,\,\theta_\gamma) = I_0\,n\,x\cdot\left(\frac{d\,\sigma(E_R,\,\theta_\alpha)}{d\Omega_\alpha}\right)_{\rm lab} d\Omega_\alpha\varepsilon_\alpha W(\theta_\alpha,\,\theta_\gamma,\varphi_\gamma)\frac{d\Omega_\gamma}{4\pi}\,\varepsilon_\gamma, \tag{4}$$

where $W(\theta_\alpha,\,\theta_\gamma,\varphi_\gamma)$ denotes the α-γ angular correlation function. This correlation function is greatly simplified if α-particles are observed in the beam direction($\theta_\alpha = 0^\circ$)[7]. In this case, the correlation function does not depend on the azimuthal angle φ_γ, and is given by the following form similar to eq(3);

$$W(\theta_\gamma) = \sum_{L=0,\,even} A_L P_L(\cos\theta_\gamma) \tag{5}$$

with the normalization of $A_0 = 1$.

The calibration of the detection efficiency of the γ-ray detector is performed as follows. At first, we measure the yields of $Y_{\rm singles}(\alpha;\,\theta_\alpha = 0^\circ)$, $Y_{\rm singles}(\gamma;\,\theta_\gamma)$, and $Y_{\rm coin}(\alpha,\,\gamma;\,\theta_\alpha = 0^\circ,\,\theta_\gamma)$ simultaneously at angles of θ_γ as many as possible. The energy of the incident beam should be chosen to be the resonance energy at 16.44 MeV. From eqs. (2) and (4), we obtain following ratios;

$$R(\theta_\gamma) = \frac{Y_{\rm coin}}{Y_{\rm singles}(\alpha)} = W(\theta_\alpha,\,\theta_\gamma)\frac{d\Omega_\gamma}{4\pi}\,\varepsilon_\gamma \simeq \{1 + A_2P_2(\cos\theta_\gamma) + A_4P_4(\cos\theta_\gamma)\}\frac{d\Omega_\gamma}{4\pi}\,\varepsilon_\gamma. \tag{6}$$

In this last expression, the Legendre expansion is limited within $L = 4$ for simplicity. The detection efficiency $(d\Omega_\gamma/4\pi)\varepsilon_\gamma$ can be derived from the zero-th order coefficient of the fit of experimental ratios R to the series of Legendre functions. It should be noted that this efficiency is only for the energy of 6.13 MeV. Since the factors of I_0, nx, Ω_α and ε_α are canceled by the fact that yields are observed simultaneously with an identical condition for beam irradiation and the target-detector arrangement. The yield of singles events is much more larger than coincidence events. Therefore, only the counting statistics of coincidence events contributes to the uncertainty of the detection efficiency in the zero-th order approximation.

After the calibration of the detection efficiency, we obtain the number of hydrogen atoms per unit area in the form of nx by fitting the observed yields $Y_{\rm singles}(\gamma;\,\theta_\gamma)$ to the Legendre expansion (see eqs. (2) and (3)). Since the detection efficiency is measured for only 6.13 MeV γ rays, the measurement of the angular distribution should be perfomed for only this γ rays. The cross section $\sigma(E_R)$ in eq(2) must be the partial cross section through the 6.13 MeV state in ^{16}O. This cross section is measured to be 440 ± 13 mb by Becker *et al*[8]. The determination of the value of nx by ERDA method is an independent experiment, so that it provides a good check for the measurements.

3. Test experiment

An experiment was carried out to test the validity and feasibility of the proposed method described above. An α-γ coincidence events were accumulated with a silicon solid-state detector placed at 0° for α-particle detection and 5 Ge γ-ray detectors arranged in a ring geometry at 63.5° with respect to the beam. The target used was a 2 μm thick titanium foil. Hydrogen adsorption was performed in hydrogen atmosphere at 400°C. In this experiment, however, the energy resolution of α-particle detector was inadequate. The singles events of α-particles were estimated from a comparison of spectrum shape between the singles and coincidence spectra.

The singles and coincidence counts of α-particles were obtained to be 8.5922×10^5 and 3.638×10^3 counts, respectively. The angular correlation was evaluated from the theoretical function assuming that the resonance is a single p-wave resonance associated with the $I^\pi = 2^-$ state in ^{20}Ne. The theoretical value at $W(\theta_\gamma = 63.5^\circ)$ is 0.8. With these values, we obtained the efficiency of the γ-ray detector to be 5.29×10^{-3}.

We measured hydrogen concentration of hydrated silica glass last year[9]. In this measurement, an obsidian sample was used as a reference of the hydrogen concentration. The experimental arrangement was

the same as the test experiment of the above α-γ coincidence experiment. The counts of 6.13 MeV γ ray was 10 counts per 1 μC for the obsidian sample. If we use the detection efficiency of 5.29×10^{-3} obtained above, the hydrogen concentration of the obsidian sample is calculated to be $nx = 6.9 \times 10^{14}$ [H/cm^2]. This value can further be converted to the concentration of water. It is 0.13 wt % H_2O, which is comparable with a value of 0.11 wt % H_2O obtained from the calibration by FTIR method. Since the error in the calibration of the detection efficiency is at least 10 % or more, the agreement would be reasonable. However, more elaborate experiments are clearly necessary, and will be continued together with the development of a new microbeam system for hydrogen analysis.

References

[1] Hjörvarsson, J. Rydén, T. Ericson and E. Karsson, Nucl. Instr. Meth. in Phys. Res. **B42** (1989) 257.

[2] L. Westerberg, L.E. Svensson, E. Karsson, M.W. Richardson and K. Lundström, Nucl. Instr. Meth. in Phys. Res. bf B9 (1985) 49.

[3] J. Seed and A.P. French, Phys. Rev. **88**, No. 5 (1952) 1007.

[4] R.W. Peterson, W.A. Fowler and C.C. Lauritsen, Phys. Rev. **96** No. 5 (1954) 1250.

[5] F. Ajzenberg-Selove, Nucl. Phys. **A475** No.1 (1987) 163.

[6] K. Spyrou, C. Chronidou, S. Harissopulos, S. Kossionidos and T. Paradellis, Zeit. Phys. **A357** (1997) 283.

[7] A.E. Litherland and A.J. Ferguson, Can. J. Phys. **39** (1961) 788.

[8] H.W. Becker, W.E. Kieser, C. Rolfs, H.P. Trautvetter and M. Wiesher, Z. Physik, **A305** (1982) 319.

[9] N. Yanagisawa, K. Fujimoto, H. Ohshima and K. Furuno, Annual Report of the Tandem Accelerator Center 1999, UTTAC-68, 2000, 113.

4.4 Preparation of standard targets for hydrogen analysis

K. Furuno, H. Ohshima, K. Sasa, T. Katabuchi, Y. Sasaki, K. Yamada, M. Ishizuka, S. Yokose,
and T. Komatsubara

A standard target for hydrogen analysis by means of the resonant nuclear reaction H(^{14}N,$\alpha,\gamma)^{12}$C or H(^{19}F,$\alpha,\gamma)^{16}$O must fulfill the following conditions.

1. The number of hydrogen atoms per unit volume is known.
2. The hydrogen concentration is reasonably high.
3. The hydrogen concentration is stable during ion bombardment.
4. It is suitable for use in high vacuum.
5. The chemical composition and density are well defined.
6. The electrical conductivity is reasonably high for reliable beam current integration.

Several organic films like Mylar, polystyrene, polyethylene and Kapton are attractive in the above items 1, 2, 4, and 5. All of these organic foils are insulator, so that thin coating with carbon or gold is necessary to avoid charge up or sparking on the target during ion bombardment. The most serious drawback of these organic foils, however, is that the yield of $gamma$ rays decreases as a function of the dose of incident ions. In other words, the concentration of hydrogen atoms is not stable under the beam irradiation.@

Several authors have reported the preparation of hydrogen bearing targets so far. Hjörvarsson *et al* prepared tantalum-hydride(TaH_x) samples by placing a $10 \times 10 \times 0.5$ mm Ta plate which was heated at 620 K for 24 hours in hydrogen atmosphere at a pressure of 900 mbar[1]. The average concentrations expressed by the ratio of atoms H/Ta were $0.41 \sim 0.51$. It was found that the concentration was uniform over the depth from 0.3 to 1.0 μm from the surface. The samples were shown to be stable during the beam irradiation and resistant to heat treatment at 420 K in vacuum for achievement of ultra high vacuum. The number of hydrogen atoms was calibrated by weighing method.

Westerberg *et al* investigated the performance of pyrolytic carbon and amorphous silicon as a hydrogen bearing target[2]. Although the thickness of the hydrogen bearing region that they tested was as thin as 0.3 μm, the stability under the ion bombardment was excellent in both of pyrolytic carbon and amorphous silicon.

Thin deuterated titanium targets were prepared by Fletcher for his experiments on the $D(d,p)$ and $D(d,n)$ reaction at very low energies[3]. A thin titanium layer was made on a thin carbon foil by electron-bombardment vacuum evaporation. The hydrogen adsorption was performed be heating the foil up to 400 $^{\circ}$C in hydrogen atmosphere.

One of the important problems in a standard hydrogen target is the calibration of the number of hydrogen atoms in the target. Hjörvarsson *et al* employed the weighing method. Westerberg *et al* normalized the γ-ray yield of pyrolytic carbon and amorphous silicon to that of organic films by extrapolating the yields to zero dose of incident ions. An alternative method of calibration is the use of such nuclear processes

as proton-proton elastic scattering, the simultaneous observation of α-particles produced by the H(^{19}F,α) reaction and recoil protons(ERDA) with a thin hydrogen bearing target, or the α-γ angular correlation in the reaction H(^{19}F, $\alpha\gamma$)^{16}O* on resonance. A progress report of our preparation for a stable standard target will be described below.

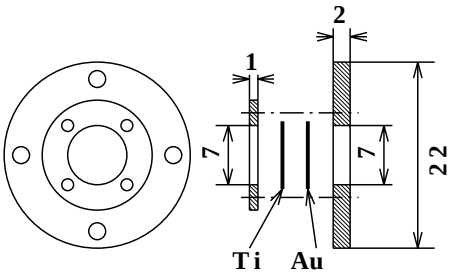

Figure 1: Target composition.

We tested the adsorption method at first. As shown in Fig. 1, a 2 μm thick titanium foil and a 5 μm thick gold foil were put between an aluminum disk and a washer. The aluminum disk was 2mm thick and 22 mm in diameter, while the washer was 1mm thick and 13 mm in diameter. Both of the aluminum disk and the washer had a hole of 7 mm in diameter at their center. A simple heater was fabricated using a 30×30 mm square of ceramic plate and an electric ribbon heater as shown in Fig. 2. The ribbon heater was made of a sheet of thin molybdenum(Mo). We wound a 0.1 mm thick, 5 mm wide and 150mm long Mo ribbon in a flat shape.

The target composition shown in Fig. 1 was placed in a vacuum chamber which was evacuated with a turbo molecular pump. The change in the

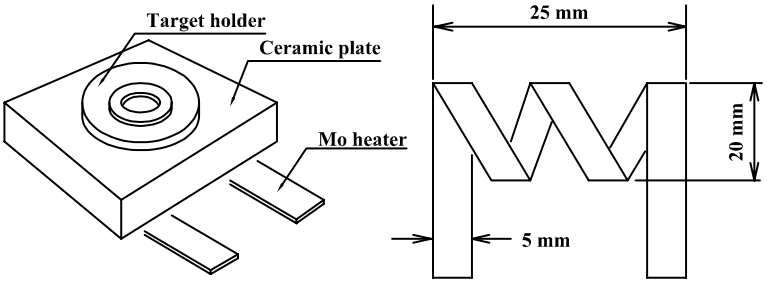

Figure 2: Heater.

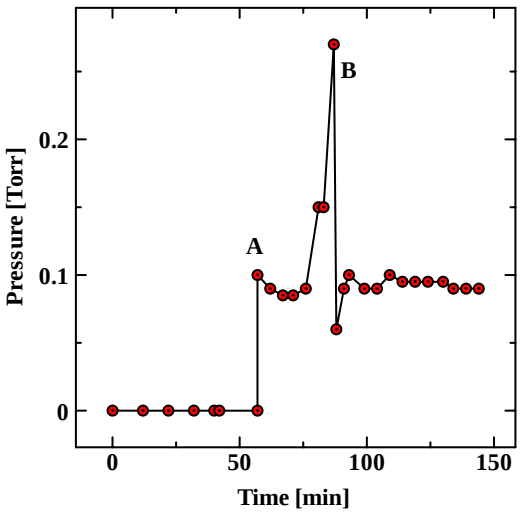

Fig. 3. Pressure during the adsorption.

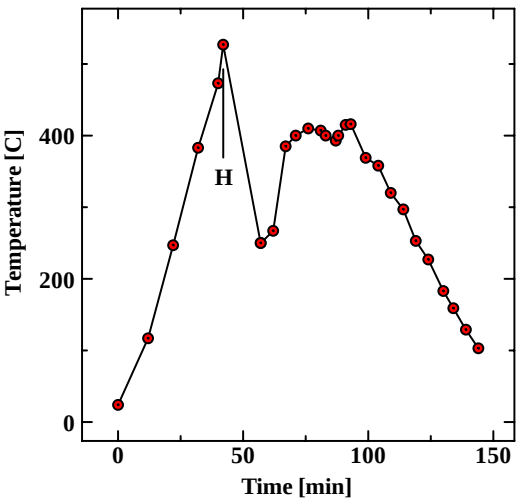

Fig. 4. Temperature during the adsorption.

pressure in the vacuum chamber and the temperature of the target composition, which was measured with a thermo couple at the edge of the washer of the target composition, are displayed in Fig.3 and Fig. 4. The degassing of the heater was carried out before the target composition was mounted on it. We increased the temperature of the target composition up to 527°C(see the mark H in Fig. 4). Hydrogen gas was introduced

into the chamber when the temperature was decreased won to 250°C(see the mark A in Fig. 3). The pressure change indicated by the symbol B in Fig. 3 occurred when we adjusted a needle valve to recover the pressure which was decreasing gradually. The titanium foil, however, was very fragile, and had got many wrinkles after this treatment.

Another method of the preparation was the implantation of H^- ions at an energy of 90 keV. The target composition was exposed to the H^- ion beam from our polarized ion source operated in the unpolarized mode. An aperture with 6 mm in diameter was placed just in front of the target. The H^- ion beam was swept using an electric deflector on which a saw-tooth voltage was applied. The target composition was mounted on a thick copper block which was cooled by a Peltier element at a temperature of -1.9°C. The integrated charge was 37460 μC.

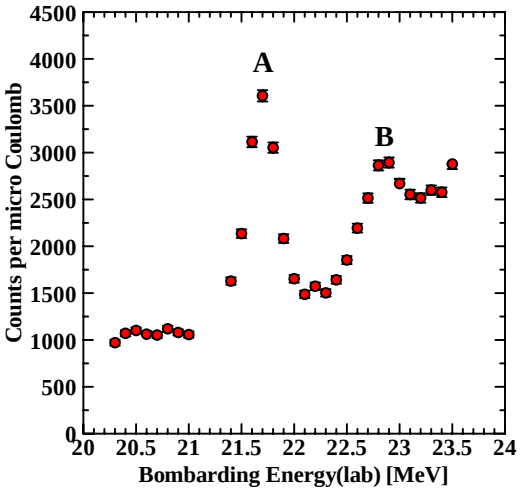

Fig. 5. The yield of 6.13-MeV γ rays as a function of the bombarding energy of ^{19}F ions

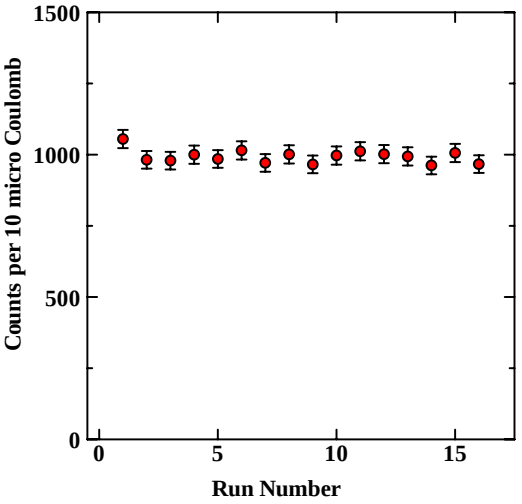

Fig. 6. The yield of α-particles from the H(^{19}F,α_2) reaction for every 10 μC accumulation runs

The depth profile of the implanted hydrogen ions was measured by observing the yield of 6.13-MeV γ rays from the H(^{19}F,α_2) reaction. The yield curve is shown in Fig. 5. The peak A in Fig. 5 corresponds to the 16.44 MeV resonance, while the peak B is due to the 17.6 MeV resonance. The shifts of these energies are ascribed to the energy loss of incident ^{19}F ions in the titanium foil, because the surface of the titanium foil exposed to the ^{19}F ions in the observation of γ rays and α particles was opposite to the surface on which the H^- implantation was performed.

The yield of reaction α-particles was measured every 10 μC with beam current of 50 nA. The results shown in Fig. 6 suggests that the target seems to be rather stable for beam irradiation.

References

[1] Hjörvarsson, J. Rydén, T. Ericson and E. Karsson, Nucl. Instr. Meth. in Phys. Res. **B42** (1989) 257.

[2] L. Westerberg, L.E. Svensson, E. Karsson, M.W. Richardson and K. Lundström, Nucl. Instr. Meth. in Phys. Res. bf B9 (1985) 49.

[3] K.A. Fletcher, Thesis, University of North Carolina at Chapel Hill (1993).

4.5 Status of Tsukuba AMS system

Y. Nagashima, R. Seki, D. Arai, T. Takahashi, and H. Kume[1]

Both of the beam transmission efficiency and the beam transmission stability are essentially important for the AMS studies. Up to now, an ion source part and a particle detection lines have a sufficient ability, but a tandem accelerator has insufficient

The energetic efforts of our AMS group are performed on the ^{36}Cl measurements this year. The ^{36}Cl to ^{35}Cl ratio of JCO samples are successively measured. The thermal neutron flux at the place of 10m apart from a criticality accidental point is estimated to be $2.5*10^{11}$ cm^{-2}. The results and some discussions are stated in this annual report with a title of " AMS ^{36}Cl measurement of JCO soils".

KEK concrete blocks for shielding radio-active beam are irradiated by very strong neutron flux and are strongly activated. From a view point of human health, it is useful to know the radio activity of the concrete blocks. Thus, ^{36}Cl contents are measured as a function of a distance from the radio-active beam. The results are listed and discussed in this annual report.

In order to know the influence of nuclear power plants to an environment, ^{36}Cl in soils are extensively studied. The ^{36}Cl is very suitable element to see the environmental changes for long term of period by the human with the nuclear associated activities because of both very long halftime, about 0.3 million years, and very low natural abundance, less than 10^{-14} of ^{36}Cl to ^{35}Cl ratio. The soils are sampled in the area of Tokai Village and in Tsukuba area as a reference. ^{36}Cl to ^{35}Cl ratio of Tokai samples are preliminary about a hundred times larger than that of Tsukuba samples. The investigations are still undergoing.

The development of a ^{129}I measurement technique has been almost succeeded. The terminal voltage of the 12UD tandem is stabilized by a slit current feedback system with the pilot beam method as well as the ^{36}Cl measurement. Fig. 1 shows an overall configuration of the ^{129}I AMS system. Both ^{129}I- and $^{97}MoO_2^-$ are generated simultaneously in the ion source and are transported to the 12UD tandem through two successive mass separators. One is 120degree with 300mm radius mass separator and another one is 90degree magnet with 900mm radius of curvature. ^{127}I- negative ions can be completely swept out and no ^{127}I- makes an invasion upon the tandem. Therefore, there is no request of particle identification such as a TOF detector for mass identification because a particle detector observes almost no ^{127}I elements. The AMS allows as isotopic sensitivity as low as one part in 10^{13} for ^{129}I with 126MeV particle energy. Thought the sensitivity is not so high, this number is enough to measure an iodine sample prepared from an environment because the background level of the sample is normally high, about 10^{-12}. A decrease of a transmission coefficient of the particle passing through a carbon stripper foil (5μg/cm2) is not observed in a 3 hours measurement of ^{129}I with 1nA $^{97}MoO_2^-$ pilot beam. $^{127}I^-$ is measured by a Faraday-cup which is located just after the 120degree magnet in the ion source system.

[1] National Institute for Environmental Studies

Configuration for the ^{129}I Measurements

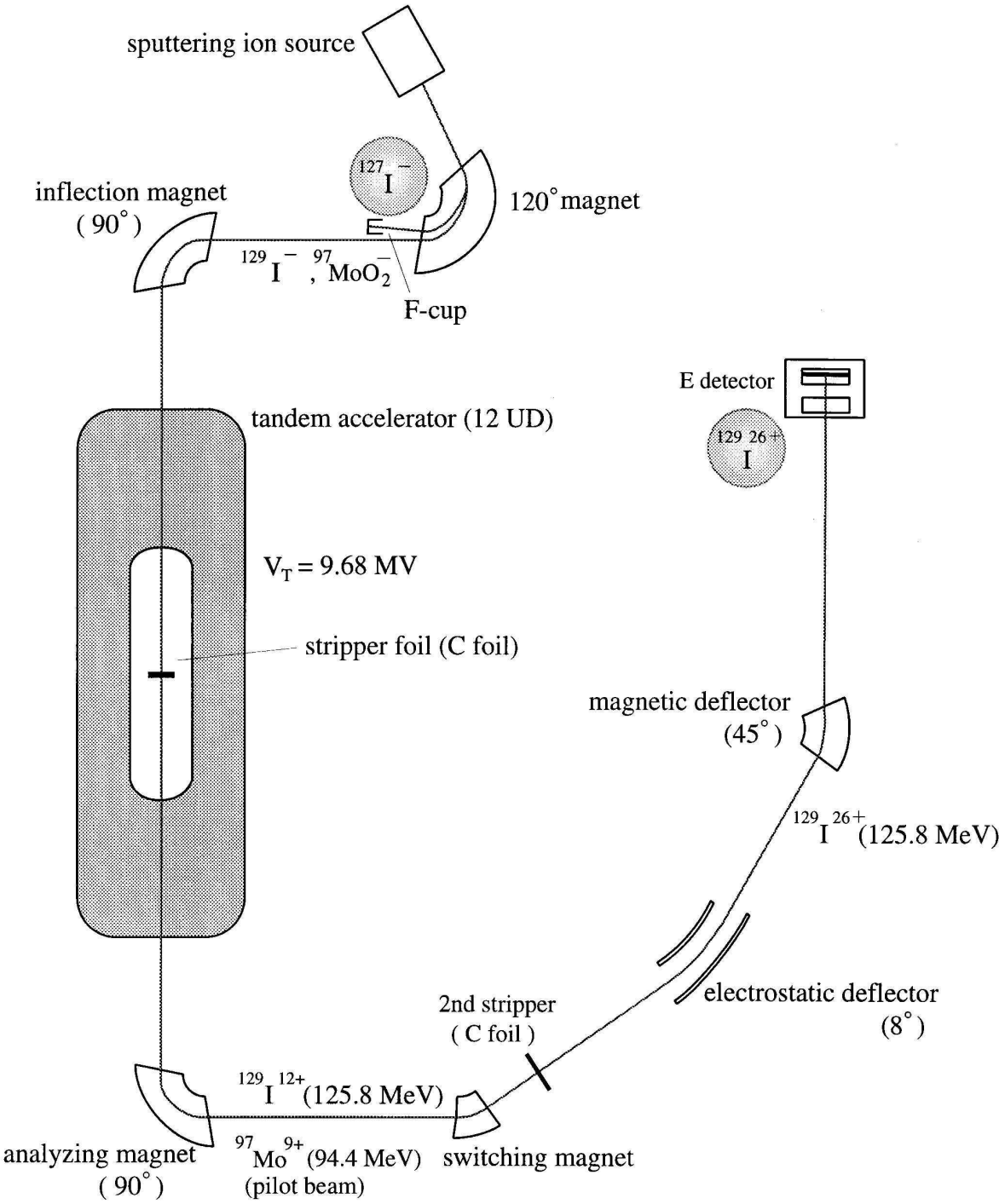

Fig. 1 system configuration of ^{129}I AMS

4.6 AMS ^{36}Cl measurements of KEK concrete shielding blocks

D. Arai, R. Seki, Y. Nagashima, T. Takahashi, T. Miura[1], K. Bessho[1], and S. Ishihama[2]

The 12GeV proton synchrotron of the KEK has been established for high energy physics and its related experiments for about twenty years since it has been constructed. A variety of radio-nuclide have been created in the shielding concrete through both thermal neutron capture process and nuclear spallation reactions. A quantitative information about radio-nuclides induced in the shielding concrete is very important not only for evaluating radiation doses for persons who are working in the radioactive circumstances, but also for planning the reconstruction of an accelerator facility. In this study, the depth profiles of ^{36}Cl long-lived radio-nuclei were measured for the shielding concrete exposed to secondary particles in the 12 GeV proton EP2 beam-line at KEK.

A view of the EP2 beam line and sampling positions are shown in Fig. 1. The samples are cored out of the shielding concrete, 3m in length for the concrete wall with diameter of 5 cm at the 60cm from a floor, at the position marked B in the Fig. 1. The concrete shielding is constructed with three concrete blocks. The thickness of each block is 1m. The most inner block is made from a normal concrete and a heavy concrete is a main component for the remaining two blocks.

The results of the depth profile of ^{36}Cl are shown in Fig. 2 together with the results of the activity measurements of ^{22}Na, ^{54}Mn, ^{60}Co, and ^{152}Eu [1]. The closed circles represent the results of the ^{36}Cl measurements as a function of depth. Ordinate shows the ration of ^{36}Cl to ^{35}Cl. The ^{36}Cl/^{35}Cl ration decreases smoothly according to the deepness of the concrete shielding in the rage of 0cm to 200 cm. On the other hand, the ratio is tremendously stepped up in the block No.3, from 200 cm to 300 cm. This phenomenon is also shown in the activity measurements of ^{22}Na and ^{152}Eu. Therefore, it is say that the history of the block No.3 is difference from those of block No.1 and block No.2. It is clear that the block No.3 might be used, in the past, in the field with strong radio-activity. The thermal neutron flux at the depth of 3 cm is estimated $3.2*10^{14}$ cm^{-2}. This number, the integration of the neutron yield for the twenty years, corresponds to the yield of neutron for about 10 seconds of a typical nuclear reactor.

Reference

1] T.Miura, S.Takahara, S.Ishihama, N.Ohtsuka, and T.Kunifuda, KEK Preprint 99-68, (1999)

[1] High Energy Accelerator Research Organization

[2] Tokyo Nuclear Services Company

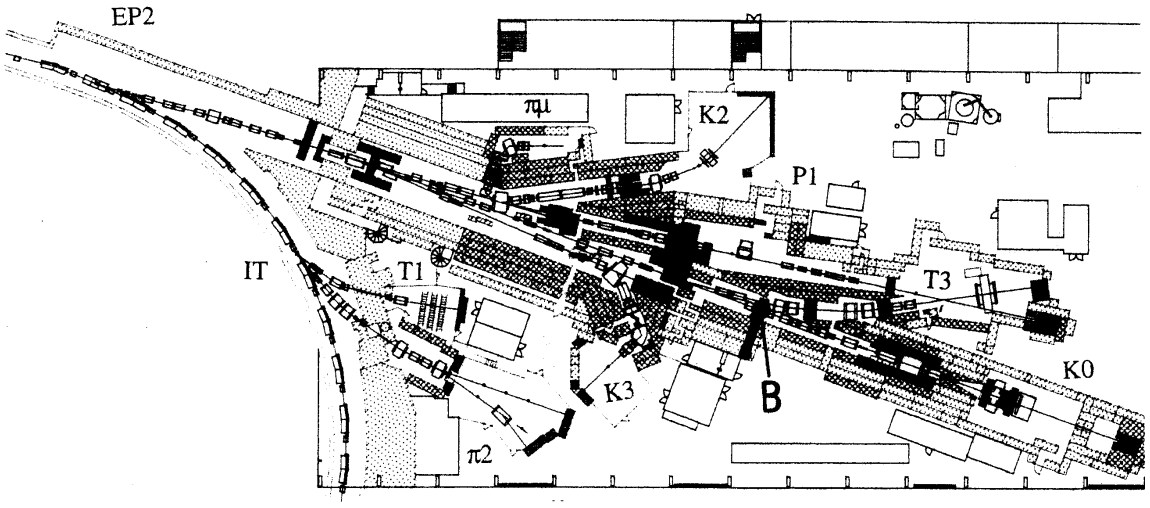

Fig. 1 The EP2 Beam Line of KEK Proton Synchrotron Accelerator.
Samples are drilled out from the concrete shielding blocks located at point B, black line.

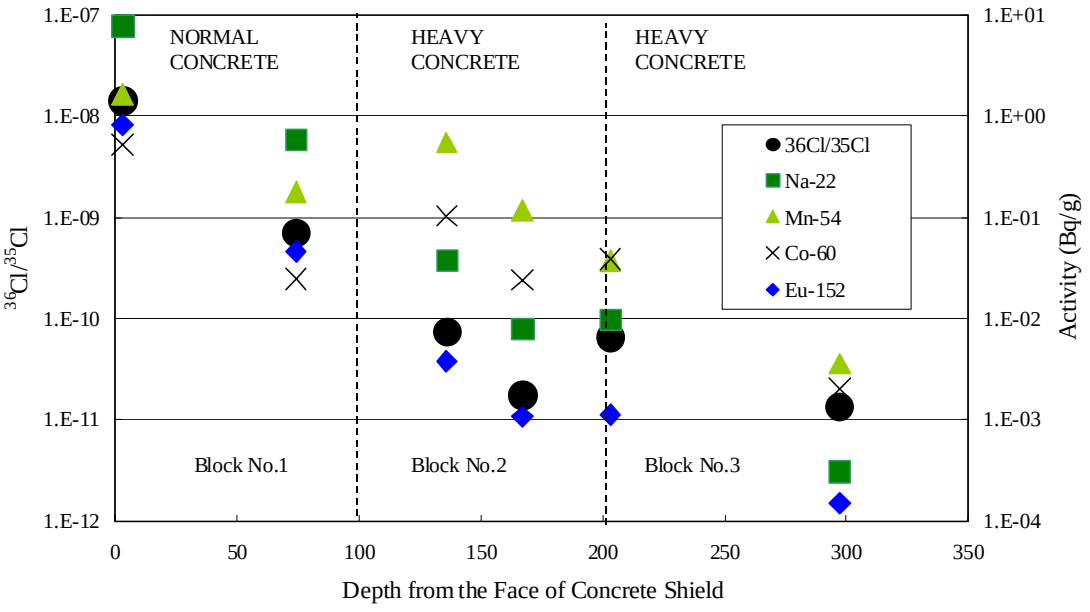

Fig. 2 $^{36}Cl/^{35}Cl$ ratio of the concrete blocks as a fuction of depth together with the activities of ^{22}Na, ^{54}Mn, ^{60}Co, and ^{152}Eu

4.7 AMS ^{36}Cl measurement of JCO soil samples

D. Arai, R. Seki, Y. Nagashima, T. Takahashi, and H. Kume[1]

A critical nuclear accident at the nuclear fuel processing facility, JCO, in Tokaimura was one of the most serious accidents in the history of nuclear power plants. Tremendous numbers of neutron particles were released. For ecological and health reasons, several Japanese groups have estimated the total neutron flux from the site through by the analysis of short-lived radio-activated nuclei such as ^{198}Au. In order to sharpen the estimations, we commenced to measure the yield of ^{36}Cl radioisotopes in the samples being collected from the accident site in the last year. The neutron flux can be estimated from the ratio of ^{36}Cl to ^{35}Cl because the ^{36}Cl nuclei are created from ^{35}Cl through a thermal neutron capture process, ^{35}Cl(n,γ)^{36}Cl. A ^{36}Cl AMS technique [1] is the only available method for detecting very rare and very long-live ^{36}Cl radioisotopes.

We have been studying several soil samples that are collecting from the site of JCO. Adding to the soil samples, both KCl and NaCl samples are also included in the study. AgCl is the most suitable target material for getting high and steady Cl negative ion beam in the ion source. Therefore, the soil samples, as well as KCl and NaCl, are formed to AgCl by our sample preparation protocols. The preparation method is described in somewhere [2]. The results of the ^{36}Cl to ^{35}Cl ratio measurements are listed up on a Table 1. The ^{36}Cl/^{35}Cl ratio of the NaCl sample is very small, $1.6*10^{-14}$, and is almost the same to the background level, $1*10^{-14}$. Therefore, the influence of the thermal neutron emerging by the nuclear accident is limited within about 80m from the site of accident. On the other hand, the ^{36}Cl yields of the soil-A and soil-I are about thousand times larger than the ^{36}Cl yield of the NaCl sample. The thermal neutron flux at 10m distances is estimated at $2.5*10^{11}$cm^{-2} from the result of the soil-B. Fig. 1 shows the ^{36}Cl to ^{35}Cl ratio as a function of distance. An inverse square of distance rule well explains the decrease of the ^{36}Cl/^{35}Cl ratio according to the increase of the distance. The closed circles represent the estimation of the ^{36}Cl to ^{35}Cl ratio by a Mon-te Car-lo simulation [3]. It seems that the calculation is systematically a little bit smaller than the measurement. Thought the difference is systematic, we are trying to compare our standard AgCl sample to the standard one of Tokyo University. Up to now, this discrepancy is not well explained. The investigation is still going on.

References

1] Y.Nagashima, R.Seki, T.Takahashi and D.Arai, Nucl. Inst. & Meth., B172(2000)129-133.

2] D.Arai, R.Seki, Y.Nagashima, T.Takahashi, R.Mawatari, and H.Kume, UTTAC-68(2000)110.

3] T.Imanaka, Private Communication.

[1] National Institute for Environmental Studies

Sample	$^{36}Cl/^{35}Cl$ (Atom Ratio)	Distance from the Accidental Site (m)
Soil-A	$(1.52\pm0.09)\times10^{-11}$	2.5
Soil-I	$(3.68\pm0.06)\times10^{-11}$	2.5
Soil-B	$(1.10\pm0.02)\times10^{-11}$	10
Soil-F	$(1.01\pm0.20)\times10^{-11}$	10
Soil-G	$(6.79\pm0.12)\times10^{-12}$	15
Soil-H	$(3.68\pm0.06)\times10^{-12}$	17
KCl	$(5.6\pm0.5)\times10^{-14}$	56
NaCl	$(1.6\pm0.3)\times10^{-14}$	80

Table 1 ^{36}Cl contents in the JCO soils. Results are represented as the ratio of ^{36}Cl to ^{35}Cl.

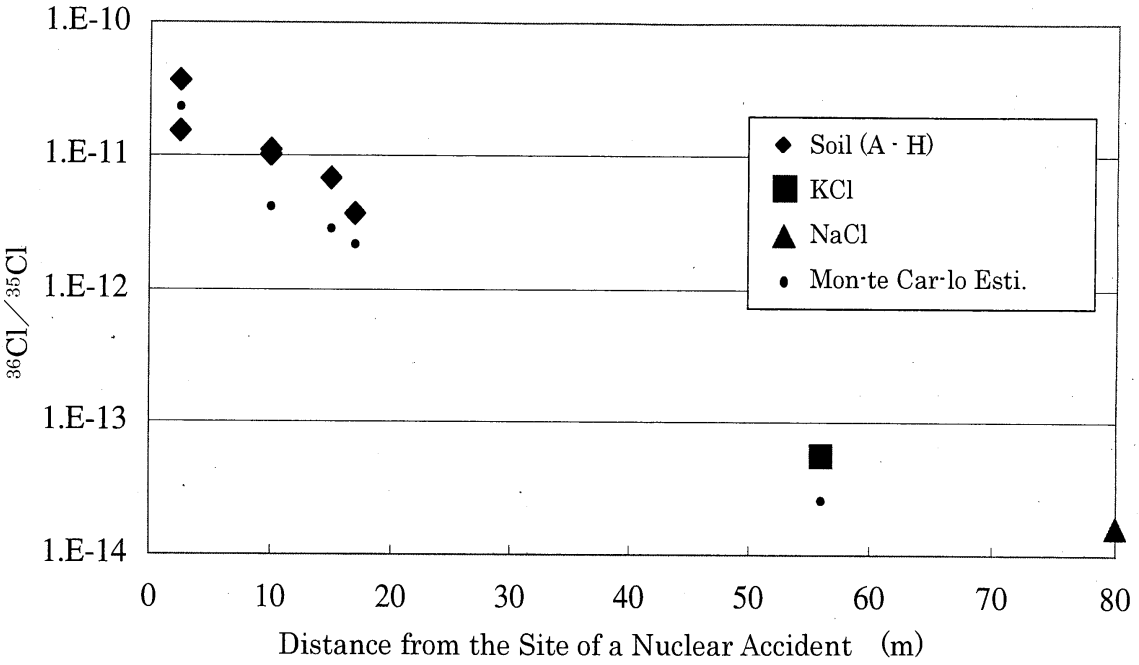

Fig. 1 Ratio of ^{36}Cl to ^{35}Cl AMS measurement as a function of distance.

5. LIST OF PUBLICATIONS

ACCELERATOR AND EXPERIMENTAL FACILITIES

K.Shima, S.Ishii, T.Takahashi, I.Sugai
Optimum thickness of carbon stripper foils in tandem accelerator in view of transmission and lifetime.
Nucl. Instrum. and Method A 460 (2001) 233-239.

Appropriate carbon stripper foils of tandem accelerator in thickness, lifetime and transmission
K.Shima, S.Ishii, T.Takahashi, I.Sugai, and M.Oyaizu
SNEAP 1999, World Scientific Publ. (2000) , pp.121-132.

T.Ito, N.Hayashizaki, S.Matsui, K.Sasa, H.Schubert, S.Osvath, T.Hattori.
Acceleration test of TIT-IHQ linac for heavy ion irradiation.
Nuclear Instruments and Methods in Physics Research, B 161-163 (2000) 1164-1167.

T.Hattori, S.Matsui, N.Hayashizaki, H.Tomizawa, T.Yoshida, K.Sasa, S.Gates, K.Kawasaki, T.Niizaki, K.Isokawa, T.Ito, M.Okamura.
Compact IH-APF type linac for PIXE and RBS analysis.
Nuclear Instruments and Methods in Physics Research, B161-163 (2000) 1174-1177.

S.Matsui, T.Hattori, N.Hayashizaki, H.Tomizawa, K.Sasa, T.Yoshida, K.Isokawa, T.Ito.
Compact IH-APF type linac for heavy-ion implantation.
Nuclear Instruments and Methods in Physics Research, B 161-163 (2000) 1178-1181.

NUCLEAR PHYSICS

Y. Tokimoto, H. Utsunomiya, T. Yamagata, M. Ohta, Y.-W. Lui, R.P. Schmitt, S. Typel, Y. Aoki, K. Ieki, K. Katori
Coulomb breakup of ^{7}Li for nuclear astrophysics
Phys. Rev. C63(2001) 035801

Y.Aoki, N.Okumura, T. Joh and Y.Honkyu
CDCC analysis of vector and tensor analyzing powers in ^{208}Pb(d,d) elastic scattering at E_d=8 MeV
14th International Spin Physics Symposium (SPIN2000), Osaka, October 2000

T. Katabuchi, K. Kudo, K. Masuno, T. Iizuka, Y. Aoki and Y. Tagishi,
Polarization transfer for the ^{2}H(d,p)^{3}H reaction at =0˚ at a very low energy,
14th International Spin Physics Symposium (SPIN2000), Osaka, October 2000

C.S.Lee, J.H.Ha, J.H.Lee, J.Y.Huh, J.C.Kim, C.-B.Moon, S.J.Chae, T.Komatsubara, T.Shizuma, H.Kimura, K.Matsuura, K.Kato, Y.Sasaki, H.Ishiyama, K.Furuno
High-spin states of rotational bands built upon nu i-13/2 in ^{166}Lu
Eur.Phys.J. A 8 (2000) 1-3.

C.-B.Moon, T.Komatsubara, K.Furuno
Rotational Bands in ^{122}Cs
Nucl.Phys. A674, 343-356 (2000), Erratum Nucl.Phys. A678 (2000) 457.

Y.H.Zhang, T.Hayakawa, M.Oshima, Y.Toh, J.Katakura, Y.Hatsukawa, M.Matsuda, N.Shinohara, T.Ishii, H.Kusakari, M.Sugawara, T.Komatsubara
Observation of signature inversion in odd-odd ^{178}Ir
Eur.Phys.J. A 8 (2000) 439-442.

A.A.Pasternak, Y.Sasaki, A.D.Efimov, V.M.Mikhailov, T.Hayakawa, Y.Toh,M.Oshima, Y.Hatsukawa, J.Katakura, N.Shinohara, Z.Liu, K.Furuno
DSA lifetime measurements and structure of positive-parity bands of ^{120}Xe
Eur.Phys.J. A 9 (2000) 293-297.

HIGH ENERGY NUCLEAR PHYSICS

L. Ahle, (A. Kumagai, K. Kurita, H. Sako, Y. Miake, S. Ueno-Hayashi, K. Yagi), et.al.
Particle production at the AGS: an excitation function
Nucl.Phys. A661(1999) 472-475.

M.M. Aggarwal, (T. Chujo, R. Higuchi, S. Kato, M. Kurata, K. Kurita, Y. Miake, Y.Miyamoto, S. Nishimura, H. Sako, S. Sato, K. Yagi, Y. Yokota), et.al.,
Elliptic emission of K+ In 158-A-GeV Pb + Pb collisions
Nucl.Phys. A661 (1999) 464-467.

T. Peitzmann, (T. Chujo, R. Higuchi, S. Kato, M. Kurata, K. Kurita, Y. Miake, Y.Miyamoto, S. Nishimura, H. Sako, S. Sato, K. Yagi, Y. Yokota), et.al.,
Recent results from the WA98 experiment
Nucl.Phys. A661 (1999) 191-197.

M.M. Aggarwal, (T. Chujo, R. Higuchi, S. Kato, M. Kurata, K. Kurita, Y. Miake, Y.Miyamoto, S. Nishimura, H. Sako, S. Sato, K. Yagi, Y. Yokota), et.al.,
Central Pb + Pb collisions at 158/A – GeV/c studied by pi-pi interferometry
Eur.Phys.J. C16 (2000) 445-451.

M.M. Aggarwal, (T. Chujo, R. Higuchi, S. Kato, M. Kurata, K. Kurita, Y. Miake, Y.Miyamoto, S. Nishimura, H. Sako, S. Sato, K. Yagi, Y. Yokota), et.al.,
Collective flow and HBT in Pb + Pb collisions at the CERN-SPS
Nucl.Phys.A663 (2000) 729-732.

Tapan K. Nayak, (T. Chujo, R. Higuchi, S. Kato, M. Kurata, K. Kurita, Y. Miake, Y.Miyamoto, S. Nishimura, H. Sako, S. Sato, K. Yagi, Y. Yokota), et.al.,
Search for disoriented chiral condensates in 158/A-GeV Pb + Pb collisions
Nucl.Phys.A663 (2000) 745-748.

M.M. Aggarwal, (T. Chujo, R. Higuchi, S. Kato, M. Kurata, K. Kurita, Y. Miake, Y.Miyamoto, S. Nishimura, H. Sako, S. Sato, K. Yagi, Y. Yokota), et.al.,
$^{++}$ production in 158-A-GeV ^{208}Pb + ^{208}Pb interactions at the CERN SPS.
Phys.Lett.B477 (2000) 37-44.

L. Ahle, (T. Chujo, A. Kumagai, K. Kurita, Y. Miake, H. Sako, S. Ueno-Hayashi, K. Yagi), et.al.,
An excitation function of K- and K+ production in Au + Au reactions at the AGS
Phys.Lett.B490 (2000) 53-60.

M.M. Aggarwal, (T. Chujo, R. Higuchi, S. Kato, M. Kurata, K. Kurita, Y. Miake, Y.Miyamoto, S. Nishimura, H. Sako, S. Sato, K. Yagi, Y. Yokota), et.al.,
Three pion interferometry results from central Pb + Pb collisions at 158-A-GeV/c
Phys.Rev.Lett. 85 (2000) 2895.

M.M. Aggarwal, (T. Chujo, R. Higuchi, S. Kato, M. Kurata, K. Kurita, Y. Miake, Y.Miyamoto, S. Nishimura, H. Sako, S. Sato, K. Yagi, Y. Yokota), et.al.,
Scaling of particle and transverse energy production in ^{208}Pb + ^{208}Pb collisions at 158-A/GeV
Eur.Phys.J.C18 (2001) 651-663.

M.M. Aggarwal, (T. Chujo, R. Higuchi, S. Kato, M. Kurata, K. Kurita, Y. Miake, Y.Miyamoto, S. Nishimura, H. Sako, S. Sato, K. Yagi, Y. Yokota), et.al.,
Observation of direct photons in central 158-A/GeV ^{208}Pb + ^{208}Pb collisions
Phys.Rev.Lett. 85 (2000) 3595.

Y. Miake,
Delta++ production & Directed and Elliptic Flow in 158 A GeV Pb + Pb collisions
XXXth International Conference on High Energy Physics, July 27 - August 2, 2000, Osaka, Japan

ATOMIC AND SOLID STATE PHYSICS, AND CLUSTER SCIENCE

K.Awazu, S.Ishii and K.Shima
Creation of individual holes in SiO_2 on Si by swift heavy ion bombardment followed process
2000 Intern. Microprocesses and Nanotechnology Conference (MNC 2000) July, 2000, Tokyo

K.Awazu, S.Ishii , K.Shima
Formation of individual holes in amorphous SiO2 by swift heavy-ion bombardment followed by wet and dry etching.
Jpn. J. Appl. Phys. 2000; 39: 7058-7059.

K.Shima and S.Nagai
Foil thickness for ions attaining charge equilibrium.
4th Asian International Seminar on Atomic and Molecular Physics, October 2000, Taipei,
J. Chinese Chem. Soc. 48 (2001) no.3A, 178-183.

Ion-induced electron emission from Si crystal targets covered with noncrystalline Si layers, Hiroshi Kudo, Naoki Nakamura, Kohki Shibuya, Kazumasa Narumi, Shunya Yamamoto, Hiroshi Naramoto, Koji Sumitomo, Seiji Seki,
Nucl. Instrum. & Methods 168 (2000)181-191.

H. Kudo, S. Seki, K. Sumitomo, K. Narumi, S. Yamamoto, H. Naramoto,
Ion-induced electron measurements using crystal targets overlaid with noncrystalline layers,
Nucl. Instrum. & Methods B164-165 (2000) 897-902.

H.Mizubayashi, G.Nishikori and H.Tanimoto,
High-cycle fatigue properties of modified 316 stainless steels under in-site thermal-pulses,
Materials Transactions, 42 (2001)151-156 .

I. Arai, H. Sasaki, T. Shimayama and S.M. Lee,
Dissociation of Si clusters produced by bombardment of 6keV Xe atoms,
Transactions of the Materials Research Society of Japan, 25 (2000)947-950.

C. K. Chung, I. Arai, S. M. Lee,
Critical size of metal cluster in a metal cluster source controlled with a magnetron,
Transactions of the Materials Research Society of Japan, 25 (2000) 955-958.

T. Kurita, M. Imanaka, T. Nakagawa, M. Kidera and S.M. Lee,
Production of highly charged Xe ions from liquid He free super conducting electron cyclotron resonance ion source,
Jap. J. Appl. Phys. 40, 5A (2001).

I. Arai, C.K. Chung, H. Sasaki and S.M. Lee,
Physical processes of cluster formation in gas aggregation and fast atom bombardment
Transactions of the Materials Research Society of Japan, 26 (2001).

I. Arai,
Scaling observed in abundance spectra of 3D transition metal cluster produced by sputtering
Desorption 2000 Conference, Saint-Malo, France, 3-7 September 2000.

ION BEAM APPLICATION

M. Kurosawa and S. Murao
Improvement of micro-PIXE to quantify geochemical thick target.
Bull. Geol. Surv. Japan, 51(2000) 325-328.

D.Yamazaki, T.Kato, H.Yurimoto, E.Ohtani and M.Toriumi.
Silicon self-difffusion in $MgSiO_3$ perovskite at 25 GPa.
Physics of the Earth and Planetary Interiors, 119 (2000) 299-309.

T. Kato, H. Terasaki and T. Kubo
Transport properties of earth material-new insights on science of the Earth's interior-,
J. Geography, 109 (2000) 868-873.

R.Seki et al,
The JCO criticality accident at Tokai-mura Japan: an overview of the sampling campaign and peliminary results,
J. Environmental Radioactivity 50 (2000) 3-14.

Y.Nagashima et al,
Status of ^{36}Cl AMS system at the University of Tsukuba,
Nucl. Instrum. Methods B172 (2000) 129-133.

6. THESES

Ph. D. Theses

N.Okumura	Total reaction cross section of p+^{28}Si system near neutron threshold energy
C.K. Chung	Cluster formation and growth in a metal cluster source controlled with a magnetron and a gas aggregation cell
T. Kurita	Development of an ECR ion source using liquid-helium-free superconducting solenoid coils
N.Nishiguchi	Crystal structures and magnetic properties of the two-dimensional spin-1/2 system MV_nO_{2n+1}
S.Sakai	Physical Property of High-Density Nanocrystalline Gold
T.Nakajou	Study of single particle spectra and two particle correlation in Au+Au collisions at 4 - 11 A GeV
S.Satou	Study of Δ^{++} resonance abundance in 158 A GeV Pb + Pb collisions at CERN-SPS

M. Sc. Theses

J. Hirose	Energy dependence of cluster production by sputtering
S. Shimakura	Secondary electron emission of clusters and their detection efficiency
K.Sawada	Development of of the proton polarimeter for double scattering experiment
K.Kudou	Measurement of polarization transfer coefficient in the ^{2}H(d,p)^{3}H reaction at incident deuteron energy of 90 keV
K.Masuno	Analyzing powers for the continuous spectrum region
R.Arai	Crystal structures and magnetic properties of δ-phase $Ag_xV_2O_5$
I.Amemiya	Basic properties of the insertion-electrode system $Li_{1+x}V_3O_8$
K.Kogure	Nuclear magnetic resonance of the mixed-valence system $Cu_7V_6O_{19}$
J.Hasegawa	Crystal structures and magnetic properties of $Tl_{0.5}V_2O_5$
M.Ohira	Structure-sesitive ion-induced electron spectroscopy of damaged Si
T.Kinosita	Structure-sensitive ion-induced Auger electron spectroscopy of layered crystals
D.Hakozaki	The prototype production and evaluation of Pestov Spark Counter for high energy nuclear experiments
M.Aizawa	Single particle measurement of pion, kaon, and proton at 158AGeV Pb+Pb collision
K. Satou	Measurements of fusion cross sections in the reactions of ^{82}Se +^{138}Ba and ^{82}Se +^{134}Ba
K. Yamada	Measurement of the magnetic moment of the second-excited state in ^{165}Ho with transient magnetic field

7. SEMINARS

Date	Speaker and Title
2000	
May. 17	H.Miyatake (KEK) ; Future plan of the nuclear physics group at KEK
May. 24	T.Katabuchi (Univ. of Tsukuba); Polarization transfer for the $^{2}H(d,p)^{3}H$ reaction at very low energies
May. 24	Y.Tagishi (Univ. of Tsukuba) ; Direct detection of alpha particles emitted from daughter nucleus of random and thoron
May. 31	K.Yabana (Univ. of Tsukuba) ; Reaction mechanisms of Halo Nuclei
June. 7	T.Nakagawa (RIKEN); New method for the trace element analysis using ECR ion source and heavy ion
June. 14	Y.Hatsukawa (JAERI); Application of the method of multidimensional spectrum to activation analysis
June. 28	S.M.Lee (Univ.of Tsukuba); Nuclear physics by femtosecond laser and cluster
Sept. 6	T.Kurita (Univ.of Tsukuba) ; Development of ECR ion source using liquid-He-free Superconducting solenoid coils
Sept. 10	I.Arai (Univ.of Tsukuba) ; Report on desorption 2000 conference
Sept. 27	G.Vourvopoulos (Western Kentucky Univ.); Pulsed fast/thermal neutron analysis : a technique for the detection of explosives and drugs
Oct. 11	Chun-Kyun Chung (Univ. of Tsukuna);Cluster formation and growth in a metal cluster source controlled with a magnetron
Oct. 25	S.Satou (Univ. of Tsukuba); Study of Δ^{++} resonannce abundance in 158 A GeV Pb+Pb collisions at CERN-SPS
Nov. 1	T.Itahashi (Osaka Univ.) ; Feasibilities of tritium acceleration and its perspectives
Nov. 8	Xiao-Hong Zhou (IMP, Lanzhou) ; Present status of nuclear structure studies in IMP at Lanzhou Shu-Xian Wen (CAEI, Beijing); Present status of nuclear structure studies in CAEI at Beijing
Nov. 22	Yu-Hu Zhang (IMP, Lanzhou) ; Study of high-spin states in doubly odd nuclei around A=160 180
Dec. 1	Y.Tagishi (Univ. of Tsukuba) ; High-Sensitive Detector for Environmental Radon
Dec. 15	K.Yoshinari (Central Research Lab., Hitachi Ltd.) ; Numerical study of ion behaviors in radiofrequency quodrupole mass spectrometer
Dec.20	Y.Honkyu (Univ. of Tsukuba) ; Measurement of the proton spectrum in deuteron break-up reaction, K. Kudo (Univ. of Tsukuba); Polarization transfer coefficient Kyy' in the $^{2}H(d,p)^{3}H$ reaction at $\theta = 0°$ at very low energies,
Dec. 27	K.Yamada (Univ. of Tsukuba); Measurement of the magnetic moment of the second-excited state in ^{165}Ho with Transient Magnetic Field, J.Hirose (Univ. of Tsukuba); Energy dependence of cluster production by means of Sputtering,

2001

Jan. 10 K.Masuno (Univ. of Tsukuba); Analyzing powers in the continuum of the ($\vec{p}$,α) and ($\vec{d}$,α) reactions at E=20MeV
K.Satou (Univ. of Tsukuba); Measurements of Fusion Cross Sections in the Reactions of ^{82}Se + ^{138}Ba and ^{82}Se + ^{134}Ba

Jan. 17 T.Shinozuka (Tohoku Univ.) ; Renewal of the cyclotron accelerator and future plan of experiment at the Cyclotron and RI Center at Tohoku Univ.

Jan. 18 T.Kurita (Univ. of Tsukuba); Development of an ECR ion source using liquid-helium-free superconducting solenoid coils

Jan. 24 D.Hakozaki (Univ. of Tsukuba); The prototype production and evaluation of Pestov Spark Counter for high energy nuclear experiments,
K.Sawada (Univ. of Tsukuba); Proton polarimeter using a liquid helium target,

Jan. 31 S.Shimakura (Univ. of Tsukuba); Secondary electron emission caused by clusters and their detection efficiency,
M.Aizawa (Univ. of Tsukuba); Single particle measurement of pion, kaon, and proton at 158AGeV Pb+Pb collision,

Feb. 8 N.Horikawa (Nagoya Univ.) ; Polarized target for d-d scattering and dynamic nuclear polarization

March 13 M.Matoba (Kyushu Univ.) ; Utilization and future of accelerators in Japanese national universities

8. SYMPOSIUM

25th Anniversary of the Foundation of the UTTAC
-------Ion beam science using tandem accelerator -------

December 12-13, 2000

University Hall, University of Tsukuba

Opening

25 years of UTTAC, *K.Furuno (Univ. of Tsukuba)*

Elemental analysis I

Application of PIXE to earth science----micro analysis of fluid inclusion, *M.Kurosawa(Univ. of Tsukuba)*

Micro-elemeental analysis using multiple γ-ray detection methods, *Y.Tou (JAERI)*

Elemental analysis II

Environmental research by AMS at NIES-TERRA, *Y.Shibata (NIES)*

AMS at the MALT of Tokyo University, *H.Matsuzaki (Tokyo University)*

Present status of AMS at the University of Tsukuba, *Y.Nagashima (CMTN)*

Development of AMS system at Kyushu University, *S.Mitarai (Kyushu Univ.)*

Nuclear Phsics I

High spin studies of nuclei around A=120 at the Tandem Accelerator center of the University of Tsukuba (UTTAC), *Chang Bum Moon (Hoseo Univ.)*

Projectile coulomb excitation of Ge and Se isotopes, *T,Hayakawa (JAERI)*

Meson and quark degrees of freedom in the nucleus detected through the nuclear β decay, *K.Minamisono (Osaka Univ.)*

Symmetry structure of mirror nuclei studied in M1 and GT transitions, *Y.Shimbara (Osaka Univ.)*

Nuclear Phsics II

A coulomb breakup experiment, *H.Utsunomiya (Konan Univ.)*

Physics on one-nucleon transfer reactions in several tens MeV energy region, *M.Matoba (Kyushu Univ.)*

Current and near future experiments by using tandem accelerator, *Y.Aoki (Univ. of Tsukuba)*

Nuclear reaction using an ion source, *Y.tagishi (Univ. of Tsukuba)*

Some historical topics around the period of the birth of UTTAC, *T.Mikumo (emeritus prof. of Univ. of Tsukuba)*

Atomic and Solid-State Physics I

Ion-Induced Electron Emission from Crystalline Solids, *H.Kudo (Univ. of Tsukuba)*

Electronic excitation effects in oxide superconductors irradiated with high energy ions, *N.Ishikawa (JAERI)*

Charge-state equilibration of fast ions passing through a carbon foil and a single C60 molecule, *A.Itoh (Kyoto Univ.)*

Atomic and Solid-State Physics II

Formation of individual holes in amorphous SiO2 by swift heavy-ion bombardment followed by wet and dry etching, *K.Awazu (Electrotechnical Lab.)*

Local structure of GaN doped with Eu, *S.Morishima (Univ. of Tsukuba)*

Enhanced conductivity in polymer materials irradiated with proton beams, *S.Matumoto (Chiba Inst. Techmology)*

Ion Beam Techhnology I

Progress of cluster physics at UTTAC, *I.Arai (Univ. of Tsukuba)*

Measurement of mass distribution of gold clusters, *T.Mizota (GIRI, Nagoya)*

Development of beam, target and analyzerfor astro-nuclear experiment, *K.sagara (Kyushu Univ.)*

Development of monoenergetic neutron source using the $^{1}H(^{13}C, n)$ reaction in the MeV region, *Y.Watanabe (Kyushu Univ.)*

Ion Beam Techhnology II

Frontier of long-lived cluster and hybrid carbon stripper foils for high energy, high intensity ion beams, *I.Sugai (KEK)*

A beam-foil interaction study with lazer displacement meter, *I.Katayama (KEK)*

Acceleration of microparticles (dsust) and its application, *H.Shibata (Tokyo Univ.)*

Concluding Remarks

Science using beams of nucleus, K.Katori *(emeritus prof. of Osaka Univ.)*

9. LIST OF PERSONNEL

Accelerator Center

K. Furuno	Director, Professor
K.Shima	Associate Professor
T.Komatsubara	Assistant Professor
K.Sasa	Assistant Professor
T.Katabuchi	Research Associate
S.Ishii	Mechanical Technician
H.Kimura	Computer Technician
H.Oshima	Electric Technician
Y.Tajima	Mechanical Technician
T.Takahashi	Electric Technician
Y.Yamato	Electronics Technician
K.Itoh	Research Fellow
Li Tian-Xin	Research Fellow
Y.Kamiyama	Accelerator Support Staff
O.Akutsu	Administrative Stuff

Steering Committee

K.Furuno	Chairperson, Tandem Accelerator Center
Y.Kajiwara	Inst. of Geoscience
R.Kanzaki	Inst. of Biological Sciences
T.Komatsubara	Tandem Accelerator Center,
H.Kudo	Inst. of Applied Physics
S.M.Lee	Inst. of Physics
M.Onoda	Inst. of Physics
R.Seki	Inst. of Chemistry
K.Shima	Tandem Accelerator Center
Y.Tagishi	Inst. of Physics
K.Yabana	Inst. of Physics
K.Yasuoka	Inst. of Basic Medical Sciences

Scientific Guests and Fellows

C.B.Moon	Hoseo Univ., Korea
Zhang Yu-Hu	IMP, Lanzhou
K.Awazu	Electrotechnical Lab.
M.Matoba	Kyushu Univ.
Y.Hata	JAERI
I.Daitou	Nagoya Univ.
M.Takeuchi	Nagoya Univ.
T.Mizota	GIRI, Nagoya
S.Matsumoto	Chiba Inst. Technology
H.Kume	National Inst. For Environmental Studies
T.Ishihara	KEK

Research Members

Inst. of Physics

Y.Aoki	I.Arai	S.Esumi	K.Furuno	T.Katabuchi
T.Komatsubara	S.M.Lee	Y.Miake	N.Okumura	M.Onoda
S.Satou	K.Sasa	Y.Tagishi	T.Une	

Inst. of Geoscience

R.Anma	T.Katou	M.Kurosawa

Inst. of Applied Physics

T.Azuma	A.Uedono	E.Kita	H.Kudo	K.Shima

Inst. of Chemistry

R.Seki

Inst. of Materials Science

H.Ikeda	T.Koyano	H.Mizubayashi	K.Takita	H.Tanimoto

College of Medical Technology and Nursing

Y.Nagashima

Tandem Accelerator Center

K.Itoh	Li Tian-Xin

Venture Business Lab.

T.Miyazaki

Graduate Students

Doctoral Degree Programs in Physics

Ma Ying-Jun	C.K.Chung	T.Kurita	H.Sasaki	N.Nishiguchi
N.Kawachi	T.Jou	M.Yamaguchi	T.Nakajou	Y.Sasaki
S.G.Lee	K.Masuno	M.Suzuki	M.Imanaka	K.Satoh
J.Hirose	R.Arai	M.Ono,	H.Tsuruoka	Y.Takechi
K.Takeda				

Doctoral Degree Programs in Engineering

K.Ono	N.Umeda	K.Suzuki	K.Asami	S.Sakai
N.Ookubo	Li Changqing			

Doctoral Degree Programs in Education

T.Tsukada

Master's Degree Programs in Sciences and Engineering

T.Sakai	Y.Honkyu	I.Amemiya	K.Kogure	K.Sawada
M.Aizawa	Y.Akutsu	K.Kudou	S.Shimakura	S.Shimano
D.Hakozaki	J.Hasegawa	K.Yamada	M.Oohira	T.Kinoshita
S.Yokose	T.Iizuka	A.Negishi	A.Oyadomari	D.Kasuga
K.Kanbe	M.Muramatsu	Y.Kouda	Y.Mihara	

Master's Degree Programs in Environmental Sciences

D.Arai

Undergraduates

M.Ishizuka	M.Yoshimoto	M.Imon	M.Shioda	T.Furui
M.Aramaki	K.Teranishi	N.Umezawa	T.Okabe	N.kajiya
Y.Kuroki	S.Sakai	M.Shindou	A.Danmura	H.Masui
H.Imai	K.Sekine	A.Tokunaga	T.Banno	Y.Kunieda
M.Higurashi	I.Arano	W.Iwazaki	T.Suguri	S.Numazawa
M.Nakazumi				